Low Frequency Waves in the Shoaling and Nearshore Zone

A Validation of XBeach

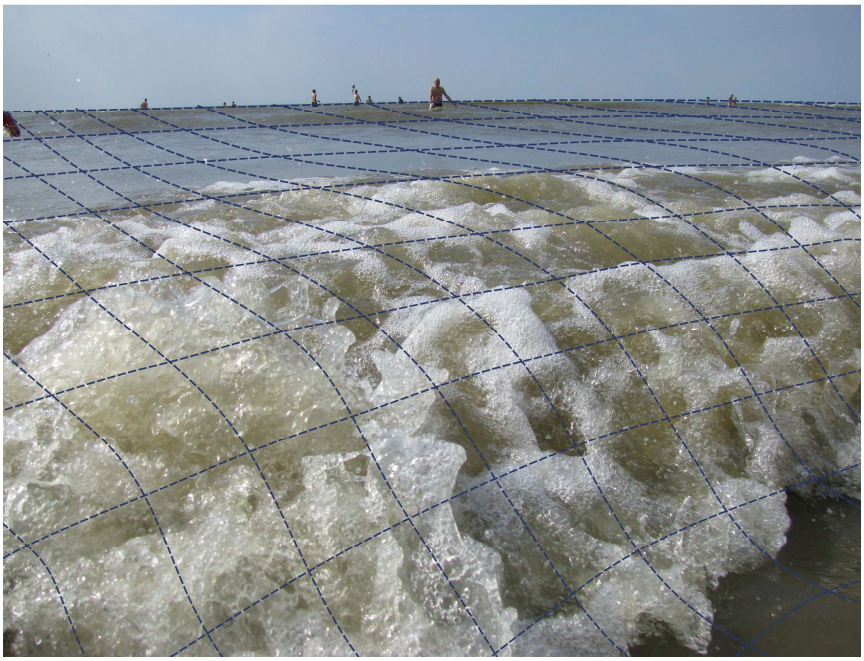

M.Sc. Thesis

Christopher Daly

CoMEM

30 June 2009

Delft University of Technology

Faculty of Civil Engineering and Geosciences

Section of Hydraulic Engineering

Department of Coastal Engineering

Low Frequency Waves in the Shoaling and Nearshore Zone

A Validation of XBeach

M.Sc. Thesis

Christopher Daly

June 2009

Graduation Committee:

Prof.dr.ir. M.J.F. Stive	TU Delft & CoMEM
Prof.dr.ir. J.A. Roelvink	UNESCO | IHE & Deltares
Dr.ir. A.R. Van Dongeren	Deltares
Ir. J.S.M. Van Thiel De Vries	Deltares & TU Delft
Ir. R.T. McCall	Deltares
Dr.ir. R.J. Labeur	TU Delft

"If you want to model nature, you must copy nature.

If you want to copy nature, you must understand nature."

Ib Svendsen

Summary

Following the discovery of surfbeat sixty years ago by *Munk* [1949] and the pioneering works of *Longuet-Higgins* and *Stewart* [1952] laying the theoretical foundation of radiation stress, we are today able to have a better understanding into the primary mechanism for the generation of forced low frequency (LF) waves. In addition *Symonds et al.* [1982] and *Schäffer* [1993] have proposed alternative methods of free LF wave generation due to wave breaking.

It has been found by many researchers since that LF waves dominate the wave energy spectrum in very shallow water. Given that much of the longshore and cross-shore morphological processes are located within this zone, LF waves play an important role in determining morphological change, especially dune erosion and overwash during storm events. The numerical model, XBeach [*Roelvink et al.* (2008)], has been developed to simulate such morphological processes which are influenced by LF waves. For hydrodynamics, it utilizes the wave forcing determined from a second generation wave module to drive linearized shallow water equations within a flow module.

The objective of this thesis focuses on validating the hydrodynamics of XBeach with particular attention paid to the estimated LF waves. This is particularly important to correctly estimate morphological changes, as it is highly dependent on the accurate representation of waves and currents. In the validation study, XBeach is used to replicate the flume experiment of *van Noorloos* [2003] in which bichromatic and irregular wave conditions are imposed on a plane sloping beach. The advantage of using this experiment is that measurements have a high spatial resolution, allowing for decomposition into incoming and outgoing wave components.

Group-varying time-averaged short wave parameters are used to investigate the accuracy of the short wave module in XBeach, while at the same time the relationship between the short waves and LF waves are determined by looking at the energy transfer to and from the LF components.

The results confirm many previous findings, such as the plus 180 degree phase difference between the short wave envelope and the bound LF wave, the dominance of LF wave energy in shallow water and the ability of LF waves to extend their reach to the uppermost parts on a beach. Given the limitations of the assumptions based on linear wave theory, the short wave results from XBeach are quite good, especially when using a newly modified breaker parameterization of *Battjes* and *Janssen* [1978] by *Roelvink* [Pers. Com. 2009].

The main shortfall of the model is that it tends to overestimate the bound LF wave heights in shallow water for irregular waves. This is believed to be partly due to the overestimation of the energy and radiation stresses contained in the short waves in this region. In reality, as waves approach breaking, non-linearities present in the waves increase, which, during breaking, effectively redistributes energy within the wave spectrum. Since frequency dependent shoaling of short waves is not currently enabled in XBeach, the energy within the HF band may tend to encourage continued shoaling of the LF waves in the surf zone. As such, it is recommended that

the current wave action conservation scheme be improved to allow for either reduction or redistribution of the short wave energy during shoaling.

Wave run-up as modelled with the linearized shallow water equations is shown to over-steepen the front of the LF wave in the swash zone. This effect is a likely result of the numerical scheme used, which tends to limit the maximum run-up height based on a minimum depth for which a computational grid cell is determined to be wet.

In general, XBeach has shown that it is capable of modelling both quantitatively and qualitatively the short wave energy flux and LF wave shoaling and reflection quite will without inducing serious errors from the linear simplifications in the wave module. Wave-current interaction, which was not considered in the modelling, can most likely give even better results if it is successfully incorporated in the model.

KEYWORDS: *low frequency waves, infragravity waves, wave shoaling, wave breaking, energy transfer*

Acknowledgements

I would like to thank, firstly, the members of my committee for their valued input to and critique of this thesis. Thanks especially to Jaap van Thiel de Vries for organising my placement at Deltares and also Robert McCall, Ap van Dongeren and Dano Roelvink for their invaluable explanations of the XBeach model and of the more difficult theoretical aspects of this work which made it easier to get through my objectives. You were all very approachable and very helpful.

To my family, despite being far away, your encouragement and support has helped me very much. Thank you for believing in me and tolerating my physical absence for the past two years. To my former work colleagues at Smith Warner International, David, Jamel and Philip, thank you for providing me with the initial opportunity to further develop my interest and knowledge in the field of coastal engineering.

My fellow CoMEM graduates, Siddharth, Stella, Margaret, Katja, Jiann Chyuan, Pavel, Rodrigo, Abiy, Rahma, Egon, Nicki, Mojtaba, Saravanan, Meghan and Thang, thank you for your camaraderie, humour and encouragement. It has been wonderful getting to know you all over the past few years (memories of our country presentations in Norway come to mind). Erasmus student life would not have been the same without you. I will always remember our many dinners together and those special Eurotrips.

To my work colleagues at Deltares, Sepehr, Marten, Roald, Lars, Thijs, Arend, Wout, Reynald, Mauritz, Reinoud, Stephen and Komla, thank you for your company and stimulating discussions at lunch while also commenting on my sometimes strange eating habits. It was especially nice playing football, going for walks after lunch and in between MATLAB sessions and, not to mention, the vital, hourly coffee manager sweepstakes.

To my other friends back home in Jamaica and those spread across the European continent, thank you for your inquiries and best wishes while I have been working on this thesis. It was really nice to know that I happened to cross your minds when we are far apart. I also apologize for my absence from 'social networking sites', but you all understand the reason why.

Thanks to my housemates at H.R. Het Gros, who have welcomed me within their studentenhuis during my final semester in Delft. I am glad you guys were around after working hours to provide endless entertainment and much needed distraction, especially at the indrinkborrels.

Finally, many, many thanks to Prof. Marcel Stive and the other hard-working CoMEM staff, whose vision for CoMEM and the partnership with the NTNU (Trondheim) and UPC (Barcelona) universities provided this life-changing educational experience in Europe, finally resulting with me doing this thesis which I have thoroughly enjoyed.

Christopher Daly

Delft, June 2009

Organization

This thesis report was produced at the offices of

Stichting Deltares
Rotterdamseweg 185, 2629HD,
Delft, the Netherlands

and is in fulfilment of the course requirements of the

Erasmus Mundus Master in Coastal and
Marine Engineering and Management (CoMEM)

which is organized by

Prof.dr.ir. M.J.F. Stive
Faculty of Civil Engineering and Geosciences
Delft University of Technology (TU Delft)
Delft, the Netherlands

and includes the following educational institutions

Norwegian University of Science and Technology (NTNU)
Trondheim, Norway
Polytechnic University of Catalonia (UPC)
Barcelona, Spain

at which the graduate has studied.

Contents

Symbols

ROMAN SYMBOLS

Symbol	*Unit*	*Description*
A	m	amplitude envelope
A	W/m^2	wave action
a	m	amplitude
C_f	-	envelope scaling parameter
c	m/s	phase speed / celerity
c_g	m/s	group velocity
D	W/m^2	wave dissipation
D	s	duration
E	J/m^2	energy density
E_f	W/m	energy flux
E_k	J/m^2	kinetic energy density
E_p	J/m^2	potential energy density
F	N/m^2	force / stress
F	-	Fourier transform
f	Hz	frequency
f_b	Hz	bound / difference frequency
f_{cut}	Hz	cut-off frequency
f_s	Hz	sampling frequency
f_{nyq}	Hz	Nyquist frequency
G_f	-	groupiness factor
g	m/s^2	gravitational acceleration
H	m	wave height
h	m	water depth
k	m^{-1}	wave number
L	m	wave length
m_0	m^2	variance / zeroth moment

Q	m^3/s	discharge
Q_b	-	probability of breaking
Q_w	m/s	Stokes drift
R	W/m^2	rate of energy transfer
R	m^2	roller area
R_f	-	reflection coefficient
S_{xx}	J/m^2	radiation stress
T	s	period
U	m/s	uniform flow velocity
Ur	-	Ursell parameter
u	m/s	horizontal particle velocity
v	m/s	vertical particle velocity
x	m	horizontal axis / distance
y	m	horizontal axis / distance
z	m	vertical axis / distance
Z	m	LF amplitude

GREEK SYMBOLS

Symbol	*Unit*	*Description*
α	-	breaker coefficient
β	-	normalized bed slope
γ	-	breaker parameter
δ	-	wave modulation
ε	-	wave steepness
ζ	m	LF surface elevation
$\hat{\eta}$	m	total / measured surface elevation
η	m	HF surface elevation
θ	degrees	wave propagation direction
κ	m^{-1}	LF wave number
κ	-	weighting parameter [*Schäffer* (1993)]
π	-	pi (3.14159)
ρ	-	correlation coefficient
ρ	kg/m^3	density

σ	Hz	intrinsic / relative wave frequency
σ	m	standard deviation
τ		shear stress
φ	-	velocity potential
χ	-	normalized surf zone width
ψ	rad	wave phase
ω	Hz	wave frequency
∇	-	spatial gradient operator

SUBSCRIPTS

Symbol	*Description*
$[\,]_g$	group
$[\,]_{hi}$	HF
$[\,]_{in}$	IBLF
$[\,]_{lo}$	LF
$[\,]_m$	mean
$[\,]_{m0}$	zeroth order moment / spectral significant
$[\,]_{m01}$	first order moment
$[\,]_{out}$	RFLF
$[\,]_p$	peak
$[\,]_{rms}$	RMS
$[\,]_s$	significant

ABBREVIATIONS

Symbol	*Description*
FFT	fast Fourier transform
HF	high frequency
IBLF	incoming bound low frequency
LF	low frequency
NSW	non-linear shallow water equations
RFLF	reflected free low frequency
RMS	root-mean-square
WCI	wave-current interaction

Chapter 1 – Introduction

1.1 Background

1.1.1 The Study of Morphology

It has been observed that high waves generated during a storm or hurricane can severely affect sandy coastlines. This most often results in the erosion of sediment in shallow water near the shoreline (the nearshore area) and also from beaches and dunes. During the storm, the eroded sediment is deposited in deeper water offshore or further down the coast or washed over the crest level of the beach. The movement of sediment under the influence of a current from one location to another is termed sediment transport. Morphology is the change in the bed level at a certain location over time as a result of sediment transport gradients.

There are many example cases where considerable morphological change attributed to storms occurs in the coastal zone. A well known example is that of Hurricane Katrina, which struck the gulf coast of the United States in 2005. Not only did Katrina result in considerable flooding, infrastructural damage and disruption to human related activities in the city of New Orleans, but also natural habitats located in the Mississippi delta were destroyed by the combination of high waves and storm surge. The waves swept away thousands of cubic meters of sediment from the upper parts of the delta and many barrier islands fronting the Mexican Gulf coast 'disappeared' into the sea. Even less intense tropical storms than Katrina can have far-reaching effects for other areas where response is limited and the coastal environment is even more vulnerable, such as the small island states in the Caribbean. For these countries, there is a high dependence of the local economy on tourism, which is under threat every year by the damaging effects of waves from tropical storms which cause significant morphological changes on the touristic beaches.

In many countries there is public interest in the prediction of morphological changes in the coastal zone in order to find solutions to varying problems; such as identifying areas at risk to morphological change, examining the response of natural systems after the occurrence of storms and implementing measures which potentially reduce the hazardous impacts of such storms. This requires keen insight into the physical processes that drive morphological change, and as such, there have been many models developed toward this end.

In a simple model, the morphological development is determined by a number of interactive subcategories based on the driving forces (energy input) of a system and the natural response of this system to the driving forces. Here, the driving forces are the waves and currents that are able to stir up sediment from the bed and the response of the natural system is given by its morphology. The resulting morphological changes over time affect the waves and currents (hydrodynamics) in return. The entire process is therefore a dynamic cycle, which is commonly referred to as morphodynamics, as depicted in Figure 1.1.

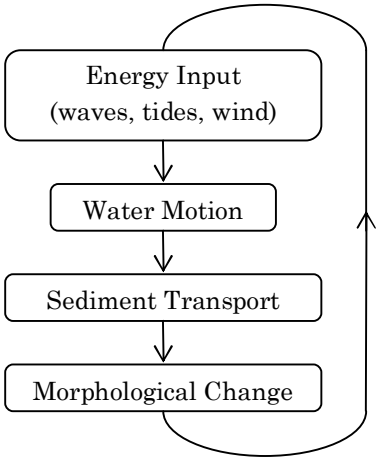

Figure 1.1 The coastal morphodynamic system.

XBeach, developed by *Roelvink et al.* [2007] at the UNESCO|IHE, Deltares and Delft University of Technology, is a numerical model designed to determine the morphological changes induced by storms and hurricanes by combining many decades of research in hydrodynamic and sediment transport modelling. Most models that try to predict morphological change use wave input that is typically within the frequency range of waves generated by wind which is usually between 0.04 and 0.4 Hz. These waves are also known as wind waves, incident waves, short waves or high frequency (HF) waves. XBeach, however, also includes the effects of low frequency (LF) waves which are typically in the range of 0.004 to 0.04 Hz (shown in Figure 1.2). LF waves, also called infragravity waves, surf beat or long waves, were first identified 60 years ago by *Munk* [1949] and have been subject of many studies ever since. For example, low frequency waves have been noted for their effect in harbours, where they can force the resonance of ships if their frequency is similar to the natural frequency of the vessel. LF waves also have an important influence on morphology, which is explained following.

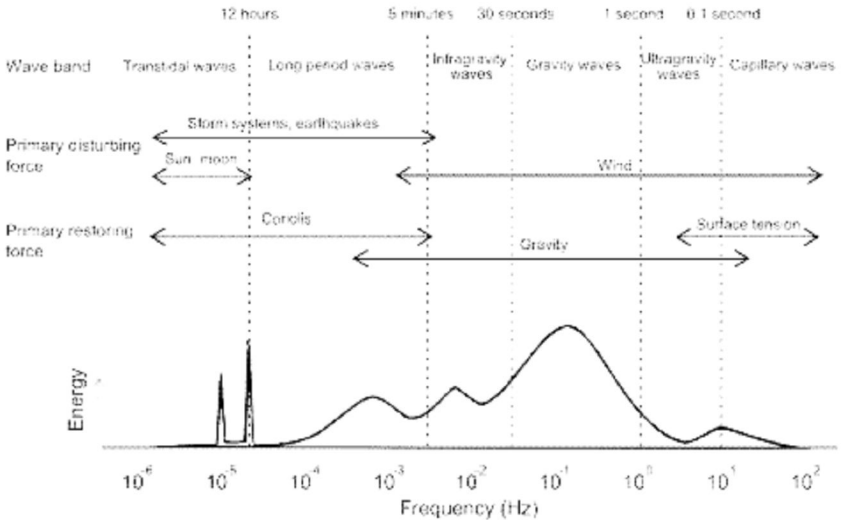

Figure 1.2 Schematic energy spectrum of ocean surface waves (from: *Masselink* and *Hughes* [2003]).

1.1.2 Low Frequency Waves

Munk [1949] observed LF motions well outside the surf zone and named it *surf beat*, suggesting that its cause was due to variations in the mass transport of groups or 'beats' of incident waves in the surf zone. Many studies (e.g. *Longuet-Higgins* and *Stewart* [1962] and *Janssen et al*. [2003]) have theorized and confirmed that LF waves are principally formed by the interaction of steady short wave trains with differing (peak) frequencies, which results in groupiness when superimposed. Small variations in the mean surface elevation over groups of waves are observed, being depressed under high waves (trough) and elevated under lower waves (crest). This resultant LF wave is bound to the short wave groups because it is forced to travel at the same speed as the short wave groups. The bound LF waves are subsequently released as free waves during the short wave breaking process in shallow water, as the groupiness (and thus the forcing) of the short waves disappear. *Symonds et al.* [1982] showed that the changing position of the short wave breakpoint (where higher waves in the wave group break first followed by lower waves) causes variations in the groupiness and is therefore also source of LF wave generation.

LF waves are little affected in the typical shallow water region of the breaking short waves because of their relatively small amplitude and long wavelength. They are freely able to propagate and shoal over a sloping nearshore bathymetry directly to the shoreline where they either break (similar to bores) and directly impact (run-up) the beach or reflect. The LF waves can therefore dominate the wave energy spectrum near the shoreline. Reflected LF waves propagate freely back into the offshore region as leaky waves or they may become trapped in the nearshore as edge waves.

In mild wave climates where LF wave amplitudes are relatively small, their overall effect on morphology has often been ignored, but the hydrodynamics of these waves play an important role in determining morphological changes during storms, schematized in Figure 1.3. The influence of LF waves on morphological changes such as dune erosion, overwash and breaching during extreme conditions is gaining much more attention in recent literature and is currently the subject of much ongoing research.

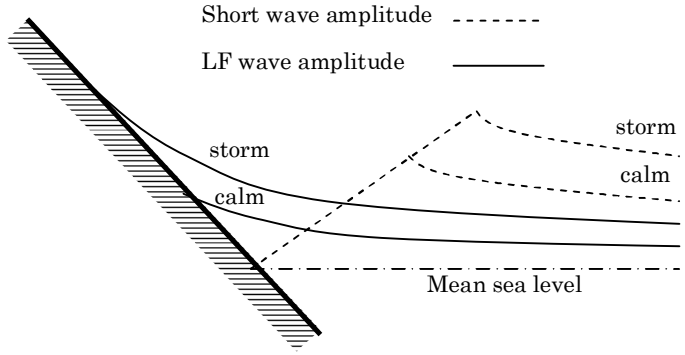

Figure 1.3 Cross-shore change in short and LF wave height during calm and storm conditions (adapted from: *Holman* [1981]).

Battjes et al. [2004] showed that the amplitude growth of the LF waves is due to the transfer of energy from the forcing short waves to the LF waves. This energy transfer is a function of the variation in the groupiness of the waves in the nearshore, which create radiation stress gradients, and also the phase difference between the short wave groups and the bound LF wave. *Van Dongeren et al.* [2007] show that the slope of the nearshore also affects the growth rate of the LF wave and also controls how much of the incident wave is reflected.

1.2 Study Objectives

1.2.1 Problem Description

XBeach is freely available for use by engineers and scientists. The main objective for its development is for it to be used to model, and therefore provide insight into, morphological problems such as dune erosion, overwash and breaching. Validation studies have been done to show the capabilities and possible shortfalls of the model. Despite very good results for most procedures in the model, XBeach is still in the development phase to further improve its capabilities. Such areas for improvement stem from studies which have found that the shoaling and reflection of LF waves may not be predicted well, being over predicted in most cases. Also, morphological predictions of overwash and breaching from XBeach may be overestimated, presumably as a result of the inaccuracies in the LF waves.

1.2.2 Main Objectives

The main objective of this thesis is to validate the hydrodynamics of the XBeach model. To do so, measurements from a flume experiment conducted by *van Noorloos* [2003] will be compared with model results of a replication of the flume experiment in XBeach. In this experiment, bichromatic and irregular waves are propagated in a flume with a fixed plane slope in order to observe the behaviour of the LF waves. The detailed objectives of this validation are therefore to investigate the short wave characteristics and the LF shoaling and reflection results of XBeach. The investigation of short wave characteristics is important as they are the major forcing term of the LF waves. Finally, possible discrepancies in the model results will be investigated to determine the cause, which can then be corrected to improve the XBeach model.

1.2.3 Approach

In keeping with the objectives of this research, the model results from XBeach will be compared to the measurements taken in the experiment of *van Noorloos* [2003]. Before doing so, we will first look at the different components of the XBeach model in order to understand how the model works and to determine what input parameters affect the results most. To make a fair comparison, certain model parameters have to be optimized to obtain results that best replicate the measurements. The sensitivity of these model parameters, such as the input wave height, frequency and breaker parameter, is investigated and ideal values are given in the results. In addition, two different wave breaking parameterizations in the model will be compared with each other in order to determine which gives the best model results for the LF waves.

1.3 Report Outline

Chapter 2 presents an overview of the relevant literature describing the physics of individual short waves and their group structure as well as the generation and shoaling of LF waves. These are all used to determine parameters that are used to judge the performance of XBeach. Chapter 3 explains the program structure and model formulations of XBeach. Within this chapter previous validation studies are also briefly presented. Chapter 4 explains in detail the objectives and approach to the validation study. The setup of both the *van Noorloos* [2003] experiment and the XBeach model is also explained in this chapter. Chapter 5 presents the results of the validation study using the bichromatic wave dataset and Chapter 6 presents the same with regard to the irregular wave dataset. In Chapter 7 the conclusions and recommendations of this thesis are presented. Appendices A to C discuss various data analysis methods that are used with the measured and modelled data to obtain results for comparison. Appendix D gives information about the physical dimensions of the flume and wave gauge locations. Lastly, Appendix E presents additional graphics which are not shown in the main body of the text.

Chapter 2 – Literature Review

In this chapter, the fundamental and important theoretical background related to this research is briefly presented. Section 2.1 presents the theory of short waves and the basic equations used to develop a synthetic timeseries of non-linear bichromatic and irregular wave groups, which is used in Chapter 4. The concept of radiation stress discussed in Section 2.1 is also directly related to Section 2.2 on LF wave theory as it is one of the generating mechanisms of LF waves. The theory of LF waves discussed in Section 2.2 is also important to the validation process described in Chapters 5 and 6.

2.1 Short Wave Theory

The theory and derived equations presented in this subsection are written to be concise and as such has limited background. For further details describing this, the reader is referred to texts by such authors as *Svendsen* [2005] and *Holthuijsen* [2008].

2.1.1 Linear Wave Theory

Linear wave theory, first derived by *G.B. Airy* [1845], forms the basis of understanding how individual waves can be mathematically modelled and how their interactions with other waves and bottom bathymetry through time and space can be predicted to reasonable accuracy. They provide an approximation in deep water where the water depth is greater than the wave length.

If we consider a 2D vertical plane (x, z), as shown in Figure 2.1, and assume waves are propagating over constant depth, h, with constant period, T, with the wave height being much smaller than the wave length ($H/L \ll 1$) and neglecting viscous and turbulent stresses hence making the fluid flow irrotational, the *velocity potential*, φ, can then be introduced based on the continuity equation derived from the mass balance equation as

$$\nabla^2\varphi = \frac{\partial^2\varphi}{\partial x^2} + \frac{\partial^2\varphi}{\partial z^2} = 0\,, \tag{2.1}$$

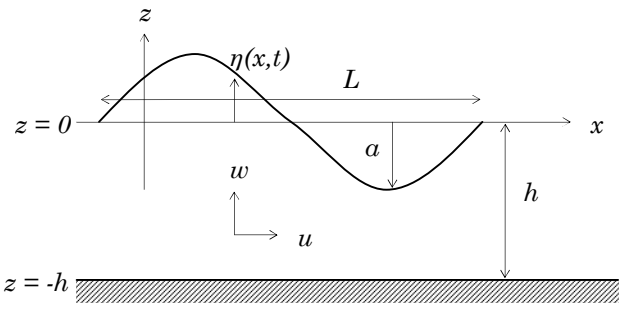

Figure 2.1 Definition sketch of variables.

where ∇ is the gradient operator and (2.1) now satisfies the Laplace equation. The following initial boundary conditions (b.c.) are used to solve the Laplace equation for the velocity potential

$$\frac{\partial \varphi}{\partial z} = 0 \quad \text{at} \quad z = -h \qquad \text{(bottom b.c.),} \tag{2.2}$$

$$\frac{\partial \varphi}{\partial z} - \frac{\partial \eta}{\partial t} = 0 \quad \text{at} \quad z = \eta \qquad \text{(kinematic b.c.),} \tag{2.3}$$

$$\eta + \frac{1}{g}\frac{\partial \varphi}{\partial t} = 0 \quad \text{at} \quad z = \eta \qquad \text{(dynamic b.c.),} \tag{2.4}$$

$$\text{and} \quad \frac{\partial \varphi}{\partial x}(0,z,t) = \frac{\partial \varphi}{\partial x}(L,z,t) \quad \text{for} \quad (-h < z < 0) \qquad \text{(periodicity b.c)} \tag{2.5}$$

where (2.3) and (2.4), representing the kinematic and dynamic conditions at the free surface respectively, have been simplified by eliminating their non-linear terms because of the negligible order of magnitude of the *wave steepness*, ε . The solution yields the velocity potential as

$$\varphi = -\frac{Hc}{2}\frac{\cosh k(z+h)}{\sinh kh}\sin(\omega t - kx), \tag{2.6}$$

where k is the *wave number* defined as

$$k = \frac{2\pi}{L} \tag{2.7}$$

and ω is the *wave frequency* defined as

$$\omega = \frac{2\pi}{T}. \tag{2.8}$$

The *linear dispersion relation*,

$$\omega^2 = gk\tanh kh, \tag{2.9}$$

and the *surface elevation*,

$$\eta_1 = a\cos\theta = \frac{H}{2}\cos(\omega t - kx), \tag{2.10}$$

are also obtained from this solution, where η_1 in (2.10) denotes the linear or first-order contribution to the total surface elevation, η . The *wave celerity* can then be defined as

$$c = \frac{L}{T} = \frac{\omega}{k} = \sqrt{gh}\left(\frac{\tanh kh}{kh}\right)^{1/2}, \tag{2.11}$$

which can also be written in terms of the dispersion relation as

$$c = \frac{gT}{2\pi}\tanh kh = \frac{g}{\omega}\tanh kh. \tag{2.12}$$

In deep water ($h > L/2$ or $kh \gg 1$) the waves are short compared to the depth and the celerity, dependent on the wave period (or wave frequency), is determined by

$$c = \frac{gT}{2\pi} = \frac{g}{\omega}. \tag{2.13}$$

In shallow water ($h < L/2$ or $kh \ll 1$), the waves are long compared to the depth and their celerity is limited by the water depth, given as

$$c = \sqrt{gh} \,. \tag{2.14}$$

2.1.2 Second-order Stokes Theory

While linear wave theory is a good first order approximation of the velocity potential and surface elevation, it does not give insight into the peaked shape of the wave. To determine this, the non-linear terms have to be added in order to resolve the phase variation of the waves. *Stokes*' [1847] wave theory is the oldest of the non-linear wave theories. The theory considers all of the higher order components of waves, however, in this thesis we only to go as far as the second order so as to match the wave input used in the experiment of *van Noorloos* [2003].

In linear wave theory, the assumption that the order of magnitude (O) of H/L is negligible has lead to the elimination of the non-linear terms in the kinematic and dynamic conditions at the free surface. *Stokes* [1847], however, uses this term to expand the quantities in a power series while also assuming that $kh = O(1)$. Using the same initial boundary conditions for linear wave theory and solving the Laplace equation we obtain the solution for the *second-order velocity potential* as

$$\varphi = -\frac{3}{32} ckH^2 \frac{\cosh 2k(z+h)}{\sinh^4 kh} \sin 2(\omega t - kx) + Kx \,. \tag{2.15}$$

The second-order component of the total surface elevation is then given as

$$\eta_2 = \frac{ka^2}{4}\left(3\coth^2 kh - \coth kh\right)\cos 2(\omega t - kx) \,. \tag{2.16}$$

The second order approximation for the wave motion is a *forced oscillation* generated or forced by the first order wave. As seen by the term $-\frac{3}{32}\frac{c^2}{k}(kH)^2 \frac{\cosh 2kh}{\sinh^4 kh}$ in (2.15), the amplitude cannot be chosen freely and it is fixed by the magnitude of the first-order term. The frequency of the second-order term is also a multiple 2 of the fist-order wave frequency. The total surface elevation is given as the linear superposition of the first- and second-order component, (2.10) and (2.16) respectively, such that

$$\eta = \eta_1 + \eta_2 = \eta_1 + \frac{ka^2}{4}\left(3\coth^2 kh - \coth kh\right)\cos 2(\omega t - kx) \tag{2.17}$$

and $$\eta = \eta_1 + \eta_2 = a_1\left(\cos(\omega t - kx) + \frac{3}{32\pi^2}\frac{HL^2}{h^3}\cos 2(\omega t - kx)\right) \tag{2.18}$$

The combined effect of the first and second order terms gives the impression that the wave profile is shifted upwards relative to the mean water level, as shown in Figure 2.2, although the wave remains symmetric, the height remains constant and the spatial average over one period remains zero.

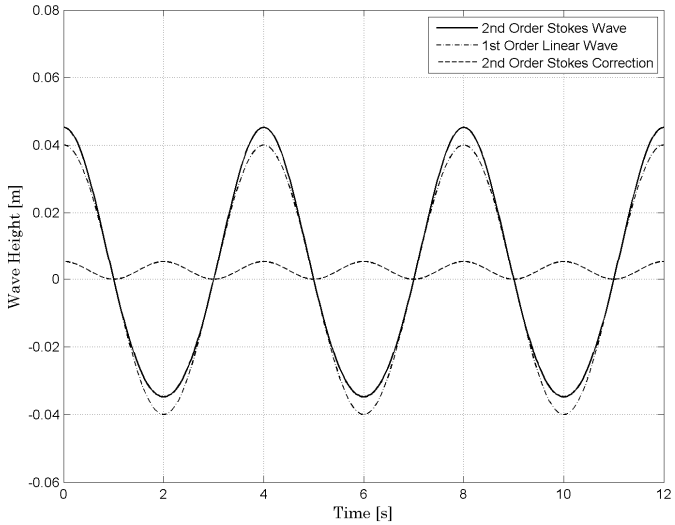

Figure 2.2: Second-order waves using Stokes theory.

In (2.15) the term Kx represents a steady uniform flow velocity, U, related to the volume flux of the wave and is given as (to second-order)

$$K = U = -\frac{1}{8} g \frac{H^2}{c} \tag{2.19}$$

and $$U = -\frac{Q_w}{h} \tag{2.20}$$

where Q_w is generally termed Stokes drift. When U is added to wave celerity (2.11), it defines the actual speed of the wave with a current. This is also the case for other sources of currents, such as those associated with tides.

2.1.3 Non-linear Shallow Water Waves

In deep water ($h > L/2$ or $kh \gg 1$), waves can be described very well with both linear and Stokes wave theories, as the relative order of magnitude of the non-linear terms are negligible. In transitional waters ($h \approx L/2$ or $kh \approx 1$), due to the shoaling of waves, linear theory becomes slightly less accurate while Stokes theory up to second order is still capable of accounting for the increasing non-linearities. As waves move into shallower waters ($h < L/2$ or $kh \ll 1$), their shape changes and they no longer remain symmetric about the horizontal x-axis. The assumption that $h/L = O(1)$ is no longer valid and different sets of equations are necessary to define the shape of the wave. In this region, the wave theories developed by *Boussinesq* [1872] and *Korteweg de Vries* [1895], where h/L is assumed small, are suitable descriptors, with the latter theory commonly known as *cnoidal wave theory*.

The *Ursell parameter*, *Ur*, proposed by *Ursell* [1953] but originally pointed out by *Stokes* [1847], is theoretically found to be a good measure of the degree of non-linearity present in waves. Three wave cases can be distinguished as follows

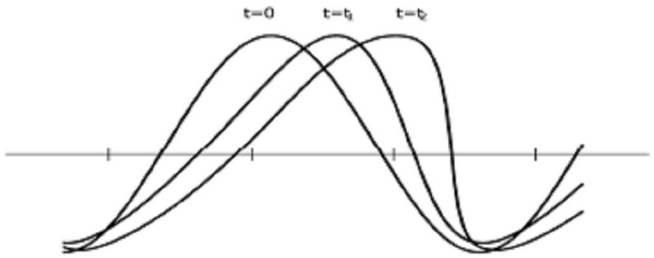

Figure 2.3: An initial sinusoidal disturbance propagated with the NSW equations steepen the wave until the front slope has become almost vertical (taken from: Smit [2008]).

$$Ur \equiv \frac{HL^2}{h^3}\begin{cases} \ll O(1) & \text{linear shallow water waves} \\ = O(1) & \text{cnoidal solitary waves} \\ \gg O(1) & \text{non-linear shallow water waves} \end{cases} \tag{2.21}$$

For the third case ($Ur \gg O(1)$), the *non-linear shallow water* (NSW) equations may be used to describe the waves when the wave height is the same order as the water depth ($H/h = O(1)$). In this shallow water region the trough of the wave travels with a celerity $c_{trough} = \sqrt{g\left(h - a_{trough}\right)}$ while the crest travels with $c_{crest} = \sqrt{g\left(h + a_{crest}\right)}$. The crest therefore travels at a greater speed than the trough and eventually it will catch up with the trough of the previous wave. The NSW equations, given as

$$\frac{\partial}{\partial t}\eta + \nabla\left(\tilde{\mathbf{u}}\left(h+\eta\right)\right) = 0 \tag{2.22}$$

and $$\frac{\partial}{\partial t}\tilde{\mathbf{u}} + \tilde{\mathbf{u}}\cdot\nabla\tilde{\mathbf{u}} + g\nabla\eta = 0 \tag{2.23}$$

where is $\tilde{\mathbf{u}}$ the depth averaged horizontal velocity, conserve mass and momentum. To accurately represent wave breaking in shallow water, an additional scheme may be required to dissipate energy. Such a scheme can allow the wave front to steepen until it is almost vertical, interpreted as the breaking of the wave which is similar to the propagation of a bore, as shown in Figure 2.3.

2.1.4 Bichromatic Wave Groups

The simplest form of a progressive wave group is obtained by the superposition of two primary waves with slightly different frequencies, resulting in a so-called beat pattern. In the simple case of two linear waves being superimposed with each other, the pattern formed has two wave-type features. First, the superimposed primary waves result in a spatial and temporal variance of the surface elevation (a resultant wave) which itself propagates with a velocity equivalent to the mean of the two primary waves. Secondly, there is an envelope of the resultant wave representing its group structure. The properties of these waves are given as

$$\begin{aligned} \omega_m &= \frac{\omega_1 + \omega_2}{2} \\ \omega_g &= \frac{\omega_1 - \omega_2}{2} \end{aligned} \tag{2.24}$$

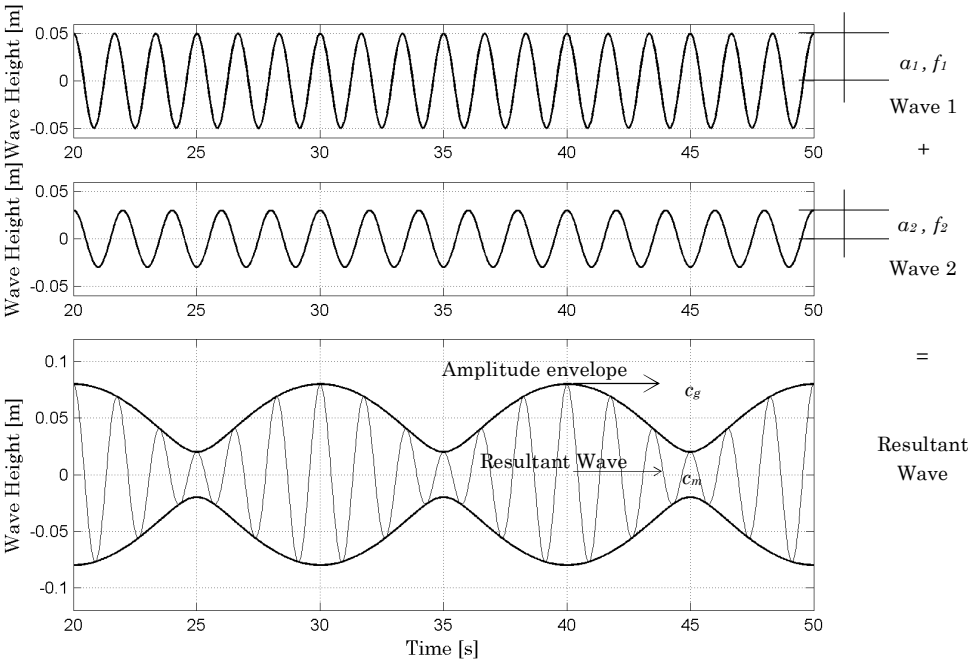

Figure 2.4: The time-varying individual waves and amplitude envelope of a linear wave group.

$$k_m = \frac{k_1 + k_2}{2}$$
$$k_g = \frac{k_1 - k_2}{2} \tag{2.25}$$

$$c_m = \frac{\omega_m}{k_m} = \frac{\omega_1 + \omega_2}{k_1 + k_2}$$
$$c_g = \frac{\omega_g}{k_g} = \frac{\omega_1 - \omega_2}{k_1 - k_2} \tag{2.26}$$

where the subscripts 'm' and 'g' denote parameters associated to the representative mean individual wave and the envelope of the wave group respectively, shown in Figure 2.4. We can rewrite the set (2.26) in terms of (2.11) as

$$c_m = \frac{\bar{\omega}}{\bar{k}} = \sqrt{gh}\left(\frac{\tanh k_m h}{k_m h}\right)^{1/2} \tag{2.27}$$

$$\text{and thus} \quad c_g \equiv \frac{\partial \omega}{\partial k} \approx c_m\left(\frac{1}{2} + \frac{k_g h}{\sinh 2k_g h}\right) = n \cdot c_m \tag{2.28}$$

As shown in (2.28), the group velocity, c_g, is lower than the velocity of the individual waves, c_m, in deepwater (n = 0.5), however in shallow water, the linear dispersion relation (2.9) limits the value of both c_g and c_m to $\sqrt{gh}$, therefore, they converge towards the waterline (n = 1).

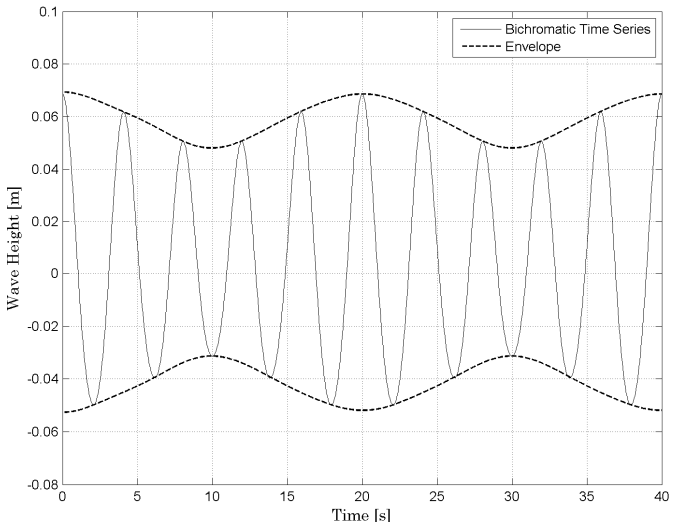

Figure 2.5: Second-order bichromatic wave group.

A representative period of the resultant short wave is given as

$$T_m = \frac{2\pi}{\omega_m} = \frac{2T_1T_2}{T_1 + T_2} \tag{2.29}$$

and its modulation is determined by

$$\delta = \frac{a_2}{a_1} \tag{2.30}$$

where a_1 is greater than a_2. A groupiness factor [*List* (1992)] can be used to describe the amplitude envelope timeseries as

$$G_f = \frac{\sqrt{2}\sigma_A}{\overline{A(t)}} \tag{2.31}$$

where A is the amplitude envelope of the resultant short wave. The method to determine the amplitude envelope is outlined in Appendix 2.

A bichromatic wave is composed of the superposition of two linear waves with nearly the same frequencies plus their non-linear terms, as shown in Figure 2.5. Considering the effects of non-linearities up to second order, the superposition produces two bound interaction waves: a high and low frequency component. The celerity of the individual and group waves are the same as those determined for linear waves in (2.26), however, the influence of the uniform flow velocity defined in (2.19) alters the observed velocity of the individual waves and thus the wave group.

2.1.5 Energy Density and Radiation Stress

The energy content of waves can be measured over a unit surface area, termed the energy density. The energy density naturally consists of potential and kinetic components. The *potential energy density* is measured relative the reference elevation $z = 0$ and considers only the fluid from z to the surface (i.e. neglecting the potential energy of the fluid below at rest), such that

$$E_p = \int_0^{\eta} \rho g z \, dz = \frac{1}{2}\rho g \overline{\eta^2} = \frac{1}{16}\rho g H^2 . \tag{2.32}$$

The *kinetic energy density* is determined by first obtaining the kinetic energy density per unit volume of fluid, given as

$$e_k = \frac{1}{2}\rho\left(u^2 + w^2\right), \tag{2.33}$$

and then integrating the instantaneous value over the water depth and subsequently averaging over one wave period. This is given as

$$E_k = \overline{\int_{-h}^{\eta} e_k(t) \, dz} = \frac{1}{16}\rho g H^2 . \tag{2.34}$$

The *total energy density* is then given as the summation of the potential and kinetic energy components,

$$E = E_p + E_k = \frac{1}{8}\rho g H^2 . \tag{2.35}$$

This energy propagates with the speed of the wave groups, which determines the *energy flux* as

$$E_f = c_g E . \tag{2.36}$$

In addition, the momentum of the waves is also transported with the wave groups which can be represented in terms of the force exerted on the water column by the waves. *Radiation stress* is defined as the mean momentum flux caused by the waves only. Considering the momentum flux in the cross-shore (x) direction, the radiation stress is defined as

$$S_{xx} = \overline{\int_{-h}^{\eta}\left(\rho u^2 + p\right) dz} - \frac{1}{2}\rho g h^2 \tag{2.37}$$

where the last term in the equation represents the subtraction of the part due to the hydrostatic pressure. The portion within the integral is a combination of momentum and pressure terms. Integrating each term over the wave group yields

$$S_{xx} = S_m + S_p = \frac{1}{16}\rho g {H_{rms}}^2 \left(1 + 2\frac{2kh}{\sinh 2kh}\right) \tag{2.38}$$

which can be written in terms the energy density, correct to second order, as

$$S_{xx} = E\left(\frac{2c_g}{c} - \frac{1}{2}\right) \tag{2.39}$$

2.1.6 Wave Spectrum and Irregular Wave Groups

In the subsections above, we have described the basic theory of individual waves and wave groups of simple structure. In reality, there exist innumerable individual waves of varying amplitude and frequency all superimposed to produce a complex wave field. For a given timeseries, we can write the surface elevation in terms of this summation as

$$\eta(t) = \sum_{i=1}^{N} a_i \cos\left(2\pi f_i + \theta_i\right) \tag{2.40}$$

We can determine the *variance density* as a function of frequency and in terms of the wave amplitude as

$$E(f) = \lim_{\Delta f \to 0} \frac{1}{\Delta f_i} \overline{\frac{1}{2} a^2} \tag{2.41}$$

where the overbars denote the expected value of the underlying terms. It is important to note the difference between (2.35) and (2.41), where $E = \rho g E(f)$. From (2.41) we obtain a spectrum of the variance density of the waves, from which *spectral moments* are defined as

$$m_n = \int_0^\infty f^n E(f)\ df \tag{2.42}$$

where n is an integer. Some important spectral parameters of the surface elevation timeseries obtained from spectral moments are the *variance*, given as

$$m_0 = \int_0^\infty E(f)\ df \tag{2.43}$$

the *standard deviation*, given as

$$\sigma = \sqrt{m_0} \tag{2.44}$$

the *significant wave height*, given as

$$H_{m_0} = 4.004\sqrt{m_0} \approx 4\sigma \tag{2.45}$$

the *peak period*, given as

$$T_p = f\left(\max\left[E(f)\right]\right)^{-1} \tag{2.46}$$

and the *mean zero-crossing period*, given as

$$T_{m01} = \sqrt{\frac{m_0}{m_2}} \tag{2.47}$$

Spectral analysis yields good insight into the structure of the individual (discrete) frequency components of a complex wave field. It can be shown that typical wave fields at sea can be described by a predefined wave energy variance spectrum. The *JONSWAP* spectrum [*Hasselman et al.* (1973)] is one such, which is a modification of the *Pierson-Moskowitz* [1964] spectrum and is given as

$$E(f) = \underbrace{\underbrace{\alpha g^2 (2\pi)^{-4} f^{-5} \exp\left[-\frac{5}{4}\left(\frac{f}{f_{peak}}\right)^{-4}\right]}_{\text{Pierson-Moskowitz}} \gamma^{\exp\left[-\frac{1}{2}\left(\frac{f/f_{peak}^{-1}}{\sigma}\right)^2\right]}}_{\text{JONSWAP}} \tag{2.48}$$

where the defining parameters are the *peak frequency*, f_p, obtained from the peak period and the significant wave height. The JONSWAP spectrum does not include the phase spectrum information of the waves, and therefore a timeseries obtained from the JONSWAP spectrum has to employ a random phase component. The randomness of the phase therefore makes the timeseries irregular. Realizations generated using the same JONSWAP spectral parameters will

not necessarily be synchronous with each other at the same point in time although they share the same spectral parameters.

2.2 Low Frequency Wave Theory

Low frequency (LF) waves were first identified sixty years ago by *Munk* [1949]. He called the waves *surf beat* as he believed that they were generated in the surf zone by groups or 'beats' of waves. These waves are also commonly known as *infragravity waves* and *long waves*. The term infragravity is somewhat incorrect, as it suggests that the waves are lie outside of the frequency range of gravity waves, when this is not the case. In addition to describing LF waves, the term '*long wave*' is also used widely to represent *any* wave in which its wavelength, L, is long compared to the water depth, h, including waves freely generated by wind or from other sources. In this thesis we will therefore refrain from using the latter two terms and give preference to the term *low frequency wave* for our descriptions.

In general, LF waves are highly correlated to energy in the short wave band, therefore LF wave motions are locally driven by sea and swell. *Ruessink* [1998] explains that there are three known generation mechanisms for LF waves:

1. Release of bound LF waves [*Longuet-Higgins* and *Stewart* (1962)].
2. Time-varying position of the breakpoint [*Symonds et al.* (1982)].
3. Persistence of groupiness into the surf zone [*Schäffer* and *Svendsen* (1988)].

Some authors (*List* [1992], *Roelvink* [1993]) have found that (1) is a major source according to their models for dissipative beaches or during high energy conditions. These LF waves are often referred to as forced or bound LF waves. (2) and (3) describe generation mechanisms for free LF waves. In the following sub-sections we will describe these generation mechanisms.

2.2.1 Forced Generation of Low Frequency Waves

2.2.1.1 Generation by Radiation Stress Gradients

Longuet-Higgins and *Stewart* [1962] showed that changes in the mean surface elevation and in the mass transport are produced by changes in the radiation stress gradient ($-\partial S_{xx}/\partial x$) of the fluid. The radiation stress is shown to be greater under groups of high waves, which tends to expel fluid from that region. This is shown figuratively in Figure 2.6 following.

Given that the variation of LF waves occur over the length scale of the short wave group, the waves are effectively long compared to water depth in the shoaling and nearshore zone of the short waves. The conservation of mass and momentum can therefore be applied in the form of the NSW equations given in (2.22) and (2.23). The momentum equation given by (2.23) can be rewritten to include the radiation stress tensor and a dissipative term accounting for shear stresses from the bed as

$$\frac{\partial}{\partial t}\tilde{\mathbf{u}} + \tilde{\mathbf{u}}\cdot\nabla\tilde{\mathbf{u}} + g\nabla\zeta = -\frac{1}{\rho(h+\zeta)}\nabla S_{xx} + \frac{\tau_b}{\rho h} \tag{2.49}$$

where τ_b is the bed shear stress and ζ now represents the surface elevation averaged over the short wave period, treated separately from η.

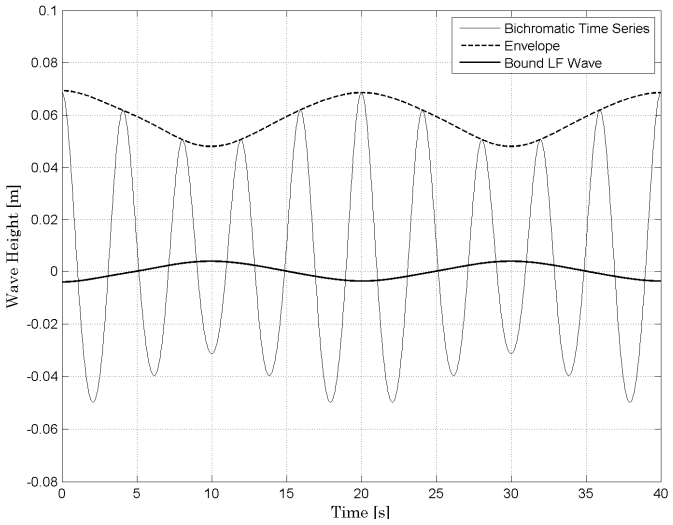

Figure 2.6: Bichromatic wave group with its corresponding bound LF wave.

Assuming $\zeta \ll h$, these non-linear equations can be linearized to give

$$\frac{\partial}{\partial t}\zeta + \nabla\left(\tilde{\mathbf{u}}h\right) = 0 \tag{2.50}$$

and $$\frac{\partial}{\partial t}\tilde{\mathbf{u}} + g\nabla\zeta = -\frac{1}{\rho h}\nabla S_{xx} + \frac{\tau_b}{\rho h} \tag{2.51}$$

In (2.28) we see that the amplitude envelope travels at the group velocity, c_g. We can, therefore, further simplify (2.50) and (2.51), assuming a horizontal profile, as

$$-c_g\nabla\zeta + h\nabla\tilde{\mathbf{u}} = 0 \tag{2.52}$$

and $$-c_g\nabla\tilde{\mathbf{u}} + g\nabla\zeta = -\frac{1}{\rho h}\nabla S_{xx} + \frac{\tau_b}{\rho h} \tag{2.53}$$

Longuet-Higgins and *Stewart* [1962] derived the expression of the mean surface elevation in terms of the radiation stress by eliminating **u** and integrating with respect to x as

$$\bar{\zeta} = -\frac{S_{xx}}{\rho\left(gh - c_g^2\right)} \tag{2.54}$$

For this steady state condition, if there is no energy loss, then as the depth becomes shallower, the time-averaged water level is depressed (set-down). During and after breaking, where energy is lost, the mean level rises (set-up). The derivation is applicable to stationary conditions and is limited in its use to only horizontal bathymetries where energy is conserved and thus dissipation is limited.

Also shown in Figure 2.6, the bound LF wave is in anti-phase with the envelope of the short waves (red). This phase difference of $-\pi$ (180 degrees) is also noted in field measurements as a negative correlation.

2.2.1.2 Energy Transfer

Given that the LF waves are generated by changes in the forcing of the short waves, *Battjes et al.* [2004] determined the rate of energy transfer to the LF waves as

$$\frac{dF}{dx} = R \equiv -\left\langle U \frac{dS_{xx}}{dx} \right\rangle \tag{2.55}$$

where R is rate of energy transfer per unit area from the short waves to the LF waves, U is the depth-averaged LF particle velocity and the brackets denote phase averaging. The above equation can be rewritten as

$$R \cong \frac{1}{2}\kappa \hat{U}\hat{S}\sin(\Delta\psi) \tag{2.56}$$

where $\hat{U}$ and $\hat{S}$ denote the real amplitudes of U and S_{xx} respectively, κ is the LF wave number given as

$$\kappa = \frac{2\pi f}{c_g} \tag{2.57}$$

and $\Delta\psi$ is the phase lag of the LF wave behind the short wave envelope, given as

$$\Delta\psi = \arg\left(\frac{\eta(t)}{\zeta_{in}(t)}\right) - \pi \tag{2.58}$$

The $-\pi$ in (2.58) compensates for the normal 180 degree phase difference between the short wave envelope and the bound LF wave. According to (2.56), energy transfer to the LF waves does not occur at integer multiples of π when the short wave envelope and LF wave are in (anti)phase, or if the amplitude of the radiation stress gradient is zero.

The phase lag is a unique corollary to the term 'bound LF wave' as phase differences greater than zero indicate that the short wave envelope is leading the LF wave. The term 'bound' is used when the LF waves and short waves travel at the same speed, which is the case for waves in deep water. For this reason, the term 'forced' is normally used to indicate the fact the LF waves are not directly bound to the short waves.

2.2.2 Free Generation of Low Frequency Waves

2.2.2.1 Generation by Time-Varying Breakpoint

Symonds et al. [1982] proposed that the movement in the breakpoint over a wave group, caused by the initial breaking of the higher waves followed by the breaking of the lower waves in shallower water closer to the shoreline, is able to generate free waves on the timescale of the wave groups. It is assumed that the amplitude of the breaking wave decreases linearly toward the shoreline and the groupiness of the waves are destroyed during the breaking process. The radiation stress gradients fluctuate and therefore induce variations in the water surface elevation (as initially described by *Longuet-Higgin*s and *Stewart*). The water level disturbance caused can be visualized in a manner similar to a wave generator which produces waves on either side, thus a shoreward and a seaward propagating LF wave.

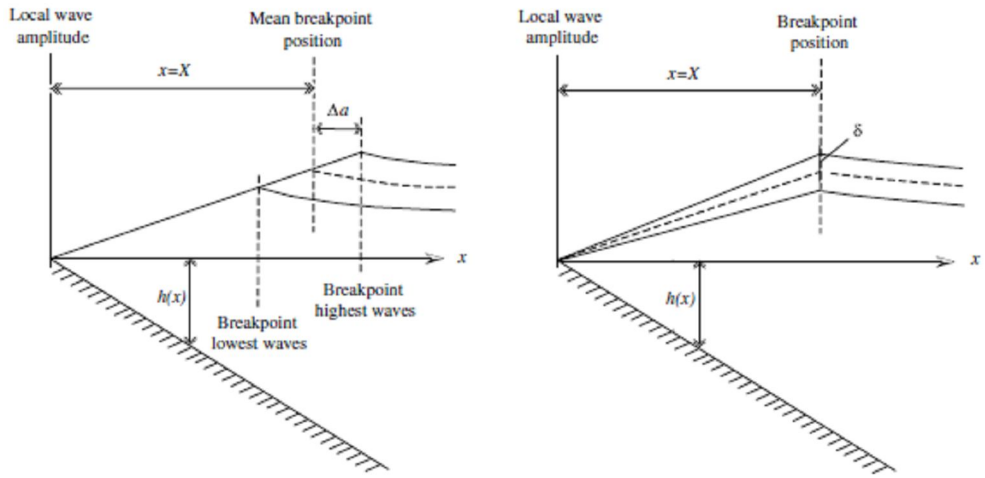

Figure 2.7: LF wave generation by a time-varying (left) and fixed (right) breakpoint (taken from *van Noorloos* [2003]).

The shoreward propagating wave is then assumed to be reflected at the shoreline, where it subsequently interacts with the seaward propagating wave creating a standing wave pattern. The normalized surf zone width, χ, proposed by *Symonds et al.* [1982], given as

$$\chi = \frac{\omega_g{}^2 h_b}{g h_x^2} \tag{2.59}$$

where ω_g is the group frequency, h_x is the bed slope and h_b is the mean depth at the breakpoint, is used to describe the relative phase difference between these waves.

2.2.2.2 Generation by Fixed Breakpoint

Schäffer and *Svendsen* [1988] present a model to represent the generation of LF waves by a fixed break point. Here, it is assumed that the groupiness of the short waves reaches inside the surf zone, causing rising and falling masses of water at the shoreline. A schematization of the time-varying and fixed breakpoint models are presented in Figure 2.7.

2.2.2.3 Hybrid Model

Later, *Schäffer* [1993] presents a hybrid model of the fixed and moving breakpoint generation mechanisms which allows for the variation of the initial breakpoint position while allowing groupiness into the surf zone. Incoming bound LF waves are also considered, which are not in the original model by *Symonds et al.* [1982]. The modulation of the short wave group has an influence on the amplitude of the LF wave generated by these mechanisms. *Schäffer* [1993] determines a weighting parameter, κ (different from (2.57)), which determines the relative importance of each type of free LF wave generation as

$$\kappa = 1 - \frac{\partial \log \gamma}{\partial \log \varepsilon_\infty} \tag{2.60}$$

where γ is the breaker parameter and ε_∞ is the deepwater wave steepness. For $\kappa = 1$, the time-varying breakpoint model is assumed and, conversely, for $\kappa = 0$ the fixed breakpoint model is assumed.

2.2.3 Shoaling and Reflection of Low Frequency Waves

2.2.3.1 Shoaling Limits

The amplitude growth of bound LF waves during the shoaling of the forcing short wave groups is a consequence of the transfer of energy to the LF wave from the short waves. The rate of shoaling of LF waves can be fitted to a function of local depth, such that

$$\hat{\zeta} = h^{-a} \tag{2.61}$$

Battjes et al. [2004] concluded that shoaling (and de-shoaling) of LF waves lies between a lower limit, given by Green's Law for free LF waves where $a = 0.25$, and an upper limit, given as the shallow water limit determined by *Longuet-Higgins* and *Stewart* [1964] where $a = 2.5$.

LF waves are released as free waves when the wave groups forcing them change rapidly, such as during breaking in the surf zone. At this point, the shoaling of the LF waves may temporarily cease until the wave propagates further into water depths comparable to its height, upon which they may begin to re-shoal and break similar to bores.

2.2.3.2 Normalized Bed Slope

Battjes et al. [2004] also found that the shoaling rate of LF wave increases with frequency. This is due to a given bed slope appearing steeper to longer waves than for shorter waves because the former experiences a greater change in depth over one wavelength than the latter. Thus, a dimensionless normalized bed slope parameter which gives an indication of the depth change per wavelength was determined as

$$\beta = \frac{h_x}{\omega}\sqrt{\frac{g}{h}} \tag{2.62}$$

where h_x is the bed slope and value of h depends on the region in which it is used. For incoming bound LF waves, h is taken as the depth at the characteristic breaker line and the normalized bed slope is then styled β_b.

Van Dongeren et al. [2007] concluded that β_b determines the growth rate and dissipation of the LF waves at the shoreline, where it is observed that for large values of β_b ($\beta_b > 0.45$ being a steep slope regime) the growth rate is small and the waves are nearly fully reflected. The converse is observed for small values of β_b ($\beta_b < 0.1$ being a mild slope regime), where there is a large growth rate of the incoming bound waves and very little associated reflection due to the breaking of the waves. The shoreline reflection is empirically related to β_b [following *Battjes* (1974)] such that

$$R_f = 0.2\pi\beta_H^2 \tag{2.63}$$

It can also be seen that β_b is closely related to χ in (2.59) such that $\chi = \beta_b^{-2}$.

Depending on the angle of incidence of the LF waves, the reflected free LF (RFLF) wave from the shoreline propagates seaward. Edge waves form if the RFLF waves are reflected an angle to the normal of the coast, which allows it to refract and curve back towards the shore. Leaky waves are RFLF waves which are able to escape into the open waters provided that their initial angle of incidence to the shore is (close to) normal.

Chapter 3 – The XBeach Model

This chapter presents a brief introduction to the XBeach model. The main objective XBeach, developed by the joint forces of the UNESCO|IHE, Deltares and Delft University of Technology, is to provide a robust and flexible environment in which to test morphological modelling concepts for the case of dune erosion, overwash and breaching. The program contains a number of Fortran 90/95 routines for short wave propagation, non-linear shallow water equations, sediment transport and coupled morphology that are designed to cope with extreme conditions such as those encountered during hurricanes. The model has already been validated against a number of analytical, laboratory and field tests, including hydro- and morphodynamics. In Section 3.1 of this Chapter, the numerical structure of XBeach is presented. In Section 3.2, the formulations which are used by the different routines of the model are shown, followed by a brief overview of previous validation studies in Section 3.3. For detailed information on the XBeach model, the reader is referred to the XBeach Manual [*Roelvink et al.* (2007)].

3.1 Numerical Scheme and Program Structure

3.1.1 General

One of the top priorities of XBeach is to provide numerical stability. First order accuracy is accepted since there is a need for small spatial and temporal steps to represent the strong gradients in space and time in the nearshore and swash zone. XBeach uses a similar approach as models such as HISWA [*Holthuijsen et al.* (1989)], SHORECIRC [*van Dongeren et al.* (1994)] and SURFBEAT [*Roelvink* (1993)] for the modelling of short and LF waves. The model equations are solved assuming that the wave energy imposed at the model boundary is propagating toward the shoreline (an 'upwind schematization') as a means to avoid numerical oscillations in the hydrodynamics and morphodynamics, especially in shallow areas, which is acceptable without too much damping. Since length scales are short in terms of wave lengths and supercritical flow frequently occurs, the upwind numerical implementation in combination with separate but aligned grids for wave action and flow (a staggered grid) makes the model robust. The model utilizes explicit schemes with an automatic time step based on Courant criterion, with output at fixed or user defined time intervals.

3.1.2 Functionalities

The XBeach model has the following functions:

- Time-varying wave action balance including refraction, shoaling and wave breaking;
- Roller and wave dissipation model for use when the wave energy varies on the wave group timescale (non-stationary wave energy balance);
- Depth-averaged shallow water equations that include time-varying wave forcing terms;

- Depth-averaged advection-diffusion equation to solve suspended transport and Soulsby – Van Rijn transport formulations;
- Bed updating algorithm including possibility of avalanching with separate criteria for critical slope at wet or dry points;
- Numerical scheme to improve long-wave run-up and backwash on the beach;
- Generalised Lagrangean Mean (GLM) approach to represent the depth-averaged undertow and its effect on bed shear stresses and sediment transport.

3.1.3 Modules

The different functionalities in XBeach are divided amongst a number of modules. There are four main modules in XBeach. Figure 3.1 outlines these different components and some of the functions which are associated with each. Arrows indicate the connectivity of the modules, where an arrow going from one module 'A' to another module 'B' indicates the use of output parameters from module 'A' in module 'B'. In a single numerical time step each of the modules are called in sequence starting with the short wave module. The flow module uses the radiation stress gradients given as output from the short wave module for its computations. Wave and current output from the short wave and flow modules are used in the sediment transport module, after which the morphology is determined using output from the flow and sediment transport modules.

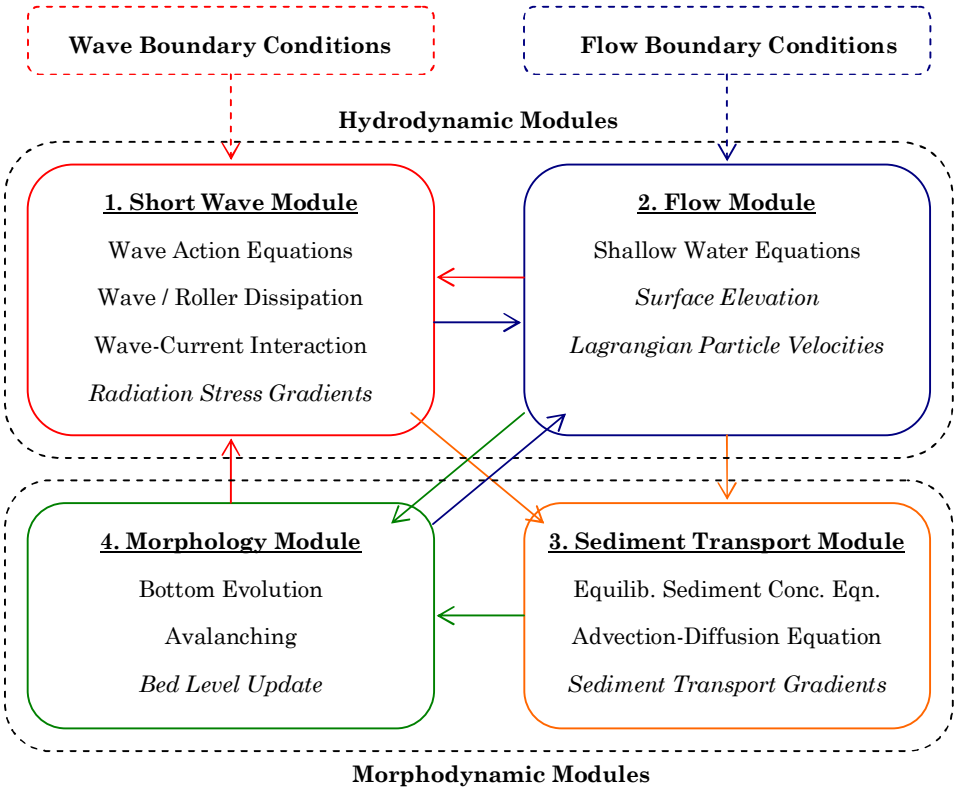

Figure 3.1: Component modules in XBeach. Arrows indicate connectivity and terms in italics indicate relevant output parameters. The black dotted lines encompass the hydrodynamic (top) and morphodynamic (bottom) modules. Boundary conditions are only used in the first cycle.

In the new time-step, the short waves module uses output from the morphology and flow modules, given that the bed levels and surface elevations change per time-step. The hydrodynamic computations of XBeach are contained within the short wave and flow modules.

3.2 Model Physics and Formulations

This section briefly states the relevant formulations used in the different routines of XBeach. Since we will try to validate XBeach against 1D flume data in Chapters 4 and 5, only formulations pertaining to the computational *x*-direction and without the consideration of directional spreading is presented where convenient. Much of the text and formulae presented is a summarized version of the XBeach User Manual.

3.2.1 Coordinate System and Grid Setup

The coordinate system used by XBeach has the computational *x*-axis oriented (approximately perpendicular) towards the coast, and the y-axis alongshore. It is defined relative to world coordinates (xw,yw)[1] through the origin (xori,yori) and the counter-clockwise orientation (alfa), defined w.r.t. the xw-axis. The grid size in *x*- and *y*-direction may be variable but the grid must be rectilinear. Figure 3.2 shows a definition sketch of these variables.

The grid applied is a staggered grid, where the bed levels, water levels, water depths and concentrations are defined in cell centres, and velocities and sediment transports are defined in u- and v-points, that is to say, at the cell interfaces. In the wave energy balance, the energy, roller energy and radiation stress are defined at the cell centres, whereas the radiation stress gradients are defined at u- and v-points. The water level, zs, and the bed level, zb, are both defined positive upward.

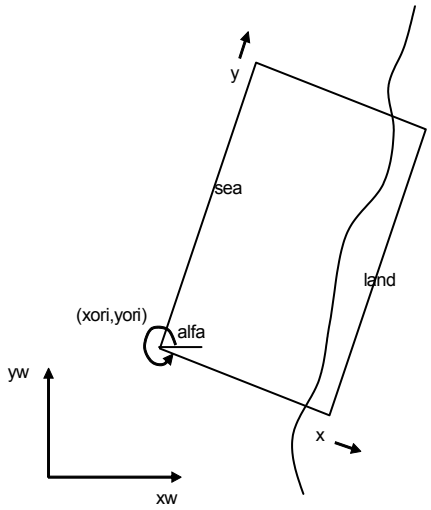

Figure 3.2: Coordinate system in XBeach.

[1] Keywords and parameter names corresponding to input and output from XBeach are written in a different font type to highlight it from within the body text.

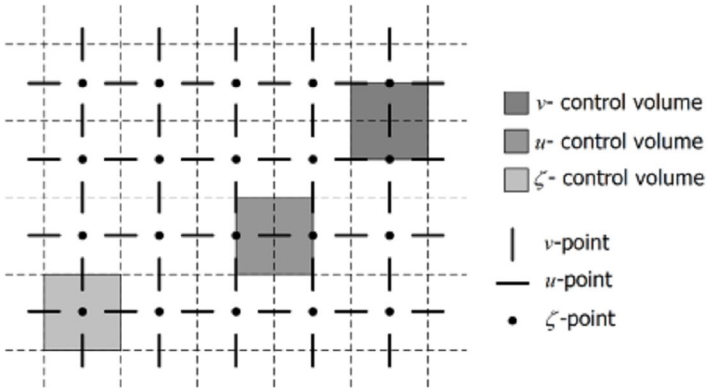

Figure 3.3: Staggered grid in XBeach.

Velocities at the u- and v-points are denoted by uu and vv respectively; velocities u and v at the cell centres are obtained by interpolation and are for output purpose only. uv and vu are the u-velocity at the v-grid point and the v-velocity at the u-grid point respectively. These are obtained by interpolation of the values of the velocities at the four surrounding grid points. Figure 3.3 gives a schematic representation of this.

3.2.2 Hydrodynamics

3.2.2.1 Wave Action Balance

The model is forced using a time dependent version of the wave action balance equation in shallow water, similar to the HISWA model. The directional distribution of the action density is accounted for and the frequency spectrum is represented by a single representative frequency. The wave action balance is given as

$$\frac{\partial A}{\partial t}+\frac{\partial c_x A}{\partial x}+\frac{\partial c_y A}{\partial y}+\frac{\partial c_\theta A}{\partial \theta}=-\frac{D}{\sigma} \tag{3.1}$$

where D is the wave dissipation due to wave breaking, and with the wave action given as

$$A(x,y,\theta)=\frac{E_{waves}(x,y,\theta)}{\sigma(x,y)} \tag{3.2}$$

where E_{waves} is the wave energy in each directional bin and σ the intrinsic wave frequency. The wave action propagation speeds in the x-direction is obtained from linear wave theory as

$$c_g=nc=\left(\frac{1}{2}+\frac{kh}{\sinh 2kh}\right)\frac{\sigma}{k} \tag{3.3}$$

The absolute radial frequency is given by

$$\omega=\sigma+\vec{k}\cdot\vec{u} \tag{3.4}$$

And the intrinsic frequency is obtained from the linear dispersion relation

$$\sigma=\sqrt{gk\tanh kh} \tag{3.5}$$

3.2.2.2 Wave Breaking and Dissipation

The wave energy dissipation due to wave breaking is modelled according to *Roelvink* [1993] using the default command break = 3 as

$$D_{waves} = 2\alpha f_{rep} E_{waves} Q_{break} \tag{3.6}$$

with $\alpha = O(1)$ and f_{rep} is a representative intrinsic frequency and where

$$E_{waves} = \frac{1}{8}\rho g H_{rms}^2 = \int E_{waves}(x,y,\theta)d\theta \tag{3.7}$$

and where H_{rms} is the root mean squared wave height. The fraction of breaking waves is given by

$$Q_{break} = \min\left[1 - \exp\left(-\left(\frac{H_{rms}}{\gamma h}\right)^n\right),\ 1\right] \tag{3.8}$$

A new command, break = 4, was developed by *Roelvink* [Pers. Com. 2009] to better simulate the breaking process. With this command, breaking is switched on or off according to

$$\begin{aligned} &H_{rms} > \gamma h \Rightarrow Q_{break} = 1 \\ &H_{rms} < \gamma_2 h \Rightarrow Q_{break} = 0 \end{aligned} \tag{3.9}$$

where h is the local water depth. Therefore breaking occurs only when the model senses that H/h is between the range gamma and gamma2 and thus a partial probabilistic approach is not used to estimate wave breaking. The property that waves are breaking is transported with the wave groups as

$$\frac{\partial Q_{break}}{\partial t} + \frac{\partial Q_{break} C_{gx,mean}}{\partial x} + \frac{\partial Q_{break} C_{gy,mean}}{\partial y} = 0 \tag{3.10}$$

and during this time, the wave dissipation is given as

$$D_{waves} = \frac{\alpha}{4}\rho g f_{rep} \frac{H_{rms}^3}{h} Q_{break} \tag{3.11}$$

which, in effect, is similar to the formulation of *Battjes* and *Janssen* [1978]. The total wave dissipation, $\bar{D}$, is then distributed proportionally over the wave directions.

$$D(x,y,\theta) = \frac{S_{waves}(x,y,\theta)}{E_{waves}(x,y)}\bar{D} \tag{3.12}$$

Given the spatial distribution of the wave action, and therefore the wave energy, the wave forcing can be calculated utilizing the radiation stress tensor

$$F_x = -\left(\frac{\partial S_{xx}}{\partial x} + \frac{\partial S_{xy}}{\partial y}\right) \tag{3.13}$$

$$\text{and} \quad S_{xx} = \int\left(\frac{c_g}{c}\left(1+\cos^2\theta\right) - \frac{1}{2}\right) S_{waves} d\theta \tag{3.14}$$

3.2.2.3 Roller Energy Equation Solver

Similar to the solution of the wave action equations an up-wind schematisation is used to solve the roller energy balance. The roller energy balance is coupled to the wave action balance where the dissipation of wave energy in (3.1) serves as a source term for the roller energy balance. The roller energy frequency spectrum is represented by a single representative frequency. The roller energy balance is then given by

$$\frac{\partial S_{roller}}{\partial t}+\frac{\partial c_x S_{roller}}{\partial x}+\frac{\partial c_y S_{roller}}{\partial y}+\frac{\partial c_\theta S_{roller}}{\partial \theta}=D_{waves}-D_{roller} \tag{3.15}$$

with S_{roller} representing the roller energy. The roller energy propagation speeds in the x-direction is given in (3.3), hence, we are assume that the waves and rollers propagate in the same direction. The phase velocity is obtained from linear wave theory:

$$c=\frac{\sigma}{k} \tag{3.16}$$

The roller energy dissipation is given by *Deigaard* [1993] as

$$\bar{D}_{roller}=c\tau_{roller} \tag{3.17}$$

where τ_{roller} represents the shear stress induced by the roller at the surface, which is expressed by *Svendsen* [1984] as

$$\tau_{roller}=\frac{\rho g R}{L}\beta_r \tag{3.18}$$

where R represents the roller area, L the roller length and β_r is the slope of the breaking wave (typically between 0.05 and 0.10). The roller area is related to the roller energy trough by

$$E_r=\frac{1}{2}\frac{\rho R c^2}{L} \tag{3.19}$$

Next the total wave dissipation, $\bar{D}_{roller}$, is distributed proportionally over the wave directions:

$$D_{roller}(x,y,\theta)=\frac{S_{roller}(x,y,\theta)}{E_{roller}(x,y)}\bar{D}_{roller} \tag{3.20}$$

Similarly, the source term is obtained from the wave action balance given by (3.12). The roller also affects the wave forcing and has therefore to be included in the radiation stress terms:

$$S_{xx,roller}=\int \cos^2\theta S_{roller}d\theta \tag{3.21}$$

These roller radiation stress contributions are added to the wave-induced radiation stresses in order to obtain the total radiation stress gradients.

3.2.2.4 Shallow water equations solver

The depth-averaged and short wave-averaged shallow water equations read:

$$\frac{\partial u}{\partial t}+u\frac{\partial u}{\partial x}+v\frac{\partial u}{\partial y}-fv-\nu_h\left(\frac{\partial^2 u}{\partial x^2}+\frac{\partial^2 u}{\partial y^2}\right)=\frac{\tau_{sx}}{\rho h}-\frac{\tau_{bx}}{\rho h}-g\frac{\partial \eta}{\partial x}+\frac{F_x}{\rho h} \tag{3.22}$$

$$\frac{\partial v}{\partial t}+u\frac{\partial v}{\partial x}+v\frac{\partial v}{\partial y}+f\,u-\nu_h\left(\frac{\partial^2 v}{\partial x^2}+\frac{\partial^2 v}{\partial y^2}\right)=+\frac{\tau_{sy}}{\rho h}-\frac{\tau_{by}}{\rho h}-g\frac{\partial \eta}{\partial y}+\frac{F_y}{\rho h} \tag{3.23}$$

$$\frac{\partial \eta}{\partial t}+\frac{\partial hu}{\partial x}+\frac{\partial hv}{\partial y}=0 \tag{3.24}$$

Here, h is the water depth, u, v are Lagrangian velocities in x- and y-direction, $\tau_{bx,}\tau_{by,}$ are the bed shear stresses, $\tau_{sx,}\tau_{sy,}$ are the wind stresses g is the acceleration of gravity, η is the water level and F_x, F_y are the wave-induced stresses. The water level gradients and shear stresses are computed at the cell interfaces. For computing the shear stresses at the cell interfaces we need the velocity magnitudes at these interfaces. These are composed by combining the normal velocity component at the interface and the average of the four adjacent tangential components. For the depth at cell interfaces, following *Stelling* and *Duinmeijer* [2003] XBeach distinguishes between the depth used in the continuity equation and that used in the momentum equation.

The depth at the interfaces for the continuity equation is taken as the upwind depth, in case the velocity is greater than a minimum velocity; or as the maximum water level minus the maximum bed level in case the velocity is less than this minimum velocity. For the depth in the momentum balance we take the average depth between the cell centres. The velocities at the new time step level are computed from the advection terms in x- and y-direction and the momentum equation. The water level is subsequently updated.

3.2.2.5 Generalized Lagrangian Mean Formulation

To account for the wave induced mass-flux and the subsequent (return) flow, the shallow water equations are cast into a Generalized Lagrangian Mean (GLM) formulation [*Walstra et al.* (2000); *Andrews* and *McIntyre*, (1978)]. To that end, the Eulerian shallow water velocity u_E is replaced with its lagrangian equivalent u_L,

$$u^L=u^E+u^S \quad \text{and} \quad v^L=v^E+v^S \tag{3.25}$$

and u^S , v^S represents the Stokes drift in x- and y-direction respectively [*Phillips* (1977)]

$$u^S=\frac{E_w\cos\theta}{\rho hc} \quad and \quad v^S=\frac{E_w\sin\theta}{\rho hc} \tag{3.26}$$

where the wave-group varying short wave energy and direction are obtained from the wave-action balance. The resulting GLM-momentum equations are given by:

$$\begin{aligned}\frac{\partial u^L}{\partial t}+u^L\frac{\partial u^L}{\partial x}+v^L\frac{\partial u^L}{\partial y}&=-\frac{\tau_{bx}^E}{\rho h}-g\frac{\partial \eta}{\partial x}+\frac{F_x}{\rho h}\\ \frac{\partial v^L}{\partial t}+u^L\frac{\partial v^L}{\partial x}+v^L\frac{\partial v^L}{\partial y}&=-\frac{\tau_{by}^E}{\rho h}-g\frac{\partial \eta}{\partial y}+\frac{F_y}{\rho h}\end{aligned} \tag{3.27}$$

for the x- and y-direction respectively. This operation shows that the GLM equations for the depth-averaged flow are very similar to the previously described Eulerian formulation, with the exception of the bottom shear stress terms that are calculated with the Eulerian velocities as experienced by the bed:

$$u^E=u^L-u^S \quad \text{and} \quad v^E=v^L-v^S \tag{3.28}$$

and not with the GLM velocities. Also, the boundary condition for the flow computations has to be expressed in functions of (u^L, v^L) and not (u^E, v^E).

3.3 Previous Validation Studies

For numerical models like XBeach, it is important to validate against data which accurately represents nature. Successful validation will therefore prove to a certain extent that the model is capable of representing nature and can therefore fulfil its aim to be used as a tool to investigate real-life morphodynamic problems. A number of validation test cases have already been carried out, both in 1D and in 2DH mode. Here we will describe a series of tests that together give an impression of the capabilities and performance of XBeach and will show why further validation is required. The validation studies are done against laboratory results, theoretical or analytical derivations or from prototype field experiments which capture data from nature itself.

Of course, extreme caution and care has to go into the measuring techniques used to collect raw data to ensure that it is of sufficiently high quality to be used for validation purposes. The severity of conditions during a storm therefore makes it quite difficult to obtain accurate measurements, and therefore not many quality datasets exist from which validation studies of morphological change associated to storms can be done.

3.3.1 Analytical Validation Studies

Analytical validations show the capability of the model to reproduce expected results for from a theoretical and numerical perspective. XBeach has already been tested for a number of these cases. LF wave propagation and numerical damping has been checked by doing a reflection test in which a standing wave is created. The wave run-up results were compared to the well known analytical solution by *Carrier* and *Greenspan* [1958] and the results showed excellent agreement. The seaward and lateral boundary conditions were also checked, especially concerning diffraction effects for generated edge waves and the development of longshore currents. Here, the results showed that the short wave energy propagates in and out of the model without any noticeable disturbances.

Further to these two tests, *McCall* [2008] carried out a full series of analytical tests where the wave forcing and surge/tide levels were varied for longshore uniform and non-uniform bathymetries. This was done using stationary, bichromatic and irregular waves. *McCall* showed that the short wave propagation scheme works very well and that shoaling and refraction over a longshore uniform bathymetry matches analytical results from linear wave theory. The propagation and reflection of LF waves was shown to be realistic, however, in some cases the energy content was found at very low frequencies and not within the expected frequency range.

3.3.2 Laboratory Validation Studies

Laboratory validation studies test the model against measured data for waves, currents and sediment transport. The near-ideal conditions of laboratory experiments make the dataset good for comparisons with XBeach simulations. Most of the laboratory validation tests for XBeach have been done with data obtained from experiments carried in the Delta flume, located in the Netherlands, which investigates hydrodynamics and morphology.

All of the laboratory validation results show that the short wave propagation and decay are represented quite well, both in terms of the surface elevation and velocities. The avalanching algorithm is tested for its ability to simulate the dune erosion process. A relatively simple approach, whereby an underwater critical slope of 0.3 and a critical slope above water of 1.0 were applied, proved to be quite successful in representing the retreat of the upper beach and dune face [*van Thiel de Vries* (2007)].

Other flume tests [*Delta Flume* (2005)] have confirmed the model's capability to simulate typical offshore-directed dune erosion processes for relatively high dunes, with the final measured and final computed profiles showing excellent agreement.

3.3.3 Field Validation Studies

Jimenez et al. [2006] analyzed and classified the response of sandy dunes inhabiting Assateague Island from extreme storm impact depending on the initial state of the dune. Following this work XBeach was tested to check whether it provides a qualitatively similar response. Preliminary conclusions indicated that for seaward dune erosion and for massive overwashing cases XBeach has a realistic behaviour, however intermediate cases of intermittent overwashing needs further work.

McCall [2008] investigated the real-life case of overwashing of Santa Rosa Island located on the Gulf coast of the United States. In this case XBeach was able to produce the complex structures associated with such events, such as washover throats and fans, which proved that it is qualitatively correct in modelling these morphological features. The amount of morphological change predicted by XBeach was, however, too great by as much as an order of magnitude.

3.3.4 Summary

The validation studies done so far have sought to prove the functionality of various parts of the XBeach code. In terms of the hydrodynamics, the short wave propagation scheme, flow boundary conditions and also basic the run-up and reflection of LF waves have been shown to function very well. The main shortfall lies in the representation of LF waves in terms of energy content for irregular wave input. In terms of morphology, the model represents natural processes such as avalanching, offshore transport of sediment and dune erosion to a good extent. However, the more advanced forms of morphology, such as overwash and breaching which occurs in very shallow water or on partially wet land, the morphological rate of change is too high in most cases.

Chapter 4 – Hydrodynamic Validation Procedure

In this chapter, the procedures of the hydrodynamic validation are outlined. First, the objectives of the validation study are given in Section 4.1. In Section 4.2, the experiment of *van Noorloos* [2003][2] is described in some detail. Section 4.3 focuses on the model setup of XBeach and a preliminary sensitivity analysis to determine the main variables for the modelling exercise. Section 4.4 presents a brief outline of the procedures used to obtain parameters for comparison in Chapters 5 and 6.

4.1 Validation Objectives and Approach

4.1.1 Objectives

The hydrodynamic validation involves using the VN dataset as a reference to represent water surface elevations and current velocities at a high spatial resolution. The main objective is to validate the XBeach model results of the incoming bound and reflected free LF waves (IBLF and RFLF waves respectively). In order to do so, we must first look at the processes which control the forcing and shoaling of the incoming LF wave, viz. the shoaling, breaking and dissipation processes of the short waves, which all have to be modelled well in XBeach. Output parameters from the XBeach simulations of the VN experiment will, therefore, be compared to the actual measurements to ensure that the model is capable of reproducing the following results:

- The shoaling and breaking process of the short wave groups represented through spatial variations in H_{rms}, E and S_{xx}.
- The amplitude and phase variation of IBLF and RFLF waves.
- The energy transfer, R, from the short wave groups to the (shoaling) IBLF wave and its subsequent release and reflection as a RFLF (de-shoaling) wave.
- The magnitude and direction of the depth averaged LF velocity.

4.1.2 Approach

Figure 4.1 shows the hydrodynamic processes which will be investigated in the coming sections, most of which fall under the classification of HF the waves. Though the objectives of the validation process are aimed at obtaining good LF wave estimations from XBeach, invariably, we have to focus on the HF wave parameters in some detail since the LF waves grow during the shoaling process of HF waves and are released during the breaking process.

[2] Hereinafter, reference to this work is stated as 'VN' or 'the VN experiment' or 'the VN dataset' where applicable.

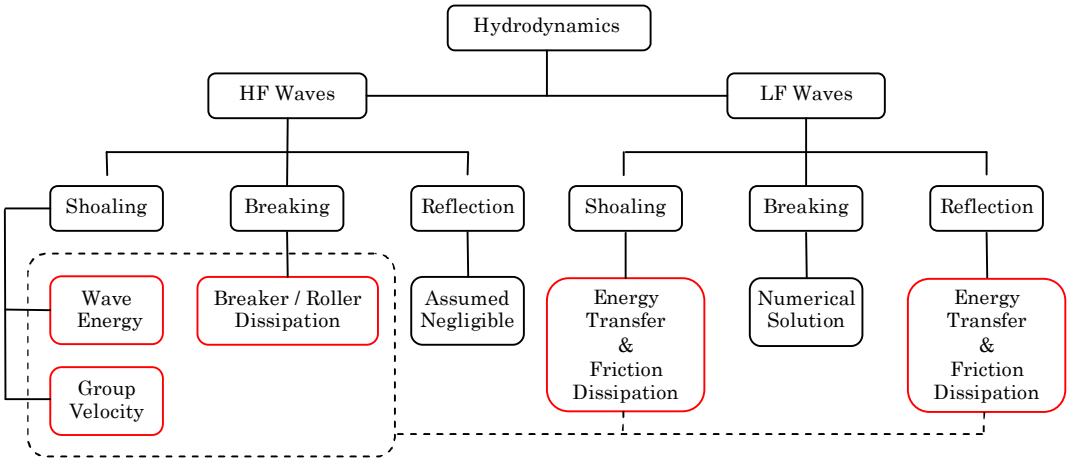

Figure 4.1: Hydrodynamic processes considered in the validation study.

The wave action numerical scheme of the XBeach model is checked by looking at the basic terms – wave energy and group velocity. The proportionality of the wave energy to the square of the wave height, according to (2.35), is very important for the XBeach computations, both in terms of energy input (forcing) and output such as radiation stress gradients. The correct representation of the group velocity will ensure that the energy flux, according to (2.36), is propagated at the correct velocity. We will therefore investigate shoaling characteristics of the HF waves by looking at the (time-averaged) RMS wave height and group velocity. The effect of energy dissipation through wave breaking will also be investigated as it also influences the wave action.

The short wave processes are computed in the short wave module of XBeach while the flow module of XBeach computes the LF surface elevation using the NSW equations. The energy transfer from HF to LF waves (and vice versa), according to (2.56), is a function of the radiation stress gradient of the HF waves and the phase difference between the HF wave envelope and the IBLF wave. This is highlighted by the dotted lines in Figure 4.1 and is also investigated in the coming sections. Dissipation of the LF waves is not directly investigated, as the process is represented numerically by the NSW equations in XBeach, however, the effect of the Chezy friction coefficient may play an important role. The RFLF waves will be also investigated in a similar manner as the IBLF waves.

Finally, we will investigate the accuracy of two numerical approaches used to simulate the breaking process of the HF waves. These different breaking schemes in XBeach, which are discussed further in subsection 4.3.3, use the keywords break = 3 and break = 4.

4.2 The Van Noorloos Experiment and Dataset

4.2.1 Physical Setup

Van Noorloos (VN) conducted experiments in the wave flume of the Fluid Mechanics Laboratory at Delft University of Technology. The flume is 40 m long from the mid-position of the stroke of the wave generator (henceforth referenced as the origin $x = 0$ m) to the opposite wall. The depth of the flume is 1.05 m with a water level of 0.7 m maintained for two test cases.

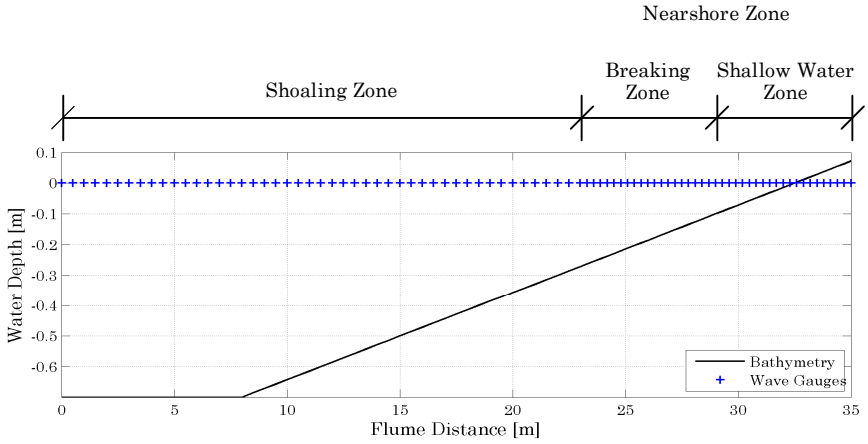

Figure 4.2: Bathymetry and location of wave gauges in the flume experiment of van Noorloos.

VN defined a 'case' based on the type of bathymetry employed; first a *horizontal case* in which the depth is uniform throughout the entire flume, and second, a *sloping case* for which the steepness of the bottom is 1:35 starting at $x = 8.5$. The bottom surface level is fixed using smoothed concrete. The bathymetry of the sloping case is shown in Figure 4.2.The wave generator is a piston type wave bard capable of Active Reflection Compensation (ARC), which absorbs reflected (long) waves. The board is also capable of generating second-order waves while suppressing the generation of spurious free super- and sub-harmonics.

We will only be using the data from the sloping cases in the validation study as they contain the required information of LF wave shoaling and reflection, and as such, we will redefine '*case*' to represent the individual sloping experiments.

4.2.2 Data Acquisition

4.2.2.1 Surface Elevation

In the horizontal case, the wave gauges are positioned in order to optimize the decomposition of the wave signal data into incoming and outgoing components. For the sloping case, the first wave gauge is located at $x = 6$ m and subsequent gauges are spaced 0.5 m apart up to $x = 23$ m (0.2714 m water depth), thereafter the spacing is reduced to 0.3 m in order to obtain a high spatial resolution of the (short) wave breaking process and energy transfer in shallow water. In total, there are 80 locations with wave signal data over a distance of 30.5 m (from $x = 6$ to $x = 36.5$ m). The sampling frequency of the wave measuring instruments, f_s, is 25 Hz. This corresponds to a Nyquist frequency, f_{nyq}, of 12.5 Hz (where $f_{nyq} = f_s/2$). The location of the wave gauges are shown in Figure 4.2.

For convenience, we can define a number of *zones* within the flume, as shown in Figure 4.2. The *shoaling zone* is taken as all the points from the origin up to 23 m where the wave gauge spacing is 0.5 m. The *nearshore zone*[3] is defined as the (remaining) section of the flume where the wave

[3] The term 'nearshore zone' may also be replaced by 'surf zone' such that it infers inclusion of the area of wave run-up, however in this report we assume that the 'shallow water zone' also represents this area.

gauge spacing is 0.3 m. The nearshore zone is divided equally into the *breaking zone* (taken from 23 m up to 29 m) and the *shallow water zone* (taken from 29 m up to 35 m).

4.2.2.2 Current Velocities

An electromagnetic flow meter (EMS) was used to measure current velocities at four point locations in the experiment. The placement of the EMS was strategically done by placing the EMS at the same cross-shore location as one the wave gauges in order to obtain simultaneous and synchronous recordings of surface elevation and velocities. The use of the EMS was limited to water depths greater than 5 cm as this is the minimum depth required for proper output. The sampling frequency of the EMS is also 25 Hz as for the wave gauges.

4.2.3 Wave Cases

4.2.3.1 Bichromatic Wave Cases

The bichromatic wave cases consist of two series sets. In the first series set (series A), the group frequency of the two primary wave components (with individual frequencies f_1 and f_2) and thus the bound wave frequency, f_b (where $f_b = f_1 - f_2$), is varied. The mean frequency of the primary waves, f_m (where $f_m = (f_1 + f_2)/2$), is kept constant. In the second series set (series B) variations in the primary amplitudes (a_1, a_2), and thus the modulation, δ, of the primary wave components are taken into account while still maintaining a constant mean frequency. Details of the primary wave components are given in Table 1. The values of the amplitudes (and modulations) shown are those which were obtained from the measured data rather than the target values.

4.2.3.2 Irregular Wave Cases

The irregular wave cases are defined using a parameterized JONSWAP spectrum, given in (2.48) , which is represented by a (spectral) significant wave height, H_{m0}, and peak frequency, f_p. There are two series sets of irregular waves. In the first series set (series C) the significant wave height is varied and the peak frequency is kept constant. For the second series set (series D), the significant wave height is again varied while the peak frequency is constant, but of greater value than in the first series set. Details of the irregular wave cases are given in Table 2 below.

Table 1 Wave Parameters for Bichromatic Wave Cases

Series	a_1 [m]	a_2 [m]	δ [-]	f_1 [Hz]	f_2 [Hz]	f_b [Hz]	f_m [Hz]
A-1	0.0625	0.008	0.128	0.6714	0.4761	0.1953	0.5737
A-2	0.0609	0.008	0.131	0.6470	0.5005	0.1465	0.5737
A-3	0.0606	0.008	0.132	0.6348	0.5127	0.1221	0.5737
A-4	0.0601	0.009	0.149	0.6226	0.5249	0.0977	0.5737
B-2	0.0611	0.012	0.196	0.6470	0.5005	0.1465	0.5737
B-3	0.0610	0.016	0.262	0.6470	0.5005	0.1465	0.5737
B-4	0.0608	0.020	0.329	0.6470	0.5005	0.1465	0.5737
B-5	0.0603	0.024	0.398	0.6470	0.5005	0.1465	0.5737

Table 2 Wave Parameters for Irregular Wave Cases

Series	f_p [Hz]	T_p [s]	H_{m0} [m]
C-1	0.50	2.00	0.05
C-2	0.50	2.00	0.075
C-3	0.50	2.00	0.1
D-1	0.65	1.54	0.05
D-2	0.65	1.54	0.075
D-3	0.65	1.54	0.1

4.2.3.3 Timeseries Duration

The duration of the timeseries is dependent on the number of data points used in the fast Fourier Transform (FFT) of the signal, which is optimized if the value is an integer power of 2. Therefore, the duration is given as

$$D = \frac{2^p}{f_s}. \tag{4.1}$$

In order to decrease computational time for FFT procedures (see Appendix A), f_s is reduced to 6.25 Hz. For bichromatic cases, $p = 11$, therefore a duration $D = 327.68$ s (5.46 minutes) is used from the measured timeseries. For the irregular wave cases, $p = 15$, and therefore $D = 1310.72$ s (21.84 minutes). A longer timeseries is required for the irregular wave cases in order to obtain accurate energy variance density spectra without compromising the spectral resolution (see Appendix A). In order to eliminate the start-up effects of the experiment, the first 200 s of the bichromatic timeseries is discarded, while for the irregular wave cases, the first 10 minutes of data is discarded. After this time a certain equilibrium is established.

4.3 XBeach Model Setup

4.3.1 Model Grid and Flow Boundary Conditions

A non-uniform grid is used in the XBeach model in order to represent the bathymetry of the wave flume used in the VN experiment. The grid has 3 lines of nodes in the computational y-axis with a spacing of 0.4 m and 104 nodes in the x-axis with an initial spacing of 0.5 m up to $x = 23$ m and 0.3 m thereafter until $x = 40.1$ m. Each node in the x-axis (between $x = 6.0$ m and $x = 36.5$ m) corresponds to the location of a wave gauge in the experimental setup of VN, thereby enabling us to compare results at the same spatial output locations. Only the output from the central (second) node in the y-axis is used for comparison.

XBeach uses an input file (params.txt) in which model parameters are specified. The parameters representing the flow boundary conditions enable the sides of the grid to be modelled as walls which retain flow within the model. A wall is also imposed on the shoreward boundary of the model but allowance is made for wave run-up. At the wave input boundary, ARC (ARC) is enabled to prevent re-reflection of outgoing waves in the model. The mean wave direction (dir0) is set to

represent the unidirectional propagation of the short wave fronts into the model and toward to the beach such that there is no directional spreading. Wave-current interaction is not included in the computations, however, the roller energy dissipation model is turned on.

4.3.2 Input Variables

A number of standard input parameters used in XBeach are defined in Table 3 below. A number of these parameters in Table 3 have variable values which all have to be 'tuned' to obtain the good model results. These parameters are Hrms, Trep, eps, C, alpha, gamma and gamma2. The values of Hrms and Trep depend on the type of wave energy input, whether bichromatic or irregular (discussed further in the subsection 4.3.4).

The eps is a numerical parameter which denotes the threshold depth for drying and flooding; therefore it separates wet grid cells from dry ones. The eps parameter can be interpreted in physical terms as the minimum water depth for the XBeach calculations. The Chezy friction coefficient parameter, C, varies the bed roughness of the model. The parameters alpha, gamma and gamma2 are all related to wave breaking and dissipation.

Table 3 General XBeach Input Parameters

Parameter	Definition	Value	Units
nx	Number of grid cells in x-direction	103	-
ny	Number of grid cells in y-direction	2	-
rho	Density of water	1000	kg/m^3
g	Gravitational acceleration	9.81	m/s^2
thetamin	Lower directional limit	-90	degrees
thetamax	Upper directional limit	90	degrees
dtheta	Directional resolution	180	degrees
dir0	Direction of wave propagation	270	degrees
CFL	Courant number	0.5	-
scheme	Wave action balance numerical scheme	2	-
eps	Threshold water depth	variable	m
C	Chezy friction coefficient	variable	$m^{0.5}s^{-1}$
Hrms	RMS short wave height	variable	m
Trep	Representative short wave period	variable	s
n	Power in Roelvink dissipation	12	-
alpha	Wave dissipation coefficient	variable	-
beta	Breaker slope coefficient	0.1	-
gamma	Breaker parameter	variable	-
gamma2	Lower breaker parameter (break =4)	variable	-
gammax	Maximum ratio of H/h	5	-

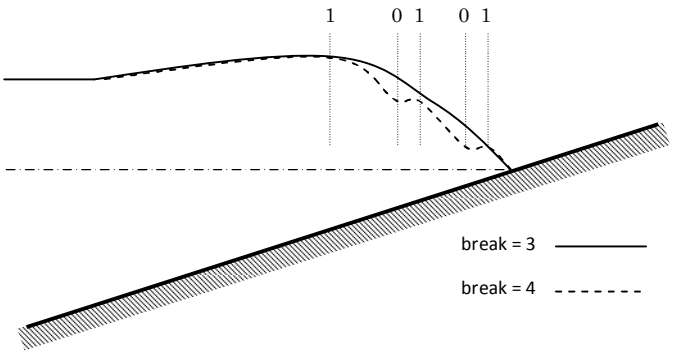

Figure 4.3: Schematic representation of the difference in the wave breaking pattern between the break = 3 (solid line) and break = 4 (dashed line) commands. For break = 4, the ones represent breaking 'on' and the zeroes represent breaking 'off'.

4.3.3 Wave Breaking and Dissipation

XBeach has different options to represent wave breaking. With the command break = 3, XBeach uses a modified formulation of *Roelvink* [1993] in which breaking occurs where H/h is over the threshold value of the breaker parameter, gamma (described in Section 3.2.2.2). A new command developed by *Roelvink* [Pers. Com. 2009], break = 4, turns breaking on when H/h is within the range of gamma and gamma2 (a new parameter) and off otherwise. This new breaker formulation is tested and compared to the default break = 3 command in the results given in Chapters 5 and 6.

The parameter gamma is used in both breaking options and gamma2 is used only in the break = 4 option. Another parameter gammax, is used to set a limit on H/h, however, is left at its default value as we will already vary gamma and gamma2. Another important parameter is the dissipation coefficient, alpha, which influences the steepness of the decay of HF wave height during the breaking process. In Chapters 5 and 6, alpha, gamma and gamma2 are optimised to best fit the results of the VN experiment.

The essential difference between the two breaker formulations is that with break = 3, the probability of breaking function applied to the shoaling waves allows dissipation to start earlier than with break = 4, where breaking *only* occurs once the breaker parameter has exceeded the threshold gamma. With break = 3, the wave height decreases rather linearly beyond the initial breakpoint with little variation. With break = 4, there is the possibility to have multiple abrupt breakpoints by specifying an upper and lower limit of the breaker parameter which permits greater variation in the breaking wave heights.

In essence, break = 3 is analogous to the time-varying breakpoint model of LF wave generation of *Symonds et al.* [1982] in which the groupiness of the waves is reduced during breaking, while break = 4 is more comparable to the hybrid model of LF wave generation of *Schäffer* [1993] where groupiness is permitted within the breaking and shallow water zone.

4.3.4 Wave Energy Input

4.3.4.1 Bichromatic Wave Cases

For bichromatic waves, the XBeach model is forced by an input timeseries of the incoming wave energy and water level at the model boundary (keyword: instat = 3). These timeseries are not

computed by XBeach, but are created in a separate file which is saved in a format that can be read by the model. The wave energy timeseries is computed using (2.35), where H is the group-varying RMS wave height of bichromatic waves obtained from the envelope detection method discussed in Appendix 2. The water levels are computed from (2.49). The input timeseries is calculated using a timestep (dtbc) of 0.04 s, the same as the 25 Hz frequency resolution of the wave gauges in the VN experiment.

In addition to the input energy and water level timeseries, the parameters Hrms and Trep have to be specified in the params.txt input file. The value of Hrms is obtained from the measured data of the VN experiment, and is used to scale the input energy timeseries to the level of the measured data. Individual short waves themselves are not modelled by XBeach, however, their representative period, Trep, has to be specified as it is used by the model to compute the group velocity. The process to determine the correct value of Trep to be used is explained in Chapter 5.

4.3.4.2 Irregular Wave Cases

XBeach is capable of generating an energy timeseries from a JONSWAP energy density spectrum using defined spectral parameters (keyword: instat = 4). For the irregular wave cases, the parameters used by VN in his experiments (given in Table 2) are also used in XBeach. There are additional parameters used to define the spectrum, namely the peak enhancement factor (gammajsp), directional spreading coefficient (s), main (nautical) wave angle (mainang) and the Nyquist frequency (fnyq). These are specified with values of 3.3, 10000, 270 and 12.5 respectively. These settings ensure that the spectral peak is enhanced to a match the JONSWAP shape, there is (essentially) no directional spreading and the waves propagate toward the shoreline.

The representative period used in XBeach is normally computed using the average of the frequencies within a range above and below the peak frequency, T_p, which contributes to 80% of the total energy density. An additional parameter, Trepfac, can be used to limit this range. While the default value is 0.8, a value of 1 for this parameter will result in T_{rep} being equal to T_p while a value of 0 will result in an average period, T_{m01}, period taken over the entire spectral range up to the upper limit given by fnyq.

4.3.5 Model Output

The output requested from XBeach are the:

- bottom elevation (zb),
- timeseries of the still water (LF) surface elevation (zs),
- timeseries of the RMS short wave height (H),
- depth averaged horizontal (cross-shore) LF particle velocity (u),
- short wave group velocity (cg),
- wave energy (E) and
- radiation stress (Sx).

The bottom is fixed in XBeach, therefore zb is constant for all computational outputs.

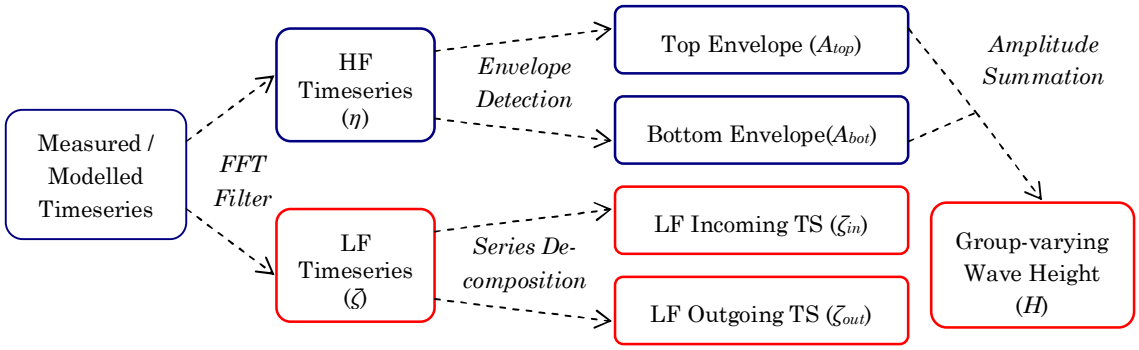

Figure 4.4: Process chart for separating different types of wave data from a measured surface elevation timeseries. Blue boxes indicate applicability to the van Noorloos data and red boxes indicate applicability to both the XBeach output and the van Noorloos data.

4.4 Timeseries Separation Techniques

A measured surface elevation timeseries, such as the raw data from the VN experiment, contains many types of waves which need to be separated from each other for analysis. These mainly include the short waves, IBLF and RFLF waves. We can obtain the time-averaged properties of these waves and further determine cross-shore variations when we consider the data from the collective series of wave gauges (w.r.t the VN data) and output nodes (w.r.t the XBeach data). We therefore have to employ different methods to extract the required data needed for our comparisons between the XBeach output and VN measured data.

Three main methods are used to extract this information from within the measured timeseries of VN and the XBeach output. These are fast Fourier Transform (FFT) filtering, envelope detection and timeseries decomposition, as shown in Figure 4.4. The FFT filtering is used to divide a (measured) timeseries into two main parts; a HF component and a LF component. This is done using the discrete Fourier Transform (DFT), where a cut-off frequency, f_{cut}, is used to distinguish between the HF and LF frequency ranges. The value of f_{cut} used for the bichromatic wave cases is equal to twice the difference frequency, f_b., while for the irregular waves cases, a value of 0.3 Hz is used for the series C and 0.4 Hz for series D. The FFT filtering procedure is explained in more detail in Appendix A.

Envelope detection is used to obtain the upper and lower amplitude envelope of a timeseries signal. The summation of these envelope timeseries gives the group-varying wave height, which can be used as a measure of the instantaneous root-mean-square (RMS) wave height, H. The phase information of H can also be used to compute the group velocity of the short waves. This procedure is explained in detail in Appendix B.

LF decomposition is used to separate IBLF and RFLF waves from the total LF (or surface elevation) timeseries. Here it is assumed that ARC does not permit the re-reflection of LF waves at the wavemaker, therefore incoming free LF (IFLF) waves do not exist and that the HF wave energy is completely dissipated during wave breaking and therefore they do not reflect, therefore timeseries decomposition is only applicable to LF data. This is discussed in more detail in Appendix C.

FFT filtering and envelope detection is applied to the VN measured data while LF decomposition is applied to both the XBeach output and the VN measured data.

Chapter 5 – Bichromatic Wave Case Results

In this chapter the model output from XBeach for the simulation of the bichromatic wave cases of VN are compared to the measured data obtained from the flume experiment. The new breaker model formulation of *Roelvink* [Pers. Com. 2009] is tested to determine its effect on HF and LF hydrodynamics. The relevant input parameters are discussed first in Section 5.1 followed by the results of the short wave shoaling and dissipation in Section 5.2. and the results of the decomposed LF waves in Section 5.3. In subsection 5.3.4, the relationship between the HF and LF waves are presented by looking at the energy transfer between both. Finally, a summary of the validation results is presented in Section 5.4.

5.1 Optimizing Input Variables

5.1.1 Calibrated Model Parameters

In subsection 4.3.2 we identified a number of parameters used in the general XBeach input file. Seven of these parameters are found to be important variables for the bichromatic wave cases. These are Hrms, Trep, gamma, gamma2 (for break = 4), alpha, eps and C. The first five parameters have been calibrated to optimize the results of XBeach. Hrms is related to the input energy time series used in XBeach (discussed in subsection 5.1.2). Trep and gamma have been determined by trial and error using the autocorrelation function (discussed in subsection 5.1.3). gamma2 is used only for the break = 4 breaker parameterization. Both alpha and gamma2 have been varied to best represent the steepness and endpoint of breaking respectively.

The remaining two parameters, eps and C, are found to mainly affect the LF wave results (discussed in section 5.3). For these parameters, a test was done to see the effect of varying them from the 'base case'. The base case values are values found to give reasonable results, but are varied in order to determine the sensitivity of the LF results. The value of eps was increased from 0.001 m (the lowest value which was found to affect the LF results) to 0.005 m. For C, a value of 70 is initially used, which represents a smooth concrete surface. This was varied to a value of 50, which is somewhat rougher.

Table 4 following shows the calibrated input values used in the bichromatic validation process. The value of Trep is constant for all test cases as the mean frequency of the bichromatic experiments are kept constant (see Table 1). The value of gamma is constant for all break = 4 model runs (a value of 0.75), however, it has to be varied when using break = 3. The value of alpha is close to the recommended value of 1.1 [XBeach manual] for break = 3, but it has to be increased to 2.5 for the break = 4 runs. A test is also done to determine the effect of the grid resolution on the LF results. In this test, the original grid defined in subsection 4.3.1 (referred to as '*grid 1*') is doubled in resolution in the *x*-direction, to have a total of 207 nodes (*grid 2*). The base case values of eps and C are used for these model runs in addition to the other calibrated model parameters excepting Trep, for which a value of 1.743 s is used (explained in subsection 5.1.3.2).

Table 4 Variable Input Parameters for XBeach Bichromatic Wave Cases

Series	Hrms [m]	Trep [s]	gamma [-] (break = 3 / 4)	gamma2 [-] (break = 4)	alpha [-] (break = 3 / 4)	eps [m] (base / test)	C [$m^{0.5}s^{-1}$] (base / test)
A-1	0.1273	1.801	0.75 / 0.75	0.15	1.2 / 2.5	0.001 / 0.005	70 / 50
A-2	0.1268	1.801	0.75 / 0.75	0.15	1.2 / 2.5	0.001 / 0.005	70 / 50
A-3	0.1273	1.801	0.75 / 0.75	0.15	1.2 / 2.5	0.001 / 0.005	70 / 50
A-4	0.1265	1.801	0.75 / 0.75	0.15	1.2 / 2.5	0.001 / 0.005	70 / 50
B-2	0.1304	1.801	0.69 / 0.75	0.15	1.2 / 2.5	0.001 / 0.005	70 / 50
B-3	0.1338	1.801	0.63 / 0.75	0.15	1.2 / 2.5	0.001 / 0.005	70 / 50
B-4	0.1394	1.801	0.58 / 0.75	0.15	1.2 / 2.5	0.001 / 0.005	70 / 50
B-5	0.1438	1.801	0.53 / 0.75	0.15	1.2 / 2.5	0.001 / 0.005	70 / 50

5.1.2 Input Wave Timeseries

The input energy timeseries, E, used in XBeach is computed by first creating a synthetic bichromatic timeseries using the measured amplitudes and frequencies of the primary waves in the VN experiment (given in Table 1). From this, the group-varying wave height, H, timeseries is determined using the envelope detection method outlined in Appendix B. The energy is then computed according to (2.35).

It is found that second-order waves are generated by the wave maker in the experiment of VN. Typically a linear bichromatic timeseries is used to obtain H (and thus E), however the use of a second-order bichromatic timeseries is investigated to determine if it is more advantageous. It is shown in Figure 5.1 that second-order waves have a similar energy content attributed to it when compared to linear waves, even for varying modulation of the wave group. This is also the case for the IBLF waves, computed according to (2.49). When used in XBeach model runs, the difference in the model output is negligible. Despite this, a second-order bichromatic timeseries is used to compute the energy input to the model.

In Table 4, the Hrms used as input is used to scale the energy input timeseries in XBeach. The value is derived from the measured (time-averaged) H_{rms} values from the VN data (averaged between x = 6 m and x = 16 m). In this manner, the RMS short wave height of XBeach and VN are matched at the input boundary (the wave maker).

5.1.3 Representative Period and Breaker Parameter

5.1.3.1 Auto-correlation

H_{rms} is given as output from XBeach and is determined from the HF wave envelope for the VN data. Auto-correlations (the correlation computed using the auto-covariance function) of the timeseries of H_{rms}, on a temporal scale is given as

$$\rho_{HH} = \frac{E\left[\left(H(t)-m_H\right)\left(H(t+\tau)-m_H\right)\right]}{\sigma_H^2} \tag{5.1}$$

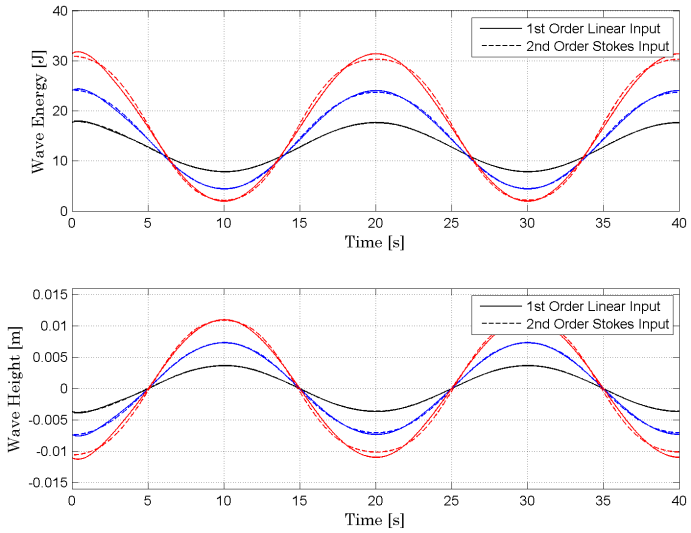

Figure 5.1: Synthetic timeseries of the group-varying input wave energy, E, (top plot) and the IBLF surface elevation, (bottom plot) obtained from bichromatic first-order (solid lines) and second-order (dashed lines) waves with modulations, $\delta = 0.2$ (black lines), $\delta = 0.4$ (blue lines) and $\delta = 0.6$ (red lines).

Where m_H is the mean value of the timeseries (assumed to be stationary), E is the expected value, σ is the standard deviation and τ is the time lag. Consider the case where we have a timeseries of $H(t)$ at a reference cross-shore location and we shift this timeseries a distance τ in time from the observed case[4], such that we get a new timeseries $H(t + \tau)$. The value of τ where we obtain the maximum correlation coefficient, τ_{max}, is equal to the time shift between the two timeseries. Therefore, the correlation at the reference point is maximum at $\tau_{max} = 0$. Repeating this process of correlating the timeseries of $H(t)$ at the reference point to $H(t + \tau)$ at different cross-shore locations reveals the spatial variations in the value of τ_{max}, and thus the group velocity assuming that $c_g = dx/d\tau_{max}$ and that the shape of the signal does not change in space or time.

Since the energy flux and thus the radiation stress computed for the short waves, as per (2.39), is dependent on c_g, it is important that XBeach is able to accurately predict its value. Using the auto-correlation method this can be checked by comparing spatial and temporal auto-correlations of $H(t)$ from XBeach to those obtained from the VN data. In Figure 5.2 the auto-correlation of H_{VN} and H_{XB} (for options `break = 3` and `break = 4`) is shown spatially and temporally. The reference point is taken at the location of the first wave gauge in the VN experiment (at $x = 6$ m) in order to facilitate direct comparison between H_{XB} and H_{VN}. In Figure 5.3, a 2D plot of the spatial variation of the auto-correlation at zero time lag ($\tau = 0$) is shown.

[4] It is important to note the difference between $t = 0$ and $\tau = 0$. For XBeach and VN data, $t = 0$ corresponds to *the start of the timeseries*, which is actually a fixed time (200 s) *after* the start of the model run or experiment. During this start-up time, data from either source is unreliable and therefore is not considered. At $\tau = 0$, the auto-correlation time lag is zero and therefore the timeseries is directly compared to itself, thus $\rho = 1$. As τ is increased or decreased, then ρ changes, varying between -1 and 1.

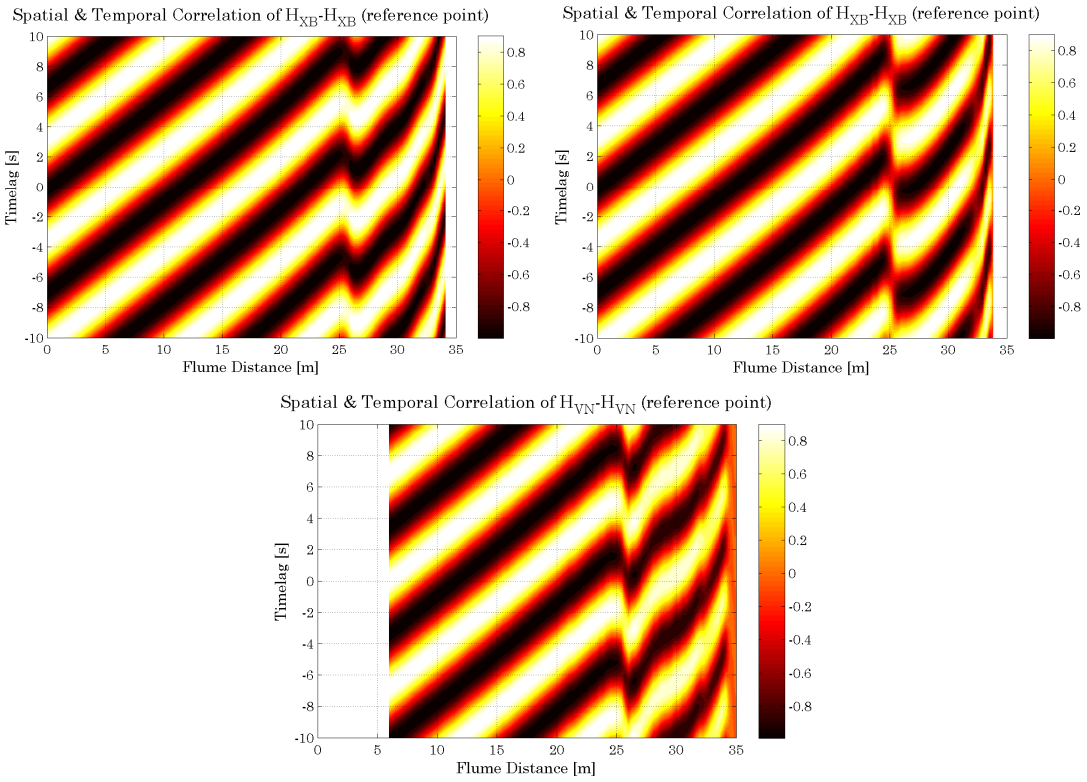

Figure 5.2: Spatial and temporal auto-correlation of H for XBeach break = 3 (top left) and break = 4 (top right) options and for van Noorloos case A-2 data (bottom).

5.1.3.2 Representative Period

Figure 5.3 shows the auto-correlation at $\tau = 0$ for four cases. In the first three, the representative period in XBeach, Trep, is equal to the peak period, T_p, (top left), the theoretical or mean period, T_m, (top right) and an optimal period, T_{opt}, (bottom left). With T_p, the auto-correlation coefficient varies at a faster rate for H_{XB} than for H_{VN} indicating that the c_g computed in XBeach is greater than the actual c_g of the short waves in the VN experiment. Using T_m, there is still slight difference, and after some trial-and-error, T_{opt} is found to be 1.801 s, rather than the theoretical value of 1.743 s (less than 4% difference).

Using this optimal value for Trep, the auto-correlation coefficients of H_{XB} and H_{VN} is very well matched, indicating that c_g determined in XBeach is similar to the actual c_g of the short waves in the VN experiment. As the mean frequency is constant for all bichromatic test cases, the optimal value of Trep (1.801 s) is used in all the model runs (with *grid 1*) with very good auto-correlation results.

The (small) difference between the values of T_{opt} and T_m may be as a result of the temporal and spatial discretizations used in the model. For instance, when using *grid 2* (a more finely resolved grid than the original) the actual value of T_m gives better correlation results than the value of T_{opt}. Using the results of the autocorrelation, we can approximately[5] calculate c_g for the VN wave

[5] This result is also sensitive to the discrete values of dx and dt.

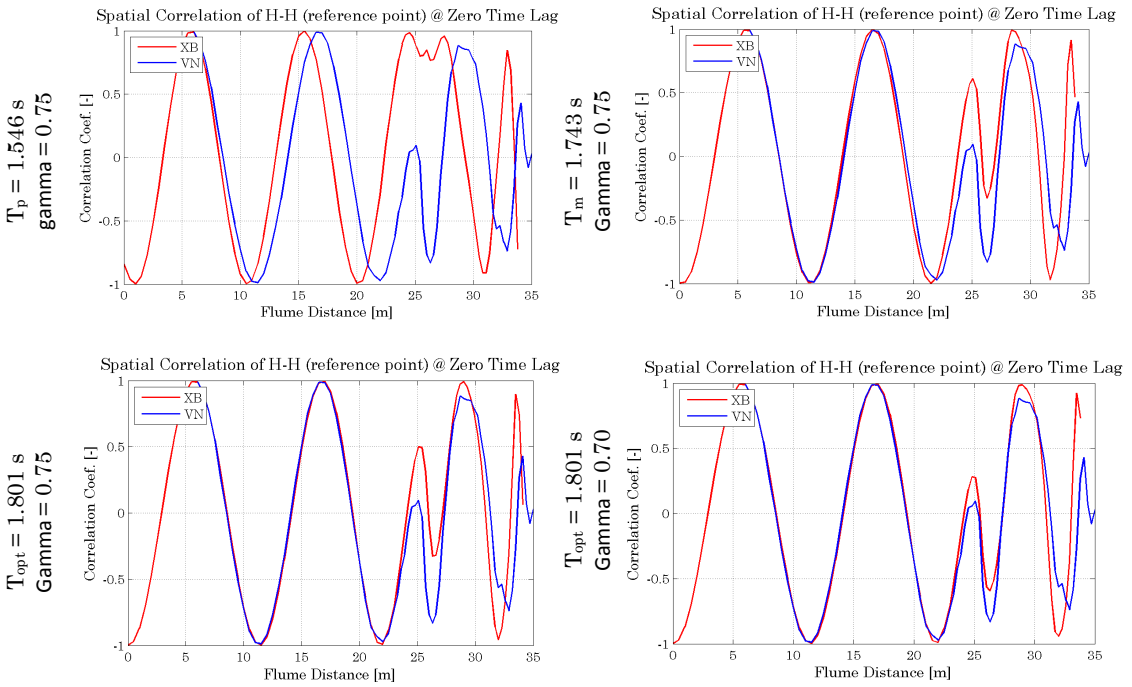

Figure 5.3: Spatial auto-correlations of H at zero time lag for XBeach results (red lines) and for van Noorloos case A-2 data (blue lines) with break = 3 for different values of Trep and gamma.

cases in the deepest section of the flume (where depths are constant). This is equal to 1.72 m/s. whereas c_g obtained from XBeach results in the same section of the flume 1.68 m/s.

Also, assuming that the distance between the first positive and negative peaks in the correlations in Figure 5.3 is approximately equal to half the wavelength of H (even though there is in reality a slight distortion due to shoaling effects), we can determine from linear wave theory that T_{rep} should in fact be approximately 1.77 s.

5.1.3.3 Breaker Parameter

In Figure 5.2, we see an obvious shift in the auto-correlation around 25 m. This is indicative of the point of inflection[6] of the wave height during wave breaking. In Figure 5.3, the inflection point is shown (more exactly) as the point at which the sinusoidal variation of the auto-correlation coefficient seems to reverse (where there is a slightly lower peak). In the bottom left plot, a value of 0.75 is used for the breaker parameter, gamma, with break = 3 for case A-2. The breakpoint of XBeach is shown to be more shoreward than for the VN data. By reducing gamma to 0.70, the breakpoint position of XBeach is corrected to the exact breakpoint position of VN as shown in the bottom right plot.

This procedure is used to determine the value of gamma used in the model runs. As shown in Table 4, the value of gamma remains constant for all cases with the break = 4 option, but with the break = 3 option, it is varied in series B where the amplitudes of the primary waves are steadily increased.

[6] Explained in more detail subsection 5.2.3

5.2 Short Wave Shoaling and Dissipation

5.2.1 Time-Averaged Results

The RMS short wave height, H_{rms}, varies at the scale of the wave groups, however we can obtain time-averaged values by either considering the time series itself or the wave envelope. $H_{rms,VN}$ is determined directly from the VN measured data (assuming Rayleigh distributed waves) as

$$H_{rms,VN} = 2\sqrt{2}\sigma_{\hat{\eta}_{VN}} . \tag{5.2}$$

$H_{rms,\mathrm{XB}}$ is determined as the time-averaged RMS value of the XBeach output parameter, H, as

$$H_{rms,XB} = \sqrt{\overline{H^2}} . \tag{5.3}$$

Other time-averaged parameters, such as E and S_{xx} which also varies at the scale of the wave groups according to (2.35) and (2.39) respectively, can be determined in a similar fashion as H_{rms}. The time-averaged values of these parameters are taken over a varying number of wave groups. Given that the range of difference frequencies in series A is between 0.0977 and 0.1953 Hz, the number of wave groups during the 327.68 s timeseries ranges from 32 to 64 respectively. For series B, there are a total of 48 wave groups.

Figure 5.4 and Figure 5.5 shows the results of the short wave parameters obtained from the VN data[7] and from the model output of XBeach (for the options break = 3 and break = 4) for series A and series B respectively. For series A, the amplitudes of the primary waves are relatively constant, therefore the short wave RMS values will be the similar for each test case as seen in Figure 5.4. For series B, the primary wave amplitudes are varied and therefore the difference in RMS values between the cases are seen Figure 5.5.

5.2.1.1 Wave Shoaling

What is particularly interesting in both Figure 5.4 and Figure 5.5 is that in the (top) plots of H_{rms} there is no shoaling of the measured short waves according to $H_{rms,\mathrm{VN}}$. On the other hand, $H_{rms,\mathrm{XB}}$ shows a steady increase of the wave heights up to the breakpoint, which is what is theoretically expected. The relative 'over-shoaling' of $H_{rms,\mathrm{XB}}$ when compared to $H_{rms,\mathrm{VN}}$ further translates to differences in the computed energy, E, and radiation stress, S_{xx}, in the vicinity of the breakpoint.

This difference may be explained by the change in the shape of the measured waves in the VN experiment leading up to and during the course of wave breaking. Results indicate that the measured short waves become more asymmetrical and skewed as they shoal towards breaking mainly due to increasing non-linearities. This effectively reduces the energy in the measured short wave band as more energy is transferred to higher and lower frequencies (later shown in section 5.2.4).

[7] The measured data, presented in the left column plots of Figure 5.4 and Figure 5.5 for series A and series B respectively, show inconsistencies at specific wave gauges, primarily located between 17 m and 23 m. In series A, these 'inconsistencies' consistently manifest themselves as 'bumps' in the (time-averaged) data at the same locations for each wave case. In series B, the bumps are also intermittently spaced. It is believed that the root cause of this is due to inaccurate calibration of the resistance (voltage) measurements from the wave gauges, which can be observed when viewing the spatial wave propagation in the flume in a video format. We can still see, however, that the error is localized and does not detract from the general comparison with the XBeach results.

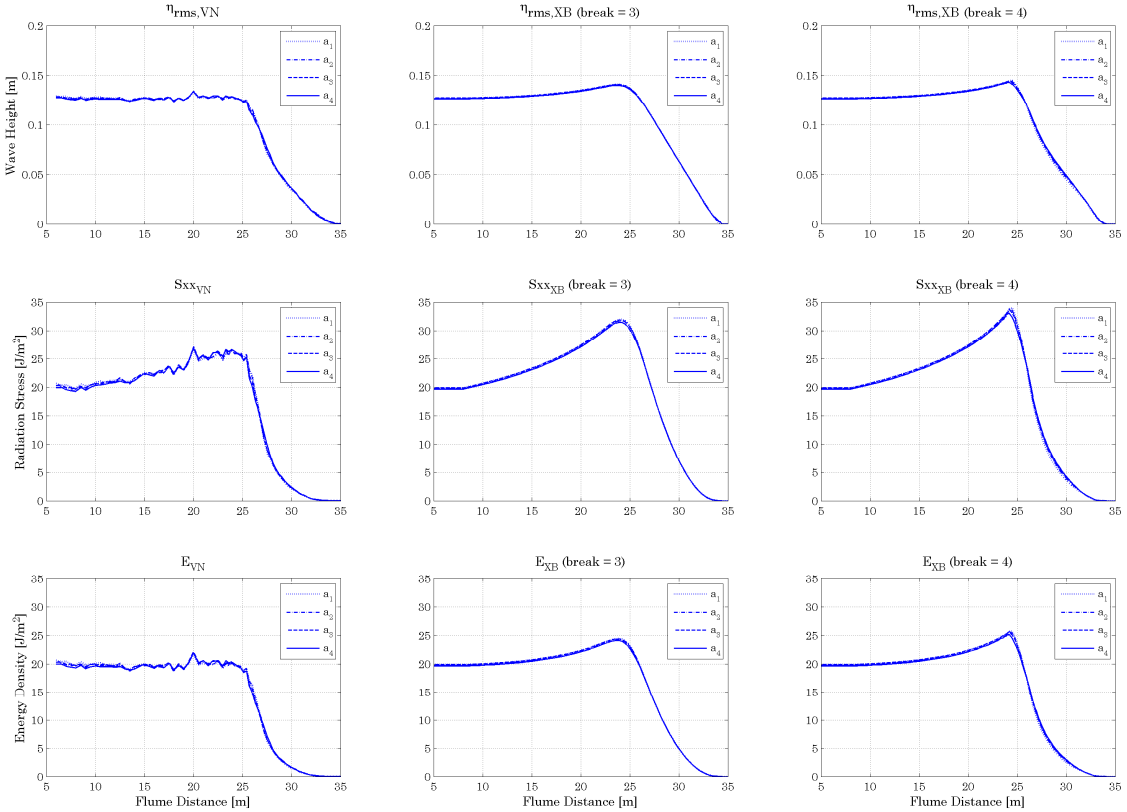

Figure 5.4: Spatial variation of H_{rms} (top row) radiation stress, S_{xx} (middle row), and HF energy, E (bottom row), for van Noorloos data (left column) and XBeach model results for the options break = 3 (centre column) and break = 4 (right column) for series A.

As energy is conserved seaward of the breakpoint, non-linear energy transfers within the short wave spectrum of XBeach is not possible, therefore resulting in the overestimates.

5.2.1.2 Dissipation through Breaking

In terms of wave dissipation through breaking, the results from the XBeach break = 4 option shows good agreement with the VN data, aptly representing the short wave breaking process which is characterised by, initially, a highly accelerated dissipation rate and, subsequently, a moderate dissipation rate toward the shoreline. In series B, knickpoints in the breaking zone are evident in the cases with higher primary wave amplitudes, such as case B-5. These knickpoints are also reproduced by the model when using break = 4. Using the break = 3 option in XBeach, the breaking process is shown to be monotonous, with a more or less constant rate of dissipation from the breakpoint to the shoreline, which is not necessarily the case in nature.

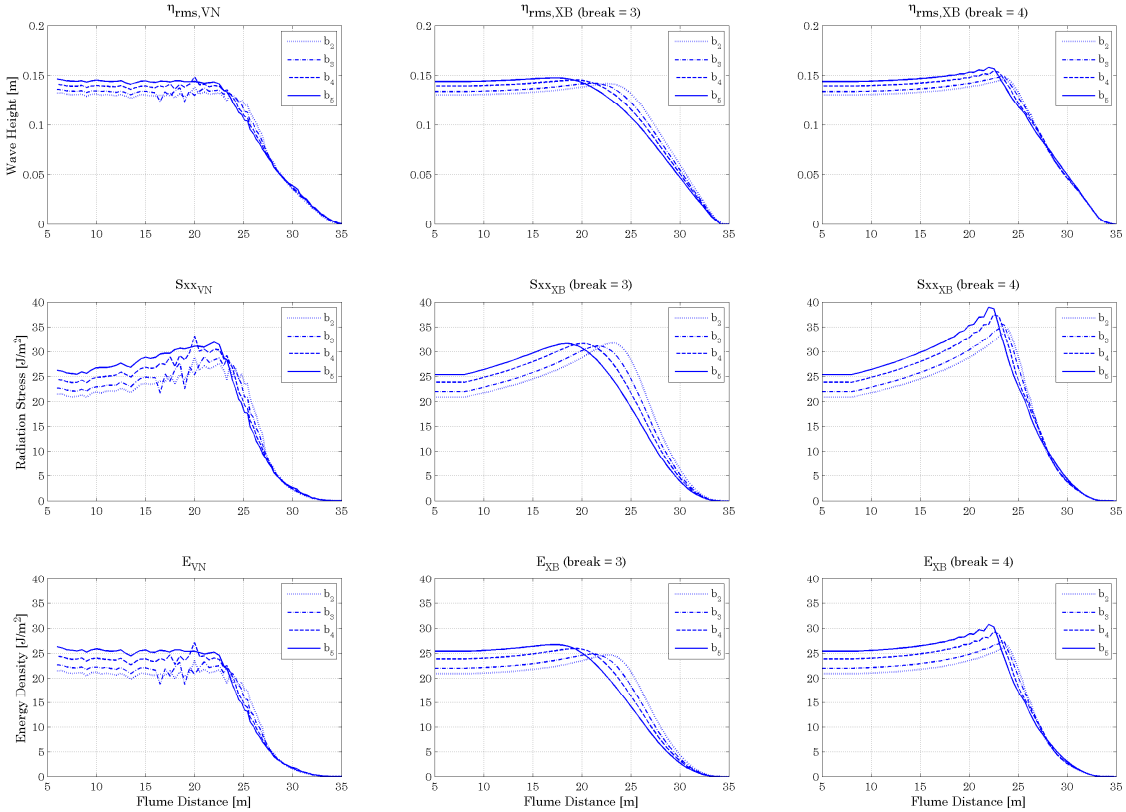

Figure 5.5: Spatial variation of H_{rms} (top row) radiation stress, S_{xx} (middle row), and HF energy, E (bottom row), for van Noorloos data (left column) and XBeach model results for the options break = 3 (centre column) and break = 4 (right column) for series B.

Breaking is shown to be abrupt for the break = 4 option, particularly in series B (Figure 5.5) but the transition is much smoother, albeit delayed, for the break = 3 option. This results in a narrow breaker zone width achieved with the break = 4 option for series B, which is comparable to the results of VN. The wider breaker zone obtained when using break = 3 is due to the variation of gamma (as shown in Table 4) in order to optimize the auto-correlation (discussed in 5.1.3.3).

5.2.2 Spatial Evolution of Timeseries

A closer look at the spatial evolution of the timeseries of H_{XB} and H_{VN} from the latter section of the shoaling zone ($20.0 < x < 23$ m) through the breaking zone ($23 < x < 29$ m) and into the shallow water zone ($29 < x < 35$ m) reveals idiosyncrasies of the behaviour of the wave groups. H_{XB} is given directly as output from XBeach, however we determine H_{VN} from the envelope of the timeseries of the VN HF data (explained in Appendix B).

Figure 5.6 shows the timeseries of H_{VN} (upper plot) and H_{XB} for the command options break = 4 (centre plot) and break = 3 (lower plot). Figure 5.6 shows that, in the latter section of the shoaling zone (blue lines), H_{XB} is increasing in height (shoaling) compared to H_{VN} which is reducing in height. This is representative of the 'over-shoaling' of H_{XB}. A distinctive feature of Figure 5.6 is the variance of the different timeseries plots. H_{VN} is shown to contain more variance or groupiness than H_{XB}.

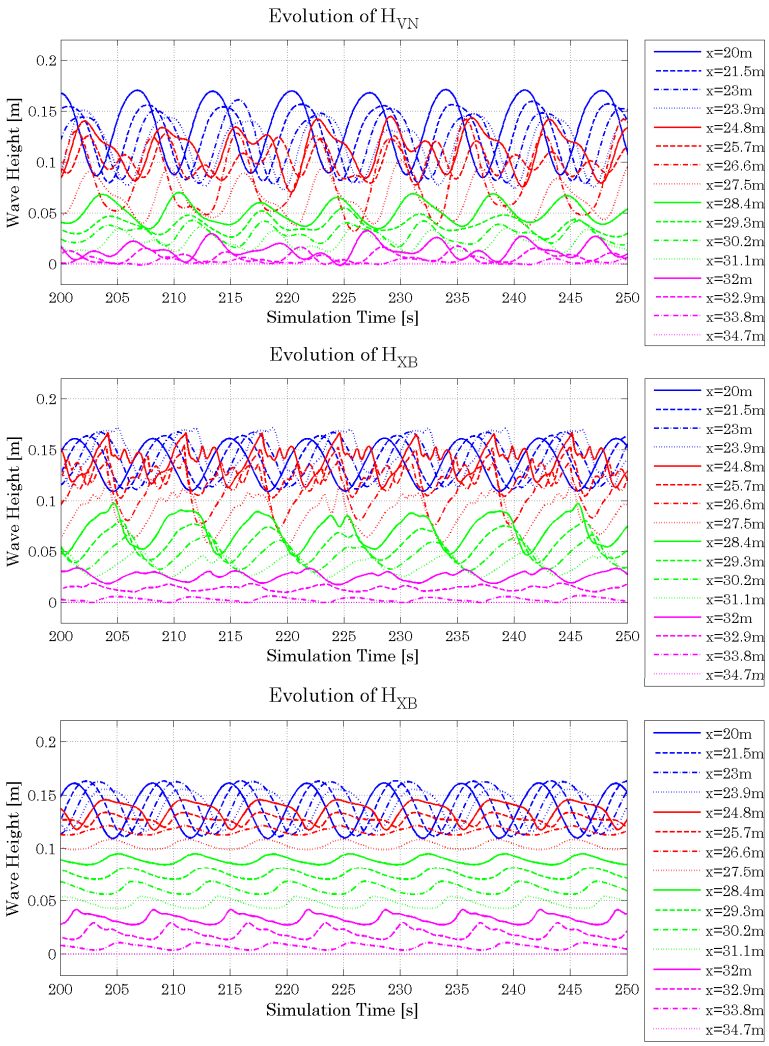

Figure 5.6: Spatial evolution of the group varying short wave height timeseries, H, from the end of the shoaling zone (blue lines), to the onset of breaking (red lines), through the latter stages of breaking (green lines), and in shallow water (pink lines) for van Noorloos data (top), XBeach break = 4 data (centre) and XBeach break = 3 data (bottom).

A groupiness factor [List (1992)], given in (2.31), is used to determine the groupiness of the waves as they shoal and break, which is shown in Figure 5.7 and Figure 5.8. In these figures, the short waves in XBeach are shown to contain less groupiness than the short waves in VN, which is what is observed in Figure 5.6.

The short waves of VN contain more groupiness due to the increased presence of non-linearities in the shoaling zone, which dramatically increases even further in the breaking and shallow water zones (see subsection 5.2.4). Non-linearities are not modelled in XBeach and therefore the groupiness will (expectedly) be somewhat lower. With the break = 3 option, the groupiness of the waves disappear during breaking, but with break = 4, the groupiness is still present, which is actually what is seen in reality.

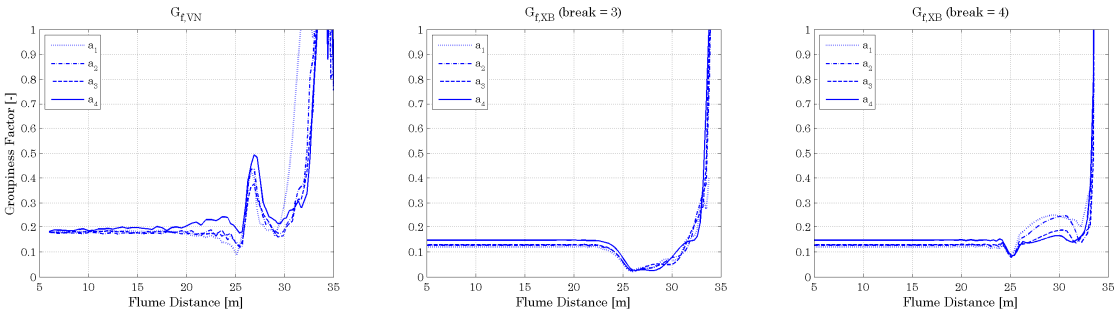

Figure 5.7: Groupiness factor of the group varying short wave height, H, for van Noorloos (left) and XBeach break = 3 (centre) and break = 4 (right) data for series A.

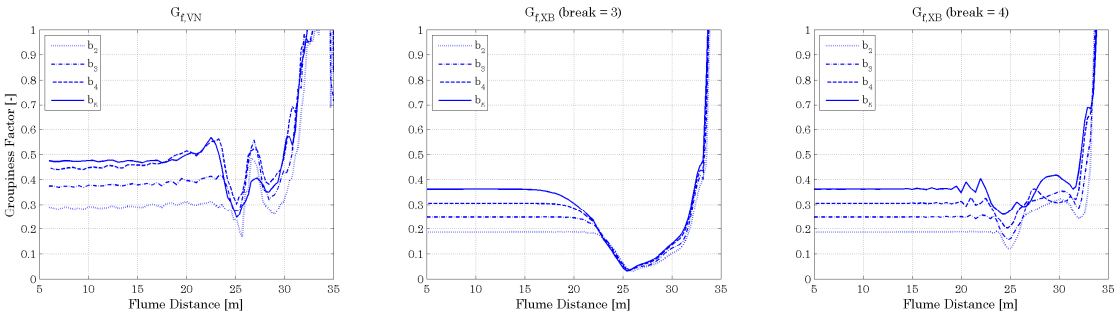

Figure 5.8: Groupiness factor of the group-varying short wave height, H, for van Noorloos (left) and XBeach break = 3 (centre) and break = 4 (right) data for series B.

During breaking, the higher waves in the group break first, followed by the lower waves. This affects the top envelope of the waves, as the crest of the envelope begins to decrease in height. The depression in the envelope crest continues to occur as the short waves propagate and continually break. As such, the crest of the wave envelope appears to devolve into the trough and the trough of the envelope then turns into the crest. In the midst of the breaking process, a high frequency component will be induced in the wave envelope (and thus the group-varying wave height), which results in a saw-toothed pattern during wave breaking.

5.2.3 Propagation of Group-Varying Wave Height and Surface Elevation

An example of the propagation of the group-varying wave height, H, and the (LF) surface elevation, ζ, is shown in Figure 5.9. The waves progress through the flume starting with the dotted lines and ending with the solid lines. Here, H_{VN} (top plot) shows significant reduction in height as the higher waves in the group break. The height is restored to a maximum when the next group of waves move toward the initial breakpoint at x = 22 m.

An important feature shown in the plots (as mentioned in the previous section) is the *inflection point* in the breaking zone. Up to this point, the crest of H devolves until it is the same height as the trough. Beyond this point, the trough of H then turns into the crest and vice versa. This occurs at approximately x = 25 m, and is clearly visible in the plots in Figure 5.9. The groupiness of H is at its lowest at this location, as shown in Figure 5.7 and Figure 5.8. The inflection point is also shown in the auto-correlation plot in Figure 5.3, where it is used to calibrate the XBeach input parameter gamma. The short waves are later shown to be in phase with the LF surface elevation beyond this point, which can be interpreted as the point of release of the LF waves.

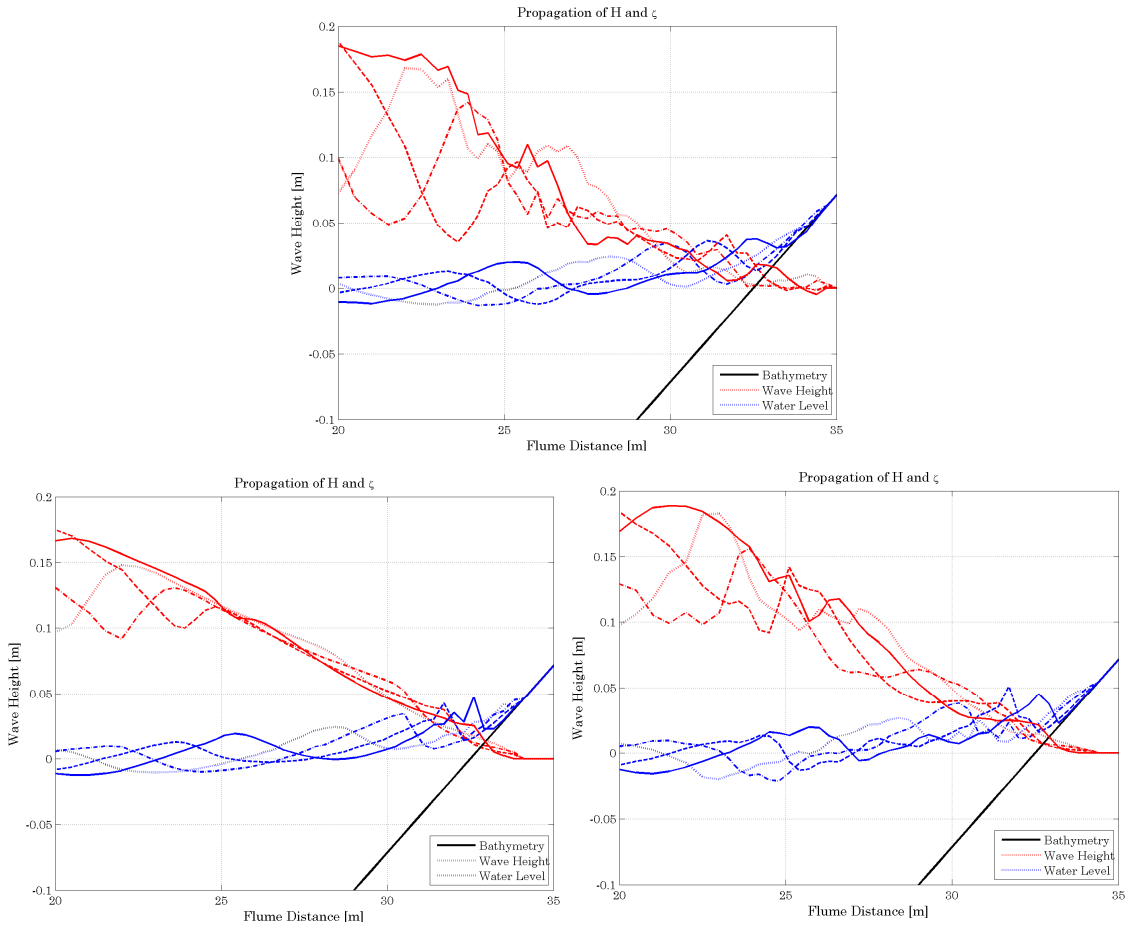

Figure 5.9: Propagation of the group-varying short wave height, H (red lines), and the (LF) surface elevation, ζ (blue lines), for van Noorloos (top) and XBeach break = 3 (bottom left) and break = 4 (bottom right) data for case B-4.

With break = 3 in XBeach (bottom left plot), the waves are shown to start breaking before the initial breakpoint of the measured waves at 22 m and the variance in the height of H_{XB} is limited beyond the point of inflection (as previously mentioned). With break = 4, significant improvement is obtained regarding wave breaking. The initial point of breaking is similar to the measured data and there is greater variance in the shallow water zone (beyond the inflection point).

The (LF) surface elevation is shown to run-up the beachface in Figure 5.9. XBeach is shown here to be able to represent wave run-up. Compared to the measured data, the front of the LF wave appears to be over-steepened in XBeach, and does not reach the same maximum run-up height as the measured data suggests.

5.2.4 Spatial Evolution of Amplitude Spectrum

The spatial evolution of the amplitude spectrum of the group-varying RMS wave height, H, is shown in Figure 5.10. Since H varies at the scale of the wave groups it has a peak frequency equal to the difference frequency ($f_b = f_1 - f_2$). In Figure 5.10 it is shown that, for both the XBeach model output and the VN data, energy diffuses above and below f_b at the breakpoint in response to the evolution of the wave envelope (mentioned in subsection 5.2.2).

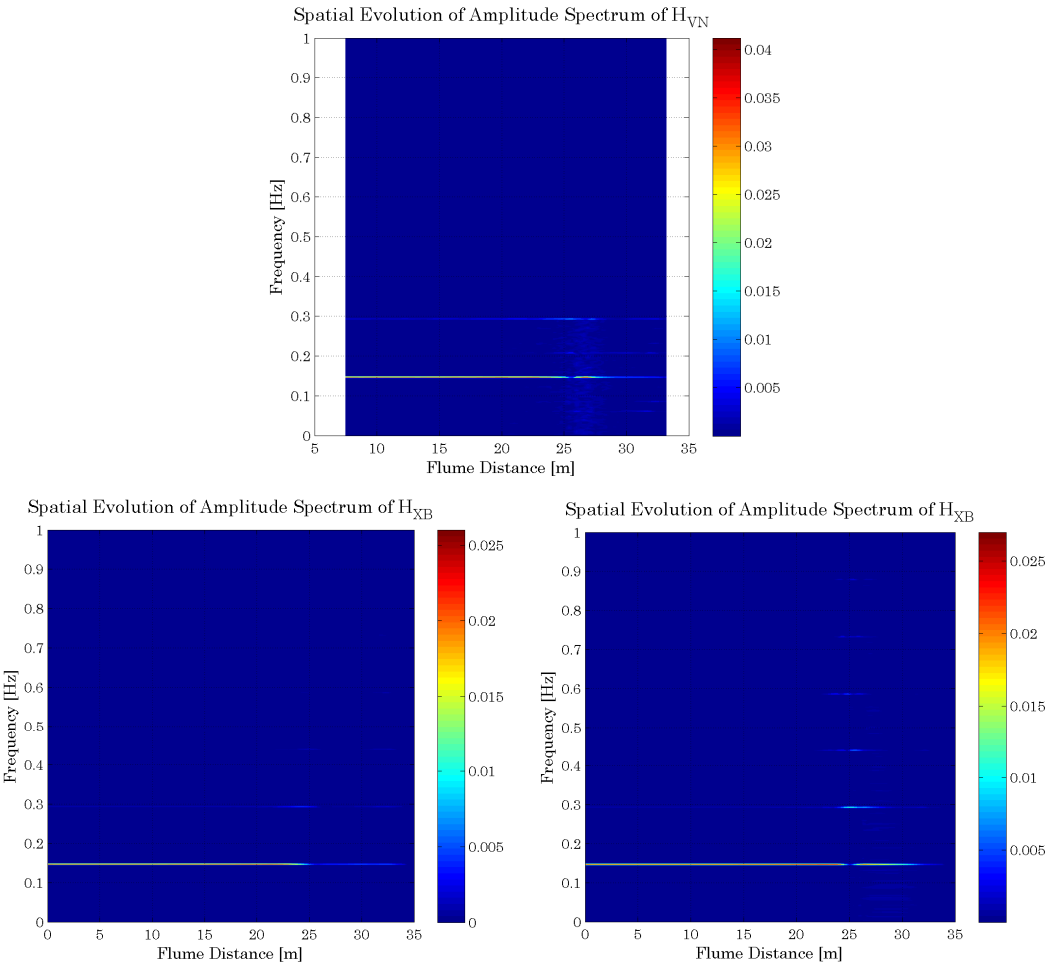

Figure 5.10: Spatial evolution of the amplitude spectrum of *H* for van Noorloos (top) and XBeach break = 3 (bottom left) and break = 4 (bottom right) data.

In the results of VN we see that the shift of energy from f_b to higher frequencies at the breakpoint and temporarily reduces the local amplitude of *H* at f_b and thereby shifts the peak frequency upwards. The amplitude of *H* at f_b is subsequently restored after the initial breakpoint. This is feature is also represented in XBeach when the break = 4 option is used. The break = 3 option captures the correct location of the breakpoint where this change takes place (given that the parameter gamma has been calibrated well), however, the amplitude of the wave envelope is not restored after the breakpoint, as it continually decreases toward the shoreline.

Figure 5.11, Figure 5.12 and Figure 5.13 each shows several 2D amplitude spectra plots of the measured VN data (red lines), which includes both HF and LF components, and of the surface elevation output from XB beach (blue lines), which contain only the LF wave components, plotted at locations in the shoaling zone, breaking zone and shallow water zone respectively. Figure 5.11 shows the two amplitudes of the primary wave input in the VN experiment and their individual frequencies. The two incident wavetrains remain distinguishable throughout the shoaling zone, with slight energy gains at f_b and above the primary frequencies (super-harmonics). Figure 5.12 shows that while the primary waves are still somewhat distinguishable at the beginning of breaking, at the end of the breaking process, their amplitudes greatly reduce and the amplitudes of the super-harmonics greatly increases such the waves components are highly non-linear.

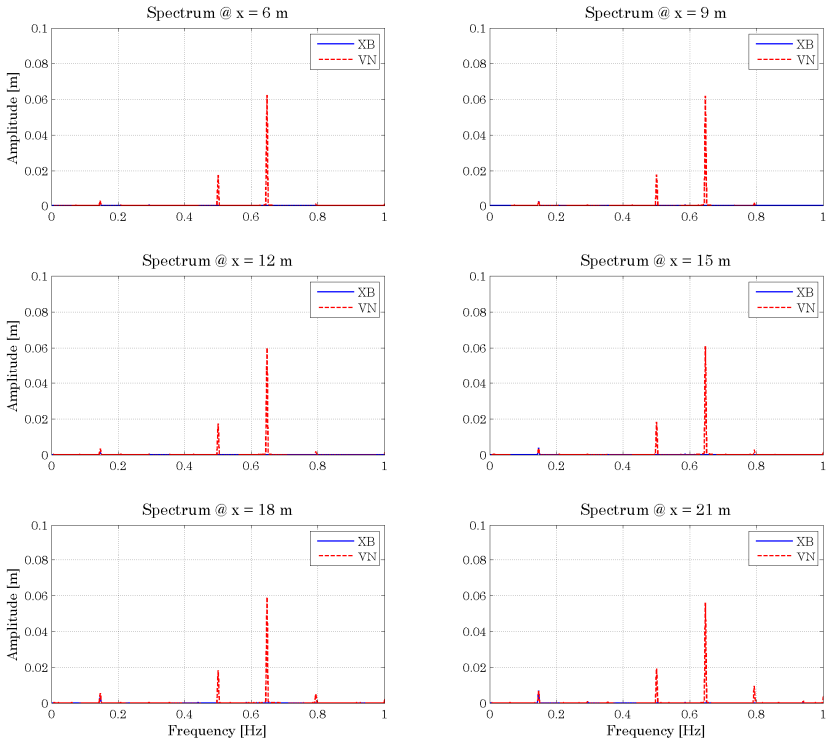

Figure 5.11: 2D amplitude spectrum of η for van Noorloos (red lines) and ζ for XBeach (blue lines) in the shoaling zone for break = 3 case B-2.

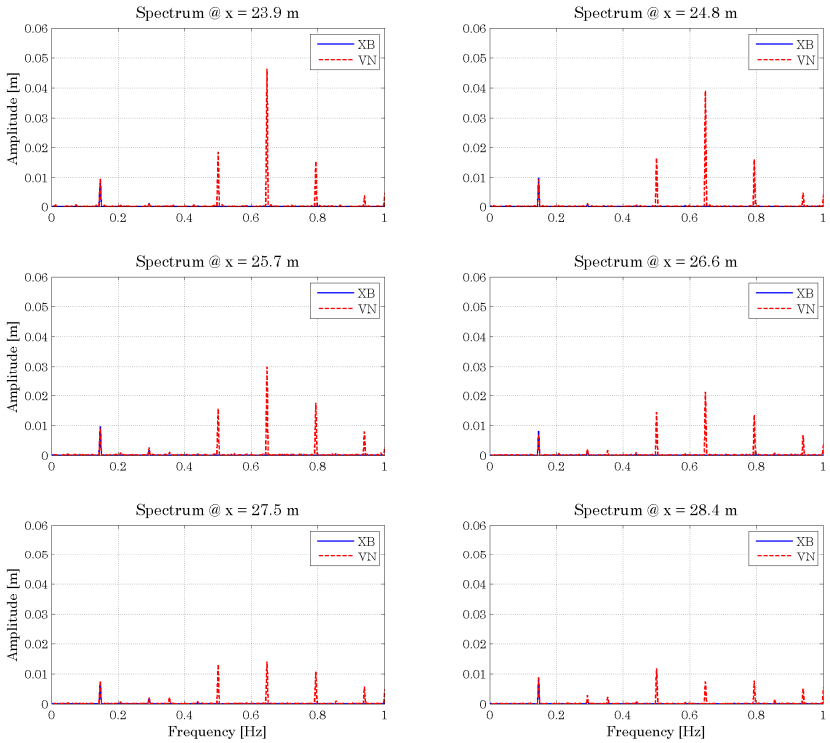

Figure 5.12: 2D amplitude spectrum of η for van Noorloos (red lines) and ζ for XBeach (blue lines) in the breaking zone for break = 3 case B-2.

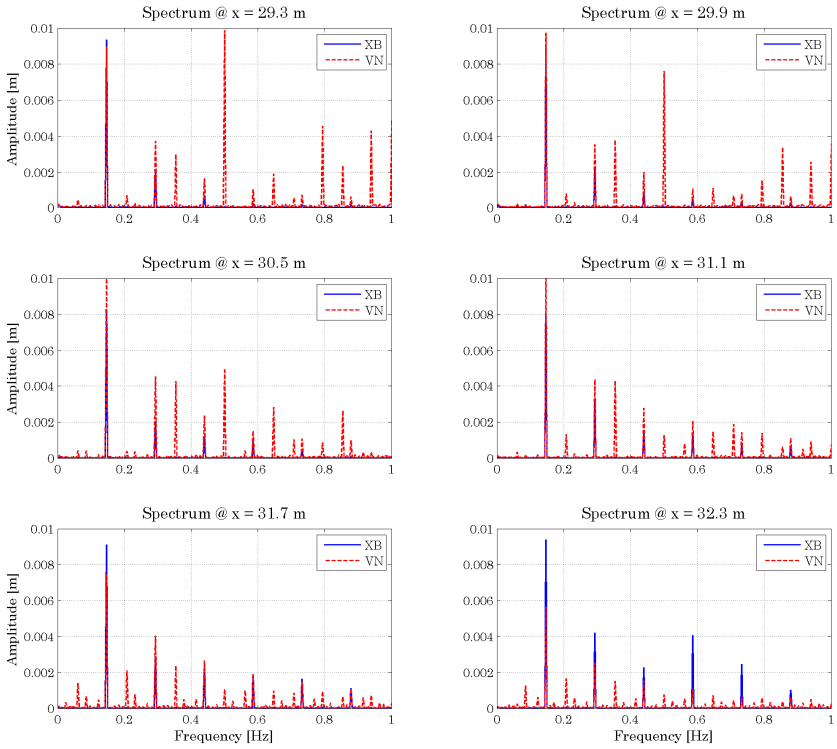

Figure 5.13: 2D amplitude spectrum of η for van Noorloos (red lines) and ζ for XBeach (blue lines) in the shallow water zone for break = 3 case B-2.

Figure 5.13 shows that in the shallow water zone the measured VN wave spectrum is very complex. The LF wave (at frequency f_b) is now the wave component with the highest amplitude, showing that in shallow water, the LF waves are dominant. An added feature of the spectrum in shallow water is that energy is transferred to frequencies which are not integer multiples of f_b (as previously seen in the shoaling and breaking zone). This can possibly be explained by the fact that there are more free waves in this zone after their release from the primary waves in the breaking zone. There is therefore much more wave-wave interactions in shallow water which produces the very complex spectrum. The spectrum obtained from the XB surface elevation output (blue lines) include the effects of the higher harmonics only at integer multiples of at f_b.

The growth and reflection of LF waves is discussed in more detail in subsection 5.3 following.

5.3 Low Frequency Wave Shoaling and Reflection

5.3.1 Influence of Model Parameters

The IBLF and RFLF waves ($\zeta_{XB,in}$ and $\zeta_{XB,out}$ respectively for XBeach data and $\zeta_{VN,in}$ and $\zeta_{VN,out}$ respectively for VN data) are determined using the decomposition technique discussed in Appendix C. In the previous subsection, we have already optimized the model input parameters which control the short waves (in the wave module of XBeach). We can now assume that the forcing computed from our short waves is as accurate as (currently) possible. This infers that differences between the measured LF data from VN and the LF model output from XBeach have to be resolved (optimized) by varying XBeach input parameters within the flow module.

The IBLF and RFLF results from XBeach have been found to be sensitive to the input eps and C parameters. The eps controls the threshold depth above which a cell is considered to be wet. This therefore varies the position of the most shoreward grid cell. As such, the grid resolution is also important to determine the exact spatial limit of wave run-up.

The Chezy friction coefficient, C, is related to the roughness of the bed. The bed shear stress terms in the NSW equations, given in (3.22) and (3.23), affects the LF wave heights, particularly in shallow water, by reducing the momentum and thereby acts as a dissipative term. In the following sub-sections, the effect of the eps, C and grid resolution is discussed for each bichromatic wave series. Plots of the LF results for these additional test runs are given in Appendix E.

5.3.2 Series A Decomposition Results

5.3.2.1 Base Case

In series A, f_b is varied while keeping the amplitudes of the primary waves relatively constant. The RMS values of the total LF, IBLF and RFLF waves obtained from the decomposition of the VN data are shown in Figure 5.14 (left column). These plots indicate that the rate of shoaling of the IBLF wave decreases with f_b while the RFLF wave heights increase. This as expected, given that the (empirical) reflection coefficient, R_f, in (2.63) is a function of the normalized bed slope, β, in (2.62). For larger values of β, the growth rate of LF waves is small, but larger reflections are observed, indicating that longer waves reflect better.

The XBeach results shown in Figure 5.14 for the break = 3 (centre column) and break = 4 (right column) options does not represent the decreased shoaling rate of the IBLF waves with decreasing value of f_b. In all cases, the shoaling rate of the IBLF wave remains constant up to the breakpoint. For break = 3, the IBLF wave heights initially stops shoaling at the breakpoint, similar to the VN results, but subsequently it slowly begins to shoal again up to the shoreline. The IBLF wave heights predicted with break = 4 stop shoaling at the breakpoint and then begins to decrease just beyond it, similar to the VN results. The main difference in this case is that the IBLF wave heights begin to shoal again in the VN results, apparently when the IBLF waves are themselves in water depths which are comparable to its height, but they do not recover in the break = 4 results, except for case A-1.

There is also some uncertainty with the RFLF waves. For case A-1, the RMS values are greater compared to the results of A-2 and A-3 when it should in fact be lower. These results indicate that the effect of varying f_b is not recognized well by the model. With break = 4, the RFLF wave heights in shallow water are lower than when break = 3 is used. As break = 3 gives the better estimates for the RFLF wave heights when compared to the measured data, the above observation suggests that some interference may be occurring in the shallow water region when break = 4 is used.

5.3.2.2 Test Cases

Decreasing the value of C from 70 to 50 (shown in Figure E.2) results in a slight decrease in both the IBLF and RFLF wave heights in shallow water of approximately 5 %, which is expected, but is not very significant.

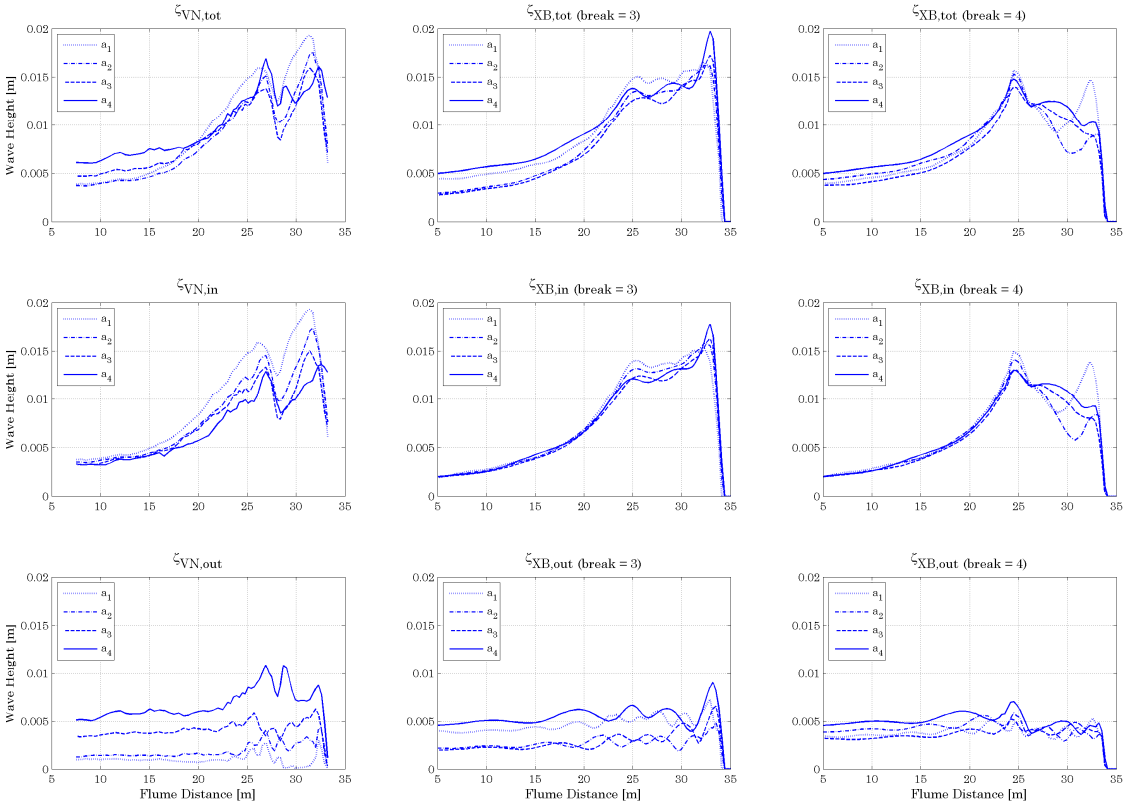

Figure 5.14: Spatial variation of RMS values for the total (top row), inbound (centre row) and reflected (bottom row) LF waves from the van Noorloos (left column) and XBeach break = 3 (centre column) and break = 4 (right column) data for series A. (eps = 0.001, C = 70, grid 1).

Increasing the value of the eps (shown in Figure E.1) mostly affects the RFLF wave heights by noticeably increasing its value by approximately 30%, however, for case A-1 the wave heights remain about the same. The increase in the RFLF wave height can be explained by the fact that the eps seemingly imposes a wall at the beach, therefore, for larger values, the height of the wave at the shoreward limit is greater and thus more reflection will occur. Interestingly, increasing the eps has placed the RMS values of case A-1 in the correct position relative to the other cases.

Increasing the grid resolution by a factor 2 in the *x*-direction (*grid 2*) (shown in Figure E.3) mainly improves the XBeach RLFL wave height estimates by widening the distribution of the wave heights from case A-1 through to case A-4, therefore being more equivalent to the distribution as seen in the measured VN data. With break = 4, the RFLF wave heights in shallow water are still lower than when break = 3 is used.

5.3.3 Series B Decomposition Results

5.3.3.1 Base Case

In series B the amplitude of the primary waves are varied such that the modulation is increased while maintaining a constant difference frequency. Figure 5.15 shows the cross-shore variation of the total LF, IBLF and RFLF waves (top, centre and bottom rows) obtained from the decomposition of the VN data and XBeach break = 3 and break = 4 data (left, centre and right columns).

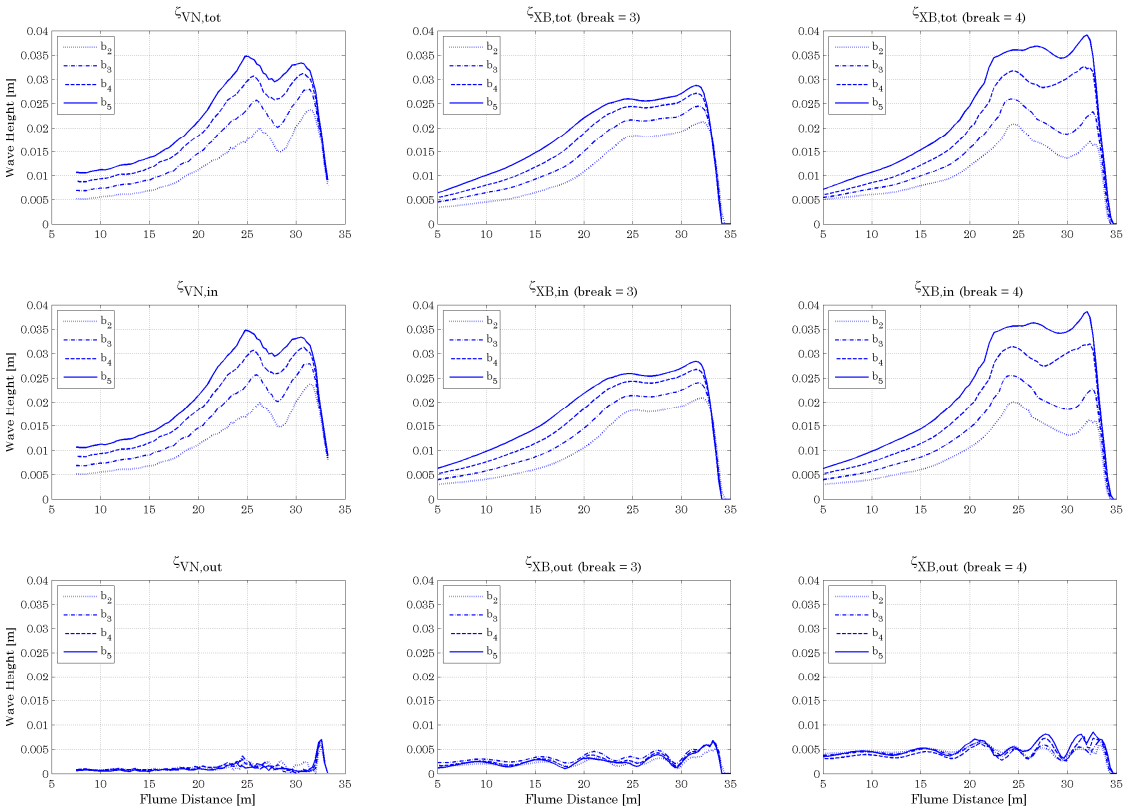

Figure 5.15: Spatial variation of RMS values for the total (top row), inbound (centre row) and reflected (bottom row) LF waves from the van Noorloos (left column) and XBeach break = 3 (centre column) and break = 4 (right column) data for series B. (eps = 0.001, C = 70, grid 1).

In subsection 5.2 it is shown that greater radiation stress gradients are developed with increased modulation, which in turn increases the RMS wave height of the IBLF wave as shown in Figure 5.15. As the difference frequency is fixed, the reflected LF wave heights are shown to be of similar magnitude. The XBeach results in Figure 5.15 show good agreement with the measured data in the shoaling zone, however with the break = 3 option, the IBLF wave heights are relatively underestimated by approximately 14% in the breaking and shallow water zones while with break = 4 there is a general overestimation in these areas, also by approximately 14%. The RFLF wave is overestimated in both breaker options where an eps value of 0.001 m is used.

5.3.3.2 Test Cases

Decreasing the value of C from 70 to 50 (shown in Figure E.5), as with series A, only slightly reduces the heights of the LF waves in shallow water by approximately 5% and does not noticeably affect the phase of the LF waves.

The results obtained when the value of the eps parameter is increased to 0.005 m (shown in Figure E.4) do not change significantly the IBLF wave heights, however the XBeach RFLF waves are just about doubled in height when compared to the former case (eps = 0.001 m). In addition, the phase of the waves are apparently shifted more seaward as a result of the lower run-up limit on the beach. Given that the results do not change much from what is shown in Figure 5.15 if the

eps is decreased, it suggests that 0.001 m is the lowest value which can be used with reasonable results (for this particular flume experiment).

Using a more refined grid (*grid 2*) we would expect that the RFLF waves would be improved when also using an eps value of 0.001 m. Surprisingly enough, the results (shown in Figure E.6) shows that the model becomes unstable in the deepest parts of the flume. High frequency noise pollutes the underlying LF wave height fluctuations. The short wave estimates remain the same, therefore the error occurs in the flow module of XBeach. It is possible that changing the eps to a slightly higher or lower value may remedy this problem, but this was not investigated.

5.3.4 Phase Differences and Energy Transfer

Energy transfer from HF to LF waves, given in (5.4), occurs due to the effect of radiation stress gradients and phase differences between the short wave envelope and the IBLF wave. The phase difference, originally defined in (2.58), can also be computed in frequency space from the phase spectrum as

$$\Delta\psi = \left(\psi_{H(f_b)} - \psi_{\zeta(f_b)}\right) - \pi \tag{5.5}$$

where ψ is the argument of the FFT of $H(t)$ and $\zeta(t)$ respectively at the (difference) frequency f_b. Figure 5.16 and Figure 5.18 shows the calculated phase differences between H and ζ_{in} (top row) and for H and ζ_{out} (bottom row) for series A and series B respectively. In these plots, the phase variation is divided by π and wrapped between -1 and 1, therefore values of $\Delta\psi$ at -1 and 1 indicate that the envelope and LF wave are in anti-phase, and 0 indicates that they are in phase.

A particularly interesting feature of the phase differences computed from the measured data for the IBLF waves is that the difference is relatively constant in the shoaling zone, as opposed to starting from an initial value close to -1 and slowly increasing toward zero, which is what is expected. The results of XBeach shows the latter feature. Also shown in the plots is the fact that in shallow water, the measured HF waves and LF waves from the VN experiment are generally in phase with each other, indicates that the short waves are essentially 'riding' on top of the (LF) water level. For series A, the model results of XBeach using the break = 4 option does not show this feature as well as the break = 3 option does.

For series A, the cyclic frequency of phase differences of the RFLF waves decreases with decreasing value of the difference frequency as expected (longer waves). In series B, the cyclic frequency of the RFLF phase differences are constant for both the measured and XBeach results as the frequency is kept constant. The measured data shows varying spatial distributions of the phase difference for each wave case, indicating variable positions of the reflection point, which is expected since the amplitude of the waves are varied and therefore the run-up height increases for each case. The point of reflection in XBeach is seemingly within close vicinity for all the wave cases in series B.

Figure 5.17 and Figure 5.19 shows the energy transfer to and from the IBLF waves (top row) and RFLF waves (bottom row) at the difference frequency for series A and series B respectively. For series A, the model results compare fairly well to the measured data with the exception that for the break = 4 option there is an excessive loss of energy from the IBLF wave in shallow water. This is also shown in Figure 5.14, where the IBLF wave heights are underestimated in this area.

For series B, the energy transfer to and from the IBLF wave computed for the measured data is quite different from the results obtained from the model output. The model results indicate that

the energy transfer to and from the RFLF wave is similar for all the cases in series B, which is also shown in Figure 5.15. The oscillating nature of the RFLF wave energy transfer plots also forms a similar feature in the same plots with the wave height.

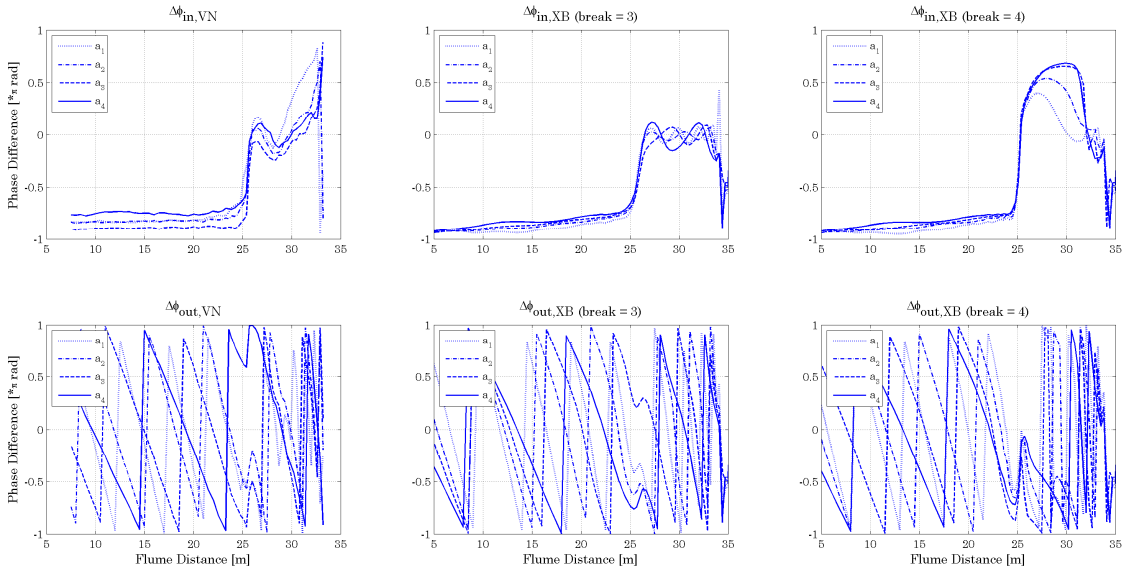

Figure 5.16: Phase difference between short wave envelope and (a) IBLF wave (top row) and (b) RFLF wave (bottom row) for van Noorloos (left column) and XBeach break = 3 (centre column) and break = 4 (right column) data for series A. (eps = 0.001, C = 70, grid 1).

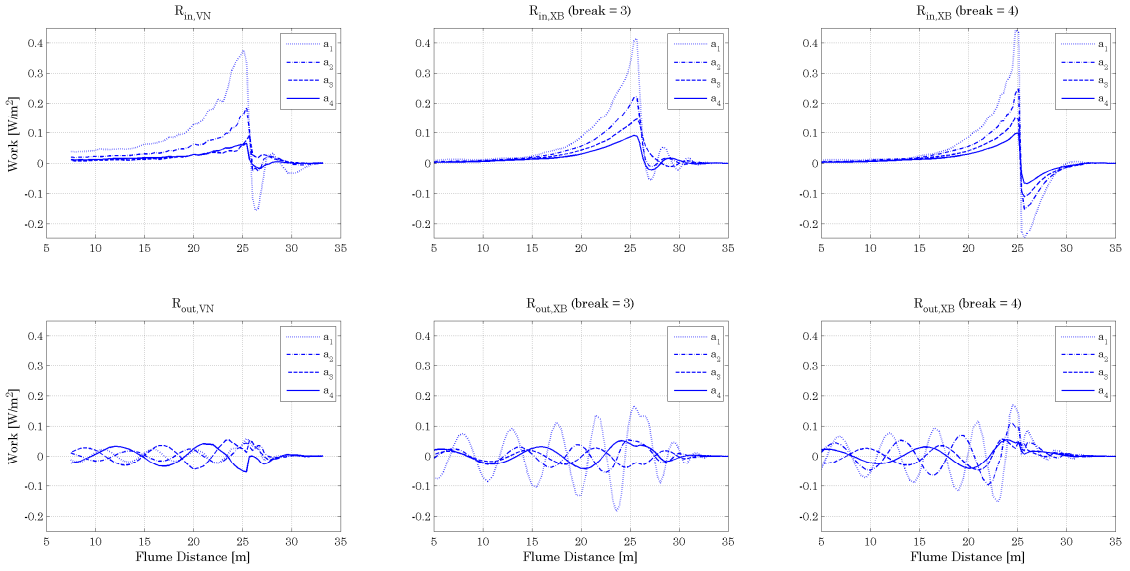

Figure 5.17: Energy transfer from HF to (a) IBLF waves (top row) and to (b) RFLF waves (bottom row) for van Noorloos (left column) and XBeach break = 3 (centre column) and break = 4 (right column) data for series A. (eps = 0.001, C = 70, grid 1).

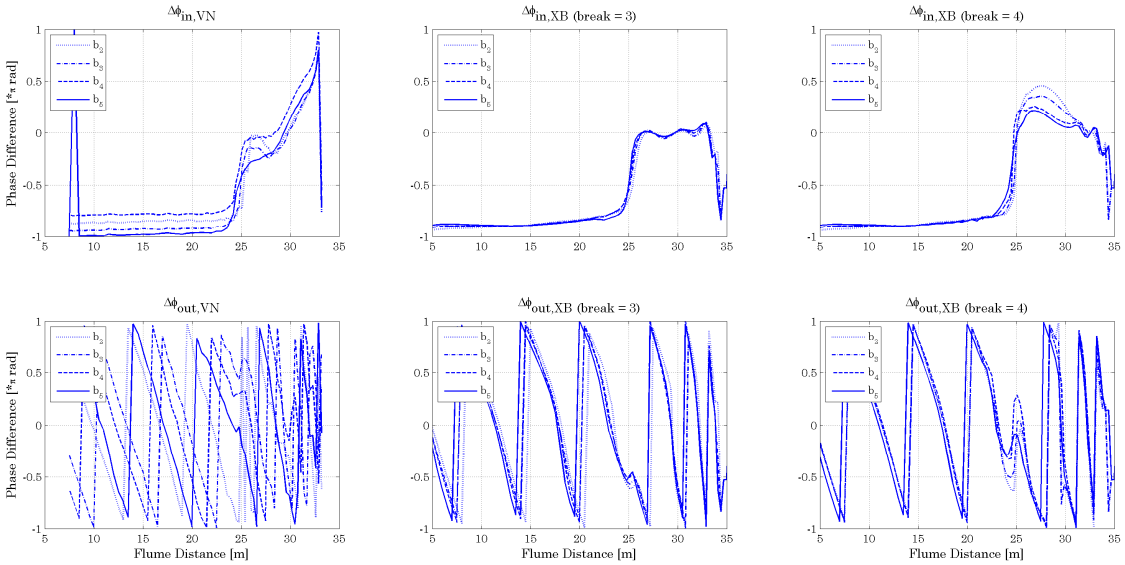

Figure 5.18: Phase difference between short wave envelope and (a) IBLF wave (top row) and (b) RFLF wave (bottom row) for van Noorloos (left column) and XBeach break = 3 (centre column) and break = 4 (right column) data for series B. (eps = 0.001, C = 70, grid 1).

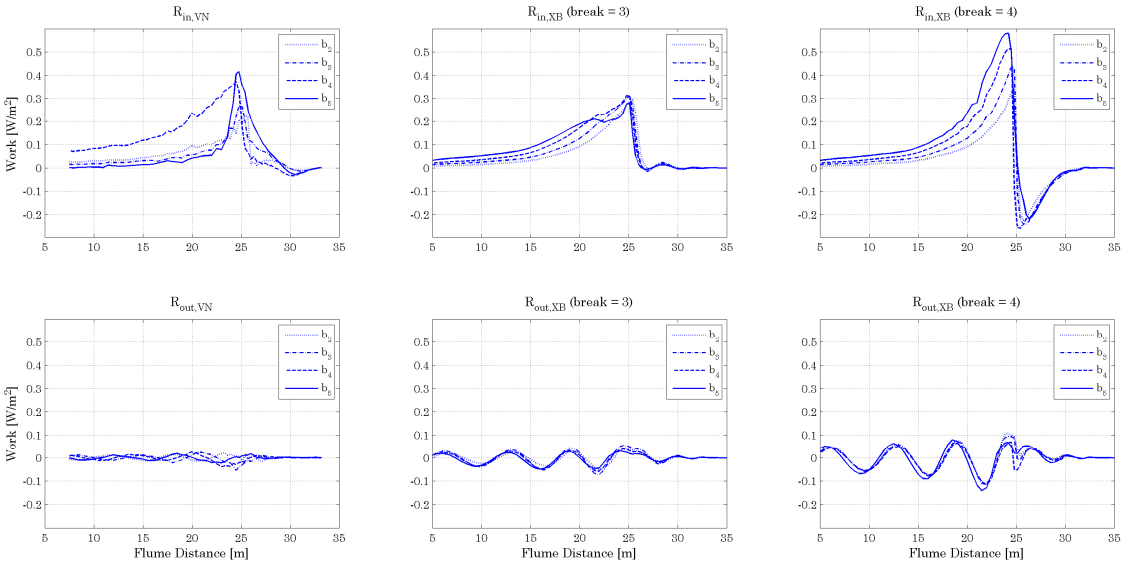

Figure 5.19: Energy transfer from HF to (a) IBLF waves (top row) and to (b) RFLF waves (bottom row) for van Noorloos (left column) and XBeach break = 3 (centre column) and break = 4 (right column) data for series B. (eps = 0.001, C = 70, grid 1).

5.4 Summary

5.4.1 Short Wave Estimates

The following is a summary of the short wave analysis for bichromatic waves:

- The difference between first order and second order wave energy input timeseries for instat = 3 in XBeach is negligible.
- The representative period, Trep, used in XBeach to determine the group velocity is optimized using the auto-correlation function. The optimal value (1.801 s) is different from the theoretical value, T_m (1.743 s) obtained when using (2.29). The reason for this difference is possibly due to the discretization of time and length scales XBeach (evidenced by the fact that T_m gives better auto-correlation results when a finer grid resolution is used). The difference between both periods is rather small, therefore T_m can still be used in model simulations of bichromatic waves.
- In the nearshore zone, the Doppler effect of wave-current interaction (WCI) (Stokes drift) causes variations in the relative group velocities in this region. This effectively distorts the natural group velocity of the waves in nature. WCI was not enabled in the XBeach simulations, therefore not accounting for this effect can lead to inaccuracies in nearshore propagation of the modelled HF waves. WCI might also be important in wave run-up on the beach.
- The crest of the envelope of the short waves devolves at the initiation of wave breaking until it is preceded by the trough. The point of inflection (the point where the trough of the group-varying wave height, H, morphs into the crest) can therefore be used to represent the exact location of the (average) breakpoint and can also serve as an indication of the point at which LF waves are released from the short waves since they are (at this point) in phase with H.
- The breaker parameter, gamma, is optimized using the auto-correlation function. For break = 3, the parameter is varied to best represent the inflection point in the breaker zone, but is constant when using break = 4. It is found that for increased modulation, the breaker parameter has to be reduced when using break = 3.
- XBeach tends to 'over-shoal' the short wave heights by up to approximately 8% (break = 3) and 10% (break = 4) which is probably due to the energy conservative scheme of the wave action equations up to the breakpoint, beyond which energy is only dissipated by breaking. Additional dissipation terms in the wave action balance equations, such as bed friction and non-linear wave-wave interaction, could help to reduce the short wave energy as it travels towards the shoreline.
- The groupiness of the short waves in XBeach does not include the effects of non-linearities and therefore might have less groupiness than the measured VN waves. With the break = 4 option the short wave groupiness in the breaking and shallow water zones is improved.
- For the measured VN data, non-linearities increase in the breaking and shallow water zones. The surface elevation results of XBeach (which are computed using the NSW equations) are able to capture not only the LF difference interactions, but also HF interactions of LF components.

- Spectral plots show that in both the measured data and in the XBeach water surface elevation results, LF energy is dominant in very shallow water.

5.4.2 Low Frequency Wave Estimates

The following is a summary of the LF wave analysis for bichromatic waves:

- Frequency dependent shoaling (series A) is not correct in XBeach and is probably influenced by the constant value of the representative wave period, Trep. We see, however, that shoaling is amplitude dependent (series B), but the rate of shoaling of the IBLF waves in XBeach is greater than what is observed.
- The position of the inflection point is shown to be important as it determines the point up to which energy is transferred to the LF waves, evidenced by the sharp decrease in energy transfer rates beyond this point, both in the measured and modelled results. Therefore, if it is made too early (using too high a value of gamma in XBeach), then IBLF waves will be essentially underestimated and vice versa if it is too late.
- The LF waves are shown to propagate similar to a bore during wave-run up. As such the IBLF waves surge up the beach and over-steepen. This may be due to neglecting the vertical component in the momentum balance of the NSW equations (only horizontal momentum is conserved). The over-steepening of the LF wave possibly prevents it from attaining the maximum run-up height when compared to the VN data.
- The position of the point of reflection (at the maximum run-up height) of the RFLF waves in XBeach is less variable (in response to short wave amplitude variations) when compared to the measured data. This affects the phase of the RFLF wave by narrowing the spatial range from which reflection occurs, thus RFLF waves in XBeach reflect at nearly the same point while we see a wider range in the VN data.
- In XBeach, the eps controls the amount of reflection of RFLF waves. As it effectively acts as wall at the top of the beach, the greater the value, the higher the wave height that is reflected. The eps is also shown to affect the phase of the RFLF wave by changing the most shoreward point in the computational grid (moving it seaward for higher values).
- Increasing the grid resolution improves the variation of RFLF wave height results in series A, however for series B, HF numerical oscillations are introduced at the offshore boundary. Increasing the grid resolution also gave improved results when T_m is used as Trep.
- The Chezy friction coefficient, C, does not significantly improve the LF wave estimates of XBeach in shallow water, however an approximate decrease of 5% is observed in the LF wave heights when C is decreased from 70 $m^{0.5}s^{-1}$ to 50 $m^{0.5}s^{-1}$.

5.4.3 XBeach Breaker Options

The following is a summary of the different breaker options in XBeach:

- break = 4 better represents the spatial limits of short wave shoaling and wave breaking dissipation than break = 3.

- break = 4 tends to incorrectly predict the phase difference between the short wave envelope and the IBLF wave in shallow water, which results in large reductions in the IBLF wave height in shallow water.
- With break = 4, a doubling of the default dissipation parameter, alpha, is required in order to obtain a similar steepness in the short wave dissipation as seen in the measured data.

5.4.4 Limitations and Sources of Error

The following is a summary of some of the limitations and possible sources of error in the analysis methods used for the measured data:

- The constant phase difference between *H* and the IBLF waves throughout the shoaling zone for the VN data is counterintuitive to what is expected, which is a steady increase from an initial phase shift close to -1 (anti-phase) toward 0 (in phase). However, the phase shifts determined by VN in his report suggest that the HF and IBLF waves are not in phase in shallow water, which is also counterintuitive. The likely caused by differences in the methods in which the LF waves are decomposed.
- The jumps in the data of VN (as mentioned in footnote 7) at similar cross-shore locations for each test case in series A and series B is quite strange but is possibly due to the calibration of the voltage/resistance of the individual wave gauges in the flume.
- The decomposition of the VN LF timeseries does not include the wave gauges which are above the still water level, therefore the actual limit of wave run-up is not directly shown in the decomposed LF results (it is, however, shown for the total LF waves).

Chapter 6 – Irregular Wave Case Results

In this chapter, similar to Chapter 5, the model output from XBeach simulations of the irregular wave cases of the VN experiment using the two breaker parameterizations (*Roelvink* [1993] and *Roelvink* [Pers. Com. 2009]) are compared to the measured data. Firstly, the main XBeach input parameters are discussed in Section 6.1. Secondly, the results of the short wave shoaling and dissipation are presented in Section 6.2 and, thirdly, the results of the decomposed LF waves are given in Section 6.3. Finally, a summary of the validation results is presented in Section 6.4.

6.1 Input Parameters

Table 5 below gives the values for the variable XBeach input parameters used for the irregular wave cases. Unlike the bichromatic wave cases presented in Chapter 5, the input parameters used to run the XBeach model for the irregular wave cases do not require detailed calibration (such as requiring the use of the autocorrelation for calibrating Trep).

The parameters Hrms and Trep are no longer required to be explicitly specified, as they are computed directly from the input JONSWAP spectrum by XBeach, which is defined by the significant wave height, H_{m0}, and the spectral peak period, T_p, already given in Table 2. The parameter, Trepfac, is used, however, to vary the period used by XBeach. With a value of 1, only the peak period, T_p, is used; while with a value of 0, the mean period over the entire spectral range, T_{m01}, is used. Both wave periods are used to determine which is best suited as the representative period in the XBeach simulations.

From experience with the bichromatic wave cases, it was found the lowest possible value of the eps parameter is most beneficial; therefore the value of 0.001 m is used in the bichromatic wave cases is also used for the irregular wave cases. The effect of decreasing the Chezy friction coefficient was previously shown in the bichromatic wave cases to not have a significant effect on the LF wave heights; therefore a single value of 70 was used for all irregular wave cases.

Table 5 Variable Input Parameters for XBeach Irregular Wave Cases

Series	Trepfac [-] (base / test)	gamma [-] (break = 3 / 4)	gamma2 [-] (break = 4)	alpha [-]	eps [m]	C [$m^{0.5}s^{-1}$]
C-1	1 / 0	0.56	0.20	1.4	0.001	70
C-2	1 / 0	0.56	0.20	1.4	0.001	70
C-3	1 / 0	0.56	0.20	1.4	0.001	70
D-1	1 / 0	0.56	0.20	1.4	0.001	70
D-2	1 / 0	0.56	0.20	1.4	0.001	70
D-3	1 / 0	0.56	0.20	1.4	0.001	70

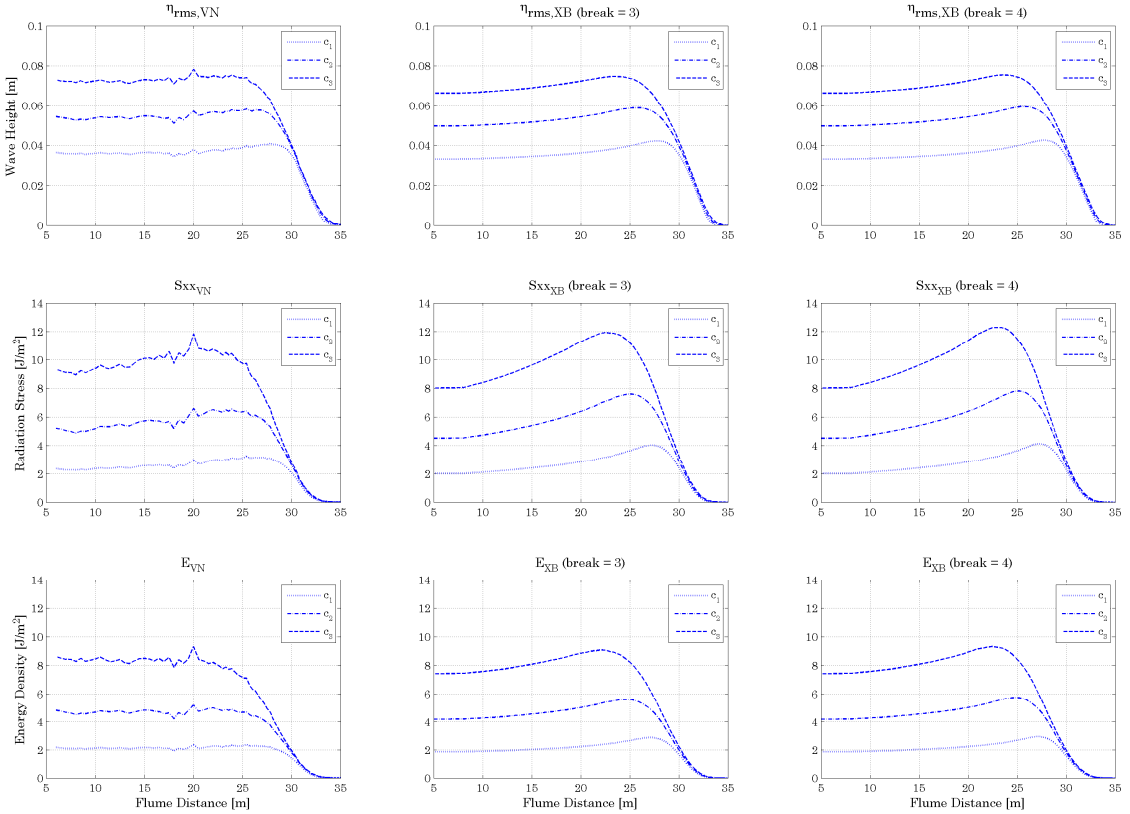

Figure 6.1: Spatial variation of H_{rms} (top row) radiation stress, S_{xx} (middle row), and HF energy, E (bottom row), for van Noorloos data (left column) and XBeach model results for the options break = 3 (centre column) and break = 4 (right column) for series C.

The breaker parameter, gamma, and the breaker coefficient, alpha, are then the only input parameters that are essentially calibrated. The value of gamma was varied until the position of the breakpoint was determined as accurately as possible. A value of 0.56 is used for both the break = 3 and break = 4 options with consistently good results. For the break = 4 option, the second breaker parameter, gamma2, was set at 0.2. The value of alpha used was 1.4 in both breaker options. The model grid used is the original grid (*grid 1*) as results from the bichromatic cases showed that no significant improvement in model results was obtained with a finer grid resolution. In addition, a finer grid in combination with the length of the model run would make comparisons far more computationally intensive than necessary.

6.2 Short Wave Shoaling and Dissipation

6.2.1 Time-Averaged Results

The results of the cross-shore variation in the RMS short wave heights are determined in a similar manner as stated in (5.2) and (5.3). The results shown in Figure 6.1 and Figure 6.2 indicate that XBeach slightly undervalues the RMS wave heights of the irregular short wave groups at the back of the flume, however, it quite accurately shoals towards the observed values around the average breakpoint at 25 m.

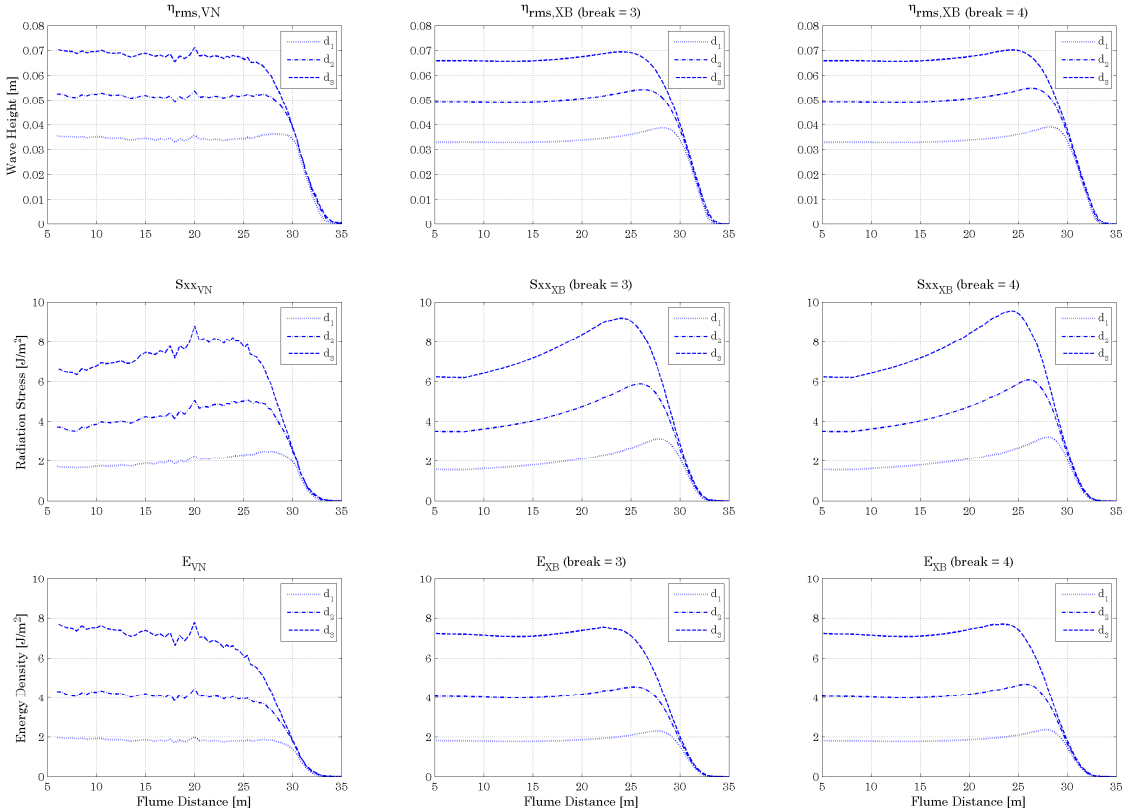

Figure 6.2: Spatial variation of H_{rms} (top row) radiation stress, S_{xx} (middle row), and HF energy, E (bottom row), for van Noorloos data (left column) and XBeach model results for the options break = 3 (centre column) and break = 4 (right column) for series D.

The measured VN data shows that in series C, slight shoaling of the short waves is observed, but clearly not as much as that determined by XBeach. For series D, shoaling is not clearly seen in the measured short waves. In fact, in D-3, the short wave heights appear to slightly decrease towards the average breakpoint[8]. This is most likely due to the changing shape of the waves as they propagate in the flume, as previously discussed in 5.2.1.1.

The wave dissipation results using the two breaker options are very similar, though with break = 4 the decrease in wave height from the breakpoint is slightly sharper. It seems here that the probability of breaking in line with break = 3, which increases as the breaker parameter tends toward gamma, gives the typical smooth reduction in wave heights around the average breakpoint while.

Given the relatively good results for the wave height estimates, it follows that the energy and radiation stress estimates from XBeach are also within good range of the measured data.

[8] Given that the waves are irregular and are therefore composed of many individual waves of varying amplitude and frequency, the breakpoint for each individual wave will be widely spaced, as higher waves break first followed by lower waves. The breaking of the peak wave constituents will mostly be observed and closely corresponds with the average location of the breakpoint.

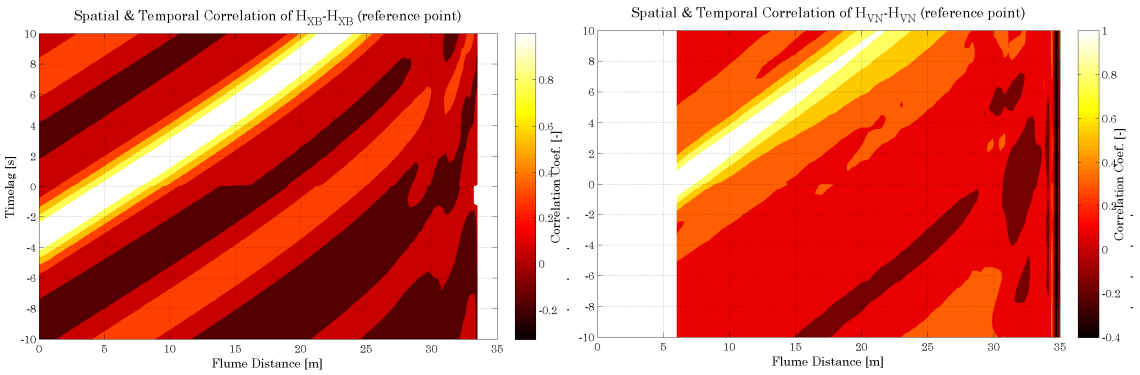

Figure 6.3: Spatial and temporal auto-correlation of H for XBeach break = 4 (left) and for van Noorloos case C-2 data (bottom).

6.2.2 Spatial Evolution of Timeseries

While the time-averaged short wave results are quite good, closer observation of the spatial evolution of the timeseries of the group varying wave height, *H*, shows that XBeach does not represent the changing shape of the wave envelope over space. This is caused by the varying speeds of the individual waves under the envelope which also vary the local amplitude and phase of the envelope. In reality, the rate of change of the amplitude and phase is equivalent to the difference in propagation speeds of the individual waves, but this difference often quite small (for a relatively narrow spectral range) and it is not taken into account in the model since the individual waves are not resolved. Rather, a mean (or representative) value of the group velocity of the individual short waves is used which is derived from the representative wave period.

Figure 6.4 shows the undisturbed translation of H_{XB} (in terms of phase and amplitude) for the XBeach results (bottom plot) whereby, for example, the peak at 215 s is shoaling constantly over distance until breaking 5 s later at 220 s. If we do the same for the measured data[9], H_{VN}, whereby we look at the translation of the peak at 220 s, the amplitude of the peak varies over distance up to 6 s later (at 226 s) due to the amplitudes of varying individual waves moving with differing speeds under the envelope.

This feature is also highlighted in Figure 6.3 where the auto-correlation of *H* is given in space and time. For H_{XB} (left plot), the strongly positive correlation of the timeseries is observed through time and space as the white streak. The similar positive correlation of H_{VN} (right plot) deteriorates over time and space from the reference point at 6 m, though the main trend can still be observed.

Figure 6.5 and Figure 6.6 shows the variation of the groupiness factor, G_f, of the short waves for series C and series D respectively. The groupiness computed from the XBeach break = 3 (centre plots) and break = 4 (right plots) results are similar to each other and to the results from the measured data (left plots) in the shoaling zone. There is, however, a significant loss of groupiness in the XBeach data during wave breaking which is not observed in the measured data.

[9] Of course, given that we are using an irregular wave spectrum, the time series of the XBeach data and the VN measurements cannot be synchronized in time.

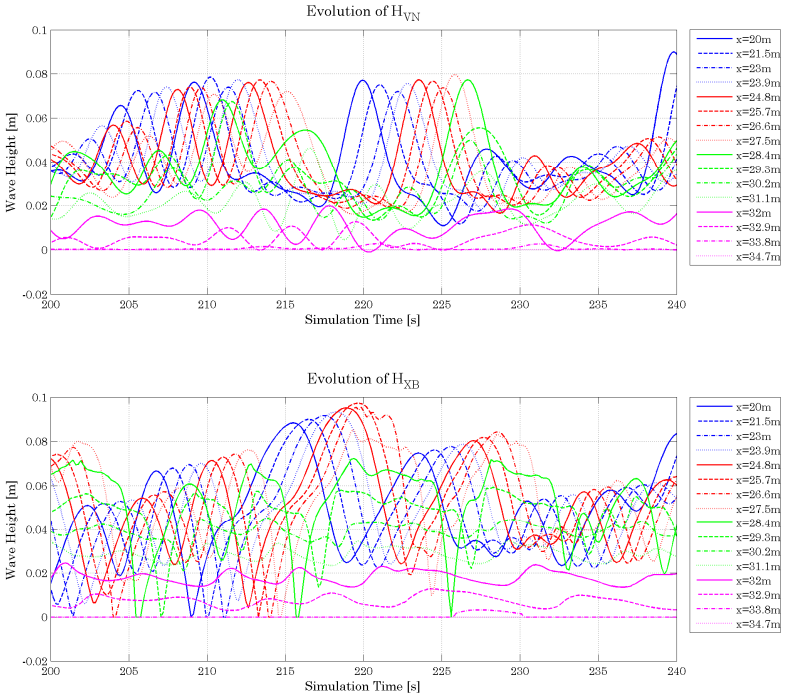

Figure 6.4: Spatial evolution of the group varying short wave height timeseries, *H*, from the end of the shoaling zone (blue lines), to the onset of breaking (red lines), through the latter stages of breaking (green lines), and in shallow water (pink lines) for van Noorloos data (top), XBeach break = 4 data (centre) and XBeach break = 3 data (bottom).

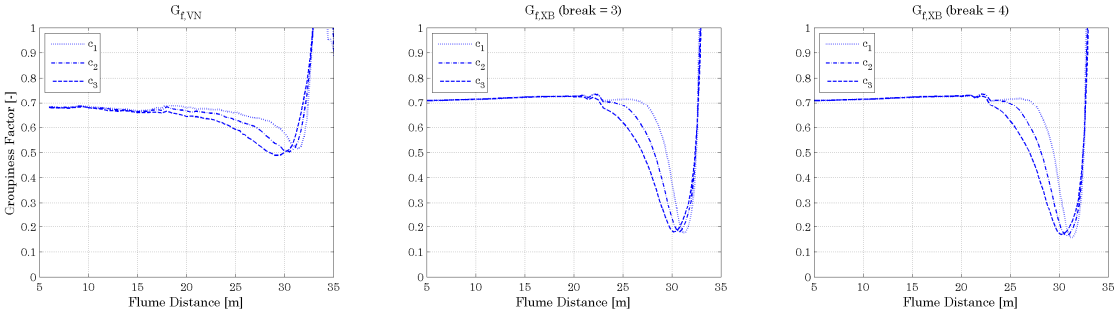

Figure 6.5: Groupiness factor of the group-varying short wave height, *H*, for van Noorloos (left) and XBeach break = 3 (centre) and break = 4 (right) data for series C.

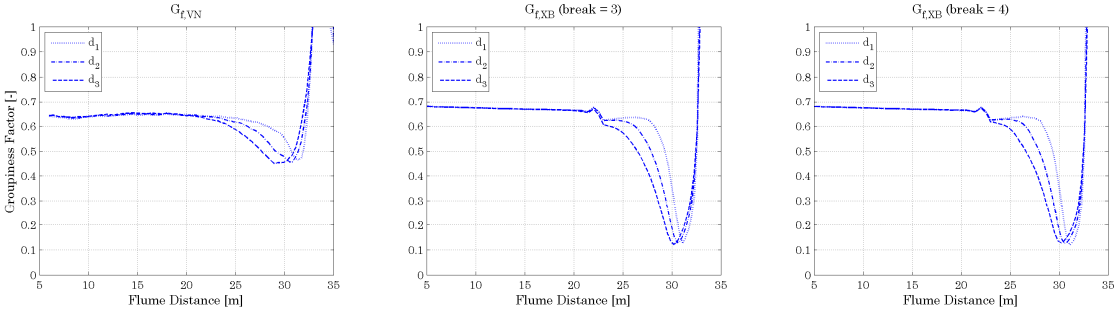

Figure 6.6: Groupiness factor of the group-varying short wave height, *H*, for van Noorloos (left) and XBeach break = 3 (centre) and break = 4 (right) data for series D.

6.2.3 Spatial Evolution of Energy Density Spectrum

Figure 6.7 and Figure 6.9 shows the spatial evolution of the energy density spectrum of the measured surface elevation from the VN experiment for case C-3 and D-3 respectively. The peaks in the (short wave) energy density at 0.5 Hz for case C-3 and 0.65 Hz for case D-3 is clearly shown to progress though the flume up to about 25 m where this energy begins to dissipate with some energy shifted to lower and higher frequencies from the peak frequency. At around 30 m, most, if not all, of the short wave energy density is dissipated, with the peak energy density now concentrated in the LF band. We see also that in the shoaling zone, the short wave spectrum is mostly above 0.3 Hz for case C-3 and for case D-3 the spectrum is mostly above 0.4 Hz. These frequencies are used as the cut-off frequency between HF and LF for series C and series D respectively. The curved energy bands in the LF section of the spectrum are also pointed out by *Battjes et al.* [2004], and are the resulting interference pattern between the IBLF and RFLF waves.

Figure 6.8 and Figure 6.10 shows the spatial evolution of the energy density spectrum of the group-varying wave height, H (left columns), and the LF part of the spectrum below the cut-off frequency, (right columns) for XBeach break = 4 data (top rows) and measured data from the VN experiment (bottom rows) for case C-3 and D-3 respectively. With regard to the energy density spectrum of H, the peak at 0.038 Hz in the measured VN data indicates that this is the peak difference interaction frequency; therefore, most of the energy contribution to the LF waves comes from HF difference interactions within a range of ± 0.038 Hz around the peak HF.

Figure 6.8 and Figure 6.10 shows that the LF wave spectrum of XBeach is well matched in the shoaling and breaking zone with the measured LF spectrum from the VN data. The XBeach model is able to capture the multiple peaks present in the LF spectrum in the breaking zone. In shallow water, a higher LF peak at around 0.1 Hz is amplified first, followed by a lower LF peak at around 0.05 Hz. The higher LF peak is also first to reduce in amplitude at the shoreline, therefore in very shallow water, only the lowest LF peaks exist. This is quite an important observation, as it means that only the lowest frequency waves are able to extend their reach inland, which is why these waves are crucial in accurately determining morphological processes such as dune foot erosion.

Figure 6.11, Figure 6.12 and Figure 6.13 show 2-D plots of the evolution of the energy density spectrum[10] of the measured surface elevation from the VN experiment (red) and of the (LF) surface elevation output from XBeach (blue) in the shoaling, breaking and shallow water zones respectively for case C-3. Figure 6.14, Figure 6.15 and Figure 6.16 show similar 2-D plots for case D-3. These plots give a one-to-one comparison of the LF spectrum of both the measured and modelled datasets.

While the energy density results in shallow water indicate that XBeach accurately estimates the shift of the peak LF to lower values in shallower water, the estimated energy density is slightly greater than what the VN measured data indicates, especially above the shoreline (located at approximately 32 m).

[10] Note that the maximum on the vertical scale changes for each set of plots. Only the results from break = 4 is shown as they are very similar to the results obtained using break = 3.

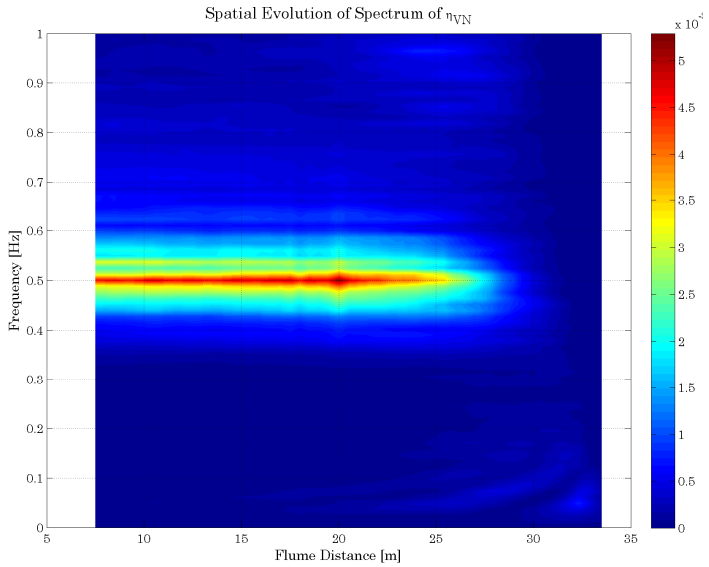

Figure 6.7: Spatial evolution of the energy density spectrum of η from van Noorloos data for case C-3.

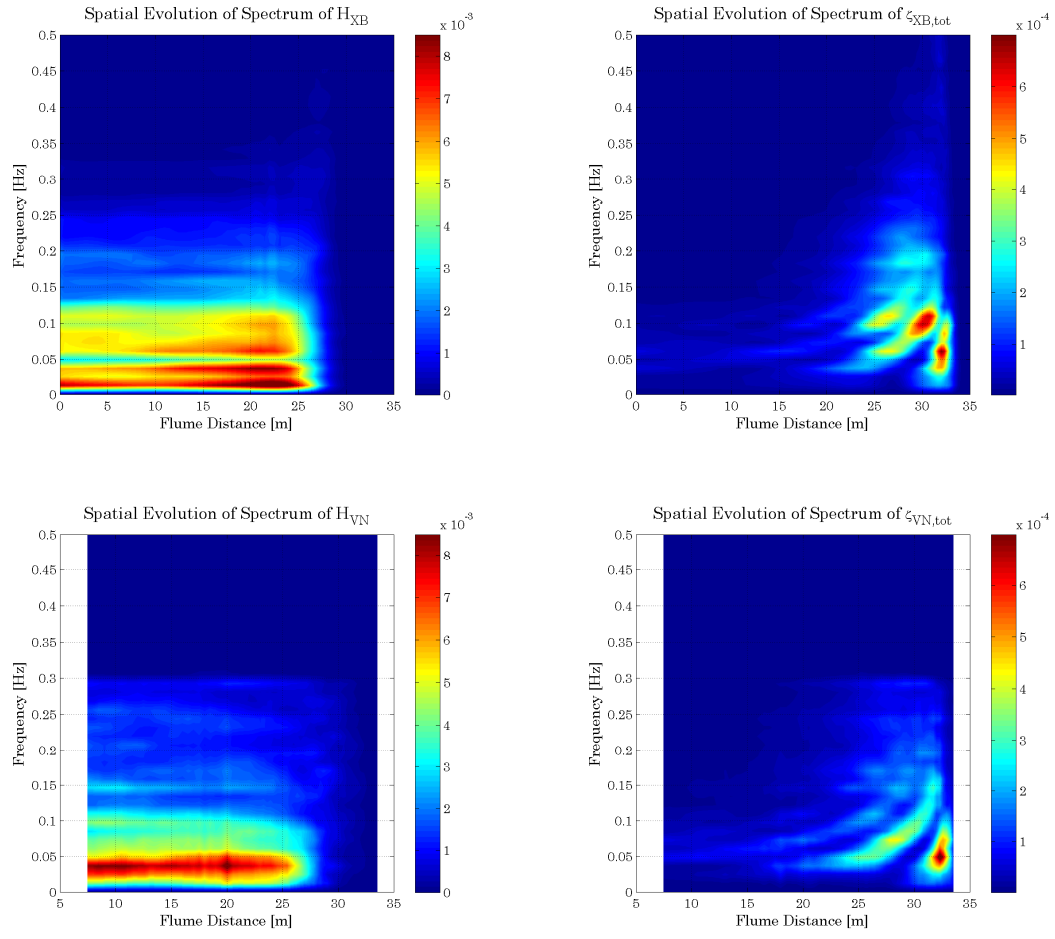

Figure 6.8: Spatial evolution of the energy density spectrum of H (left column) and ζ (right column) for XBeach break = 3 (top row) and van Noorloos (bottom row) data for case C-3.

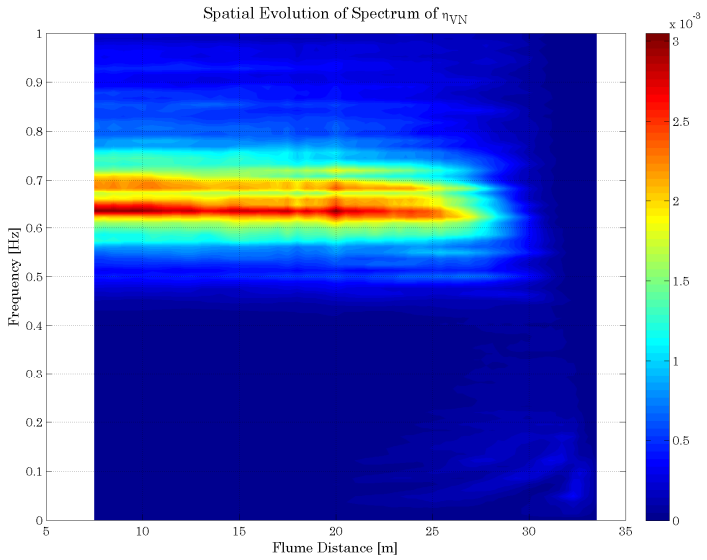

Figure 6.9: Spatial evolution of the energy density spectrum of η from van Noorloos data for case D-3.

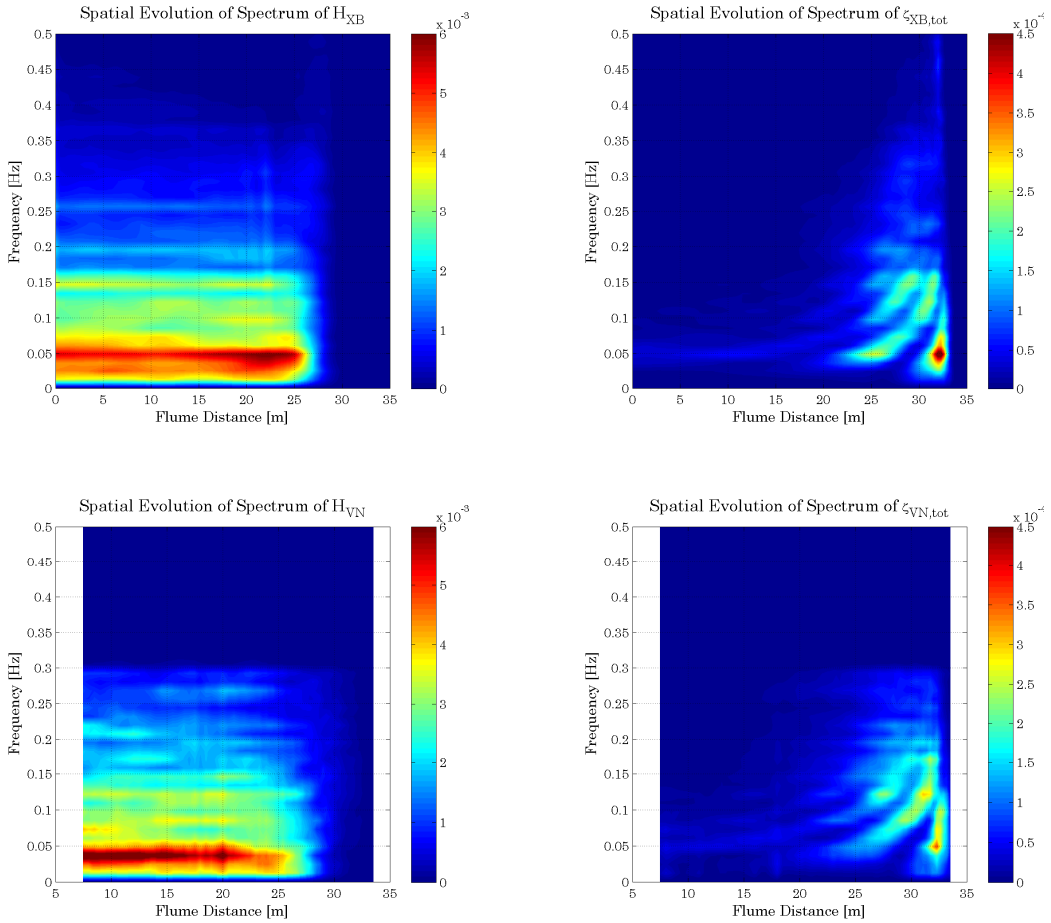

Figure 6.10: Spatial evolution of the energy density spectrum of H (left column) and ζ (right column) for XBeach break = 3 (top row) and van Noorloos (bottom row) data for case D-3.

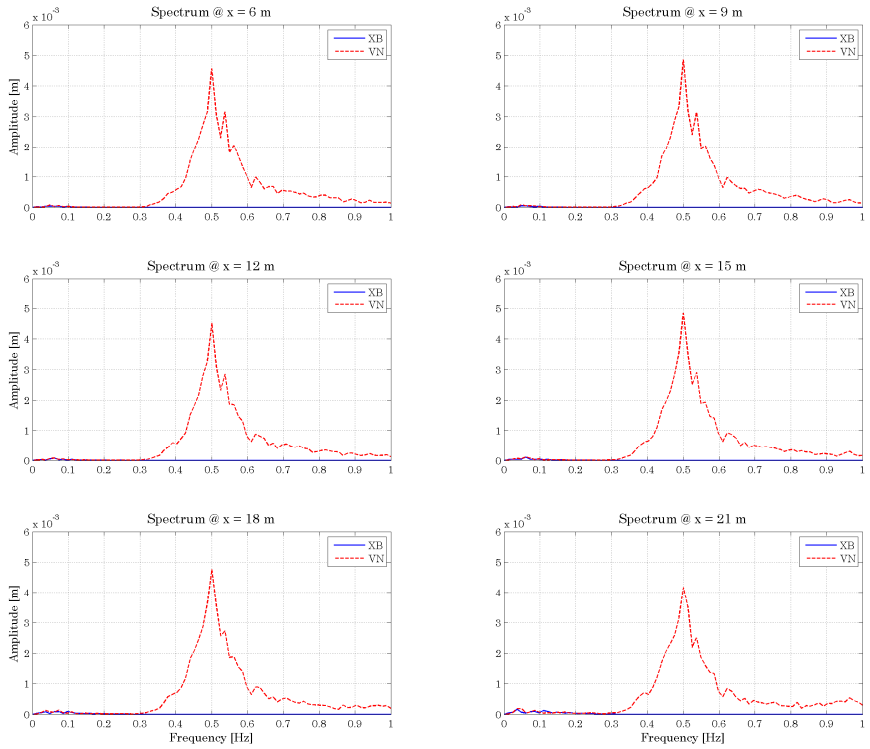

Figure 6.11: 2D energy density spectrum of η for van Noorloos (red lines) and ζ for XBeach (blue lines) in the shoaling zone for break = 4 case C-3.

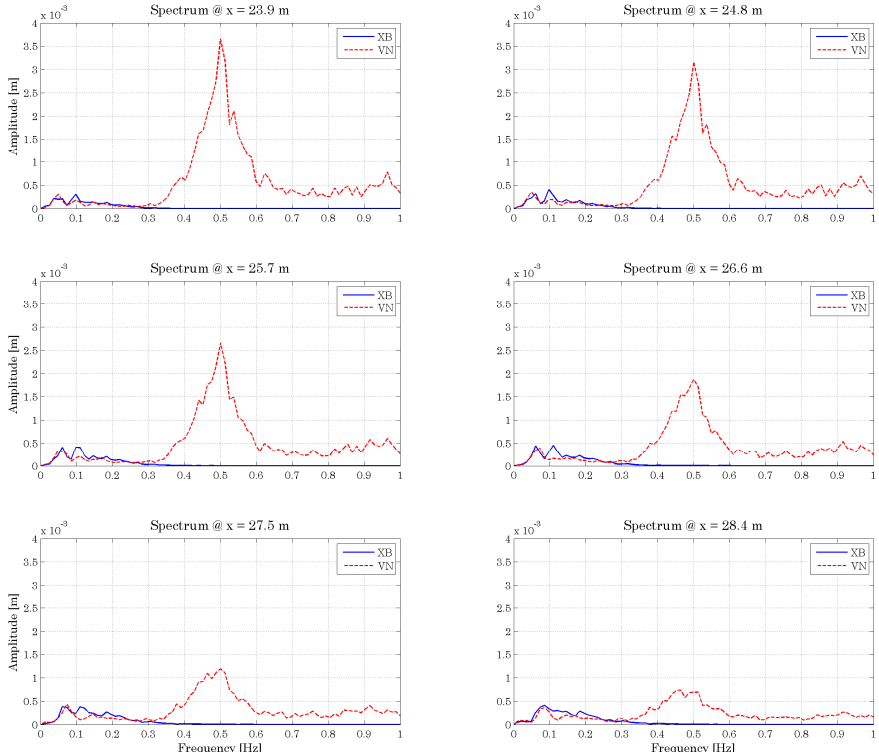

Figure 6.12: 2D energy density spectrum of η for van Noorloos (red lines) and ζ for XBeach (blue lines) in the breaking zone for break = 4 case C-3.

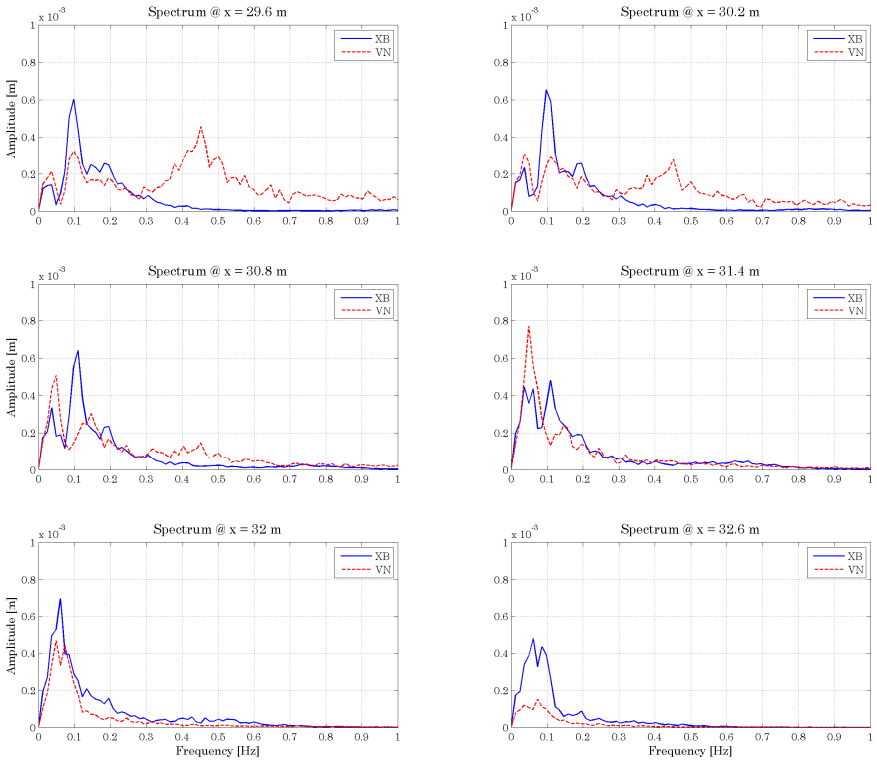

Figure 6.13: 2D energy density spectrum of η for van Noorloos (red lines) and ζ for XBeach (blue lines) in the shallow water zone for break = 4 case C-3.

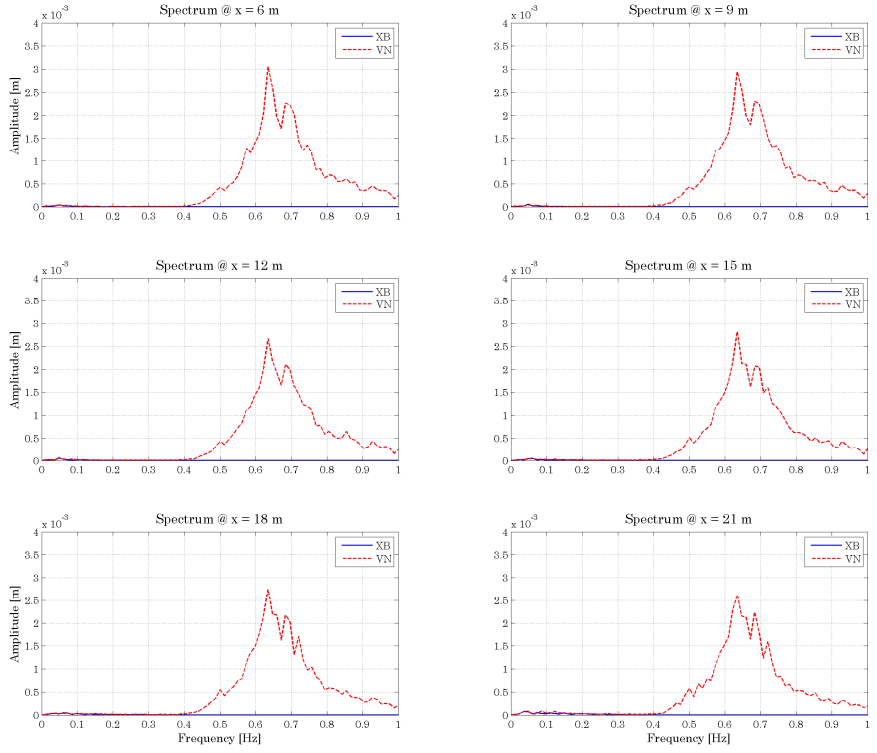

Figure 6.14: 2D energy density spectrum of η for van Noorloos (red lines) and ζ for XBeach (blue lines) in the shoaling zone for break = 4 case D-3.

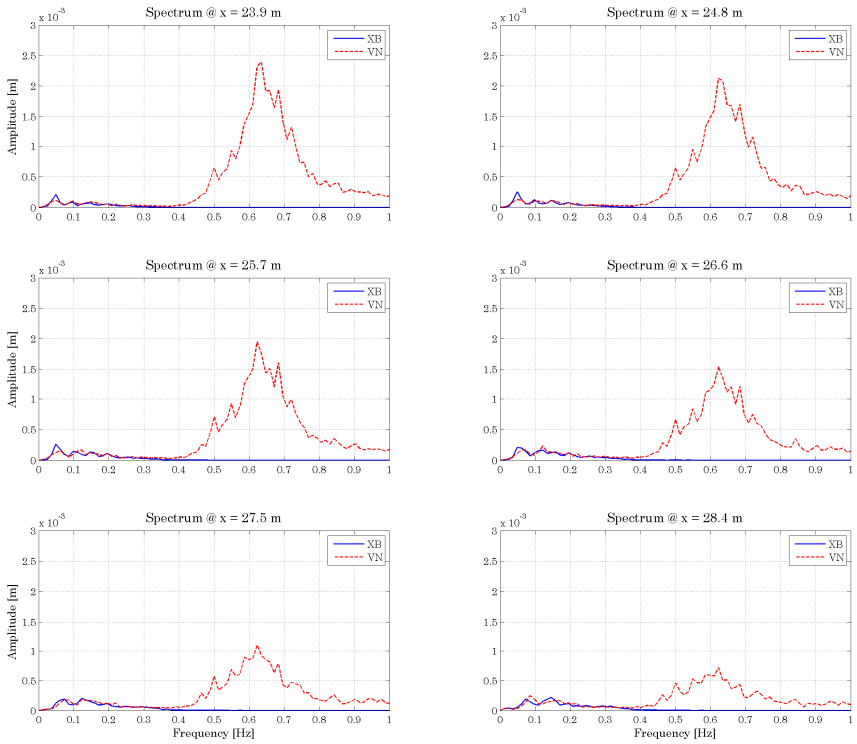

Figure 6.15: 2D energy density spectrum of η for van Noorloos (red lines) and ζ for XBeach (blue lines) in the breaking zone for break = 4 case D-3.

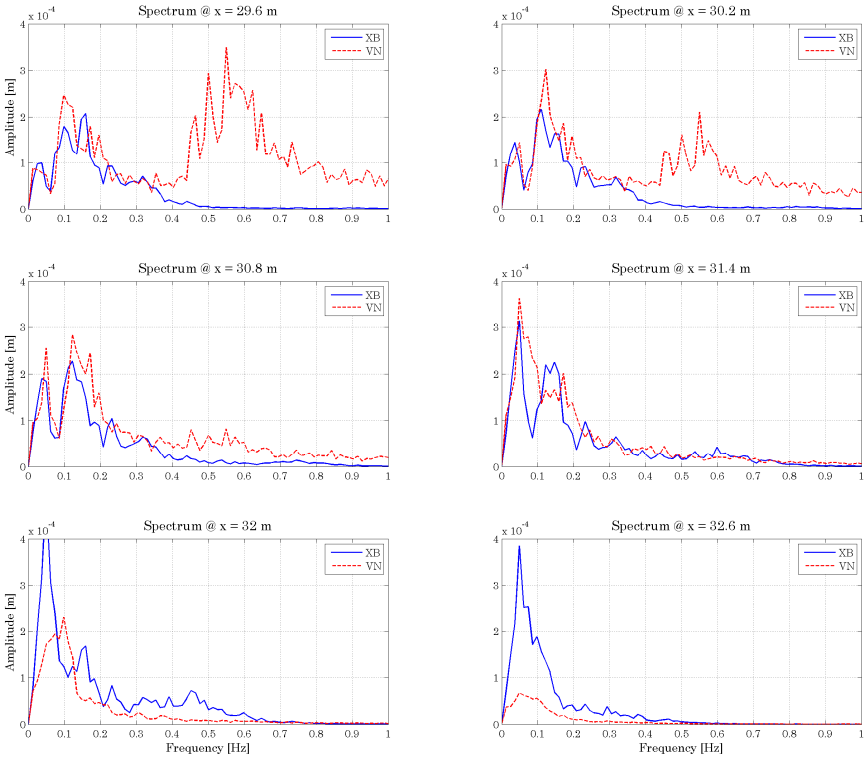

Figure 6.16: 2D energy density spectrum of η for van Noorloos (red lines) and ζ for XBeach (blue lines) in the shallow water zone for break = 4 case D-3.

6.3 Low Frequency Wave Shoaling and Reflection

6.3.1 Time-Averaged Decomposition Results

Figure 6.17 and Figure 6.18 shows the growth of the total LF wave heights towards the shoreline (top rows) and more specifically the IBLF (centre rows) and RFLF (bottom rows) wave heights of the measured VN data (left columns) and the XBeach model results using break = 3 (centre columns) and break = 4 (right columns) for series C and series D respectively.

The results obtained using break = 3 and break = 4 for the XBeach simulations, similar to the short wave results, are very much the same with each other. The RFLF waves are all shown to be predicted quite well by XBeach, however, the total LF wave heights are overestimated in the breaking and shallow water zone. This is primarily a result of the overestimation[11] of the IBLF wave heights by approximately 34% for series C and 20% for series D. The initial shoaling rates of the XBeach IBLF wave heights match the measured data up to the location of the average breakpoint at around 23 m, but instead of levelling off and eventually decreasing, the shoaling of the XBeach IBLF waves continues well into the shallow water zone and up to the shoreline.

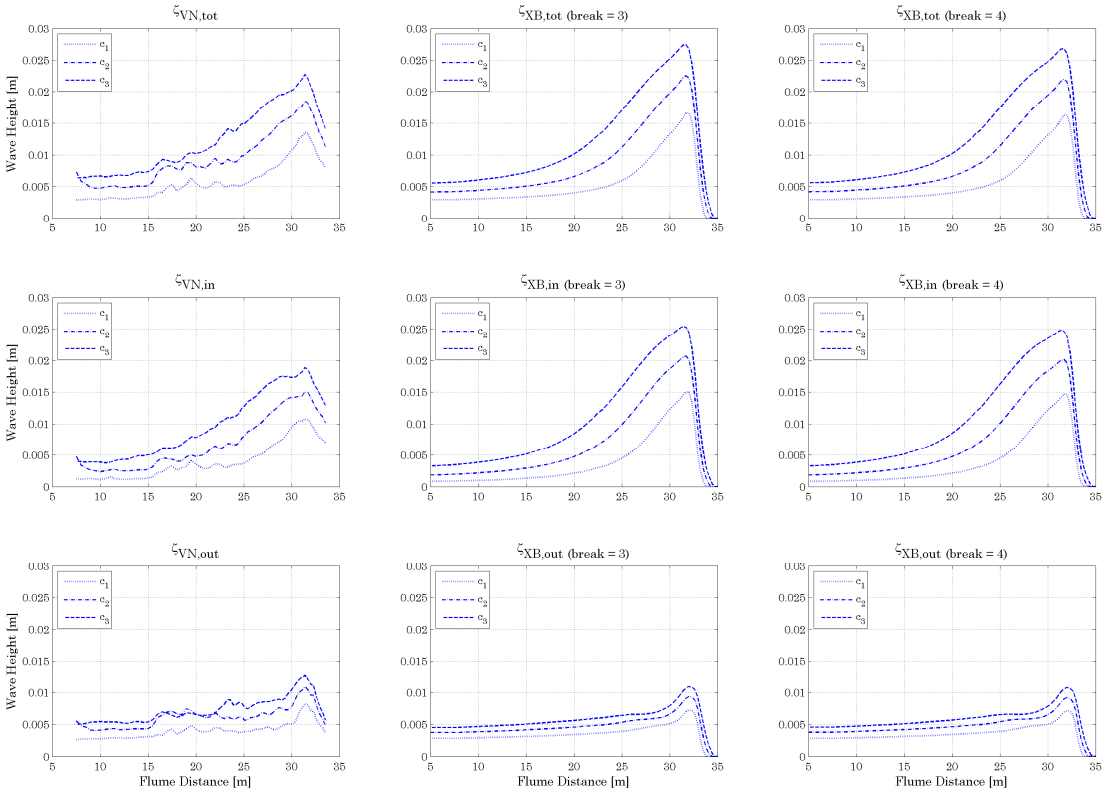

Figure 6.17: Spatial variation of RMS values for the total (top row), inbound (centre row) and reflected (bottom row) LF waves from the van Noorloos (left column) and XBeach break = 3 (centre column) and break = 4 (right column) data for series C. (Trepfac = 1, roller on).

[11] The estimate is taken at the peak value of the wave height for both the VN and XBeach data (at around x = 32 m).

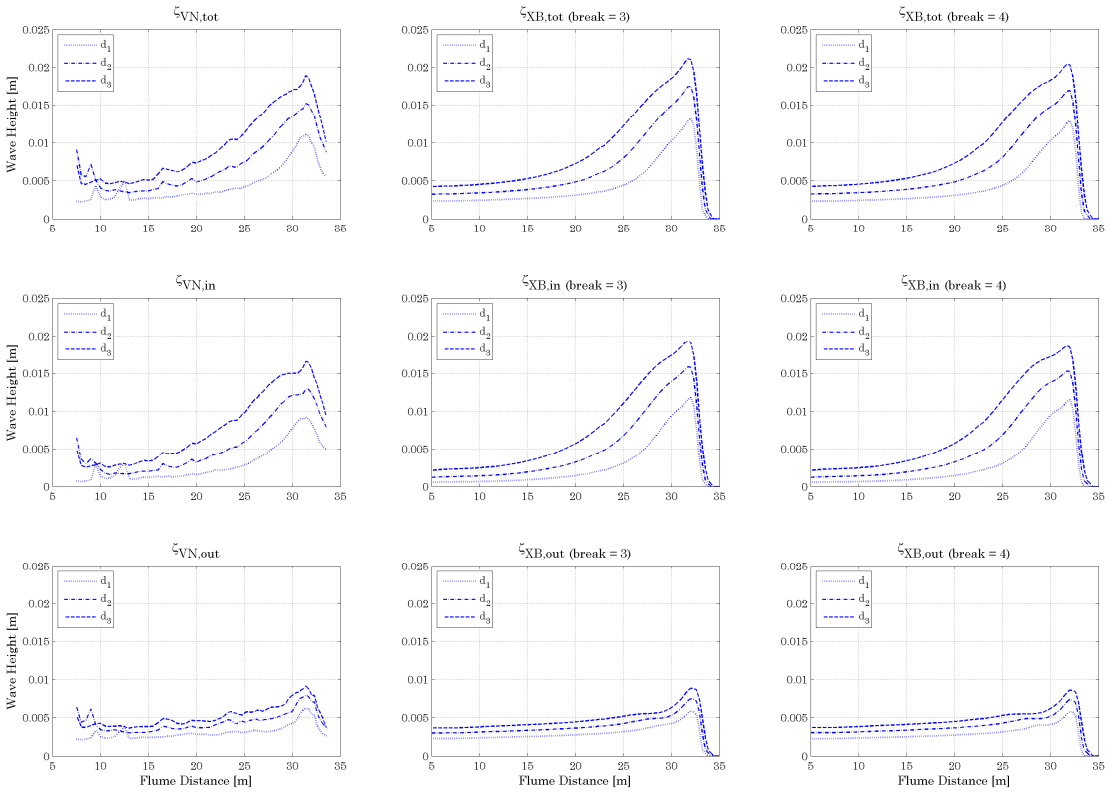

Figure 6.18: Spatial variation of RMS values for the total (top row), inbound (centre row) and reflected (bottom row) LF waves from the van Noorloos (left column) and XBeach break = 3 (centre column) and break = 4 (right column) data for series D. (Trepfac = 1, roller on).

6.3.2 Spatial Evolution of Energy Density Spectrum

Figure 6.19 shows the evolution of the energy density spectrum of the IBLF and RFLF waves for XBeach and VN. Here, it is more clearly shown that the XBeach IBLF wave heights are overestimated in shallow water when compared to the measured VN data. The XBeach RFLF waves are shown to reasonably well estimated in frequency space. Figure 6.19 is representative of the results obtained for the other irregular wave cases.

6.3.3 Effect of Excess Roller Radiation Stress

The overestimation of the IBLF wave in XBeach could be related to the determination of the radiation stresses as a result of the roller dissipation model, which are added to the radiation stress gradients due to the waves. To test this hypothesis, the roller dissipation model was turned off in another set of model runs while keeping the other parameter settings constant. The result, shown in Figure E.7 in Appendix E for series C, does not indicate that the roller radiation stresses is the main cause, as the overestimate is only reduced to approximately 28% from 34%.

6.3.4 Effect of Representative Wave Period

The effect of changing the Trepfac to 0, thereby using the mean spectral period, T_{m01}, is shown in Figure E.8 in Appendix E. Here, the results are very much similar to that obtained when trepfac is set to 1 for which the peak period is used.

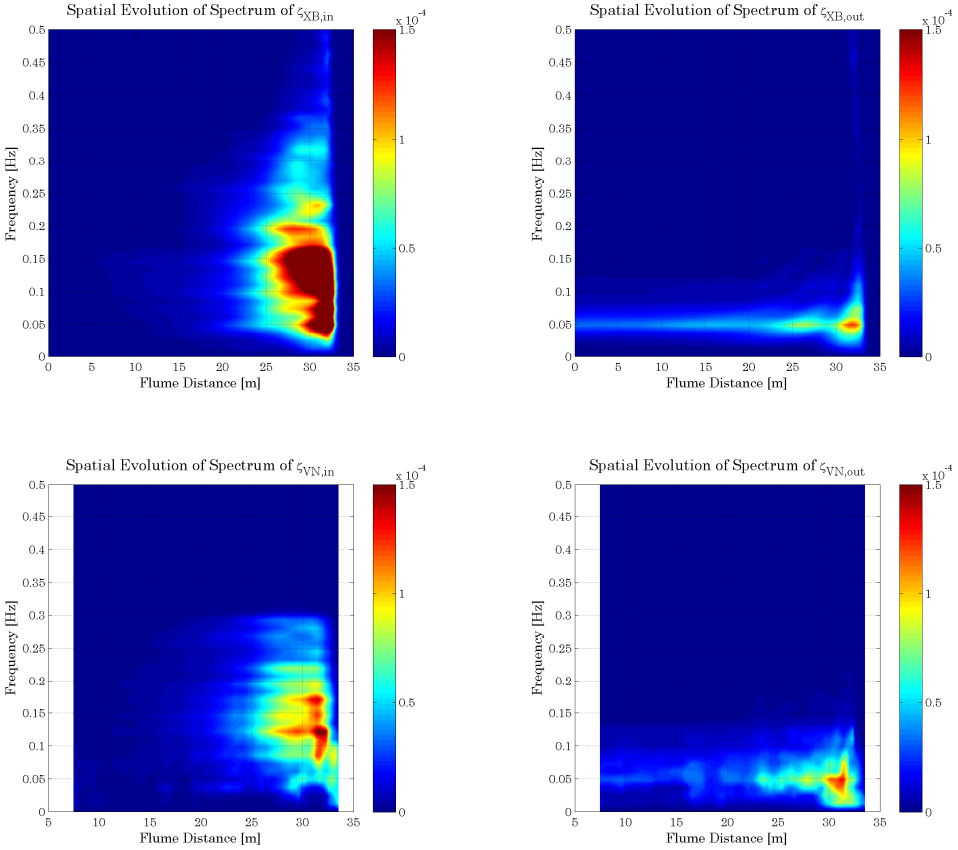

Figure 6.19: Spatial evolution of the energy density spectrum of ζ_{in} (left column) and ζ_{out} (right column) for XBeach break = 3 (top row) and van Noorloos (bottom row) data for case D-3.

6.4 Summary

6.4.1 Short Wave Estimates

The following is a summary of the short wave analysis for irregular waves:

- A standard and common set of model parameters can be used in irregular wave cases for both break = 3 and break = 4 options.
- XBeach gives quite good estimates of the time-averaged short wave parameters (H_{rms}, E and S_{xx})

6.4.2 Low Frequency Wave Estimates

The following is a summary of the LF wave analysis for irregular waves:

- The energy density spectrum of XBeach matches the measured spectrum well in shoaling and breaking zone, but is higher in the shallow water.
- RFLF wave heights are estimated quite well by XBeach, however, the IBLF wave heights are overestimated by approximately 20 – 34% in shallow water.

- The initial rate of shoaling of the XBeach IBLF waves are quite similar to the measured rate of shoaling in the shoaling zone (up to 23 m), however, the fact that the over-estimates occur in the breaking and shallow water zone, indicate that processes in this region are the likely cause.
- The additional radiation stress gradients from the roller model are not the main factor for the overestimates of the XBeach IBLF wave heights. Turning this feature off in the model accounts for only a 6% reduction in the overestimation, when a 25% reduction of the XBeach IBLF wave height is required.
- The results obtained when using T_p and/or T_{m01} as the representative period in XBeach are very similar. Perhaps for a wider spectrum or for a bi-modal spectrum there may be greater differences in the results.

6.4.3 Discussion

6.4.3.1 XBeach Breaker Options

There is very little difference in the results presented above for the irregular wave cases between the two XBeach breaker parameterization options used. It has been shown that `break = 3` is limited in representing short wave breaking for bichromatic waves, as the breaking range obtained is much wider than what was seen in the measurements. With increased bichromatic modulation the value of the breaker parameter decreased. As the irregular waves are also quite highly modulated, the value of `gamma` used is low, but is similar to the recommended values of *Roelvink* [1993]. `break = 3` greatly improves with application to irregular waves, most likely because the values of the breaker parameters chosen represent average wave breaking conditions for the random waves, which in reality, does have a wide breaking range.

The value of `gamma` used with `break = 4` was constant for bichromatic waves, suggesting that it is independent of the modulation of the waves. For the irregular wave cases we had to, however, reduce the value of `alpha` to half the value used for the bichromatic wave cases. This effectively reduced the rate of dissipation during breaking, therefore sustaining breaking over a longer distance. This makes it, in some sense, equivalent to `break = 3`, as dissipation of the wave energy occurs over a wide area.

6.4.3.2 IBLF Overestimation

While the spectral plots of the total LF wave heights appear only show minor overestimates of the energy in the LF spectrum in shallow water, when this is decomposed into incoming and reflected components, the clear overestimation of the IBLF is seen. It is possible that the interference with the RFLF waves makes the total wave heights not that far off from the measurements; however the forcing of the IBLF waves is most likely too great in the model. Wave-current interaction (WCI) may also be an important factor for estimates in shallow water, especially where wave run-up and run-down are concerned, as this can alter the observed velocities in this region. This feature was not enabled in the model runs.

Chapter 7 – Conclusions and Recommendations

7.1 Conclusions

The objective of this study was to validate the hydrodynamic modules of the XBeach model with particular interest in the LF wave estimates in the shoaling and nearshore zone. The experiment of VN has provided invaluable information into the physics of wave propagation and dissipation, and is therefore a very useful test to measure the performance of time-dependent shallow water models like XBeach. The wave action equations prove to remain robust over the various types of wave input while the NSW equations, which form the basis of many models describing fluid flow, show more sensitivity in shallow water where the processes are certainly more complex.

In the experiments of VN, bichromatic waves allows for detailed comparisons based on a very simple, narrow-banded spectrum and we can then analyse the individual wave components that are measured versus model output. The irregular wave cases allow us to observe the performance of the model for a wider band of wave spectra, which is observed most often in nature and is therefore most suited for practical applications of XBeach.

In order to make a fair comparison between the measured and modelled data, XBeach has to be calibrated to optimize a number of input parameters. Some of the seven main input parameters used, which are `Hrms`, `Trep` (which represent the boundary wave height and the period used to transport the wave energy upwind in the model), `gamma`, `gamma2`, `alpha` (used in the wave breaking schematization) `eps` and `C` (used for the flooding-drying schematization and bed shear stress in the NSW equations in the flow module respectively) can be optimized using the auto-correlation function while others are tested based on trial-and-error.

For both bichromatic and irregular wave cases, the short wave heights are fairly well predicted, given the limitations of the assumptions in linear wave theory. In both cases, the shoaling of the short waves in XBeach were slightly overestimated when compared to the measured data, which is believed to be due to inability of the (second generation) wave action equations to model the increasingly non-linear behaviour of the measured waves (skewness and asymmetry) as they shoal and dissipate in the nearshore zone.

The dissipation of wave energy in XBeach was done using two breaker parameterizations – one, *Roelvink* [1993] (keyword: `break = 3`) and a modified version also by *Roelvink* [Pers. Com. 2009] (keyword: `break = 4`). `break = 3` is found to be limited in use when applied to bichromatic waves where the probability function applied to wave breaking constantly dissipates wave energy over a wide area which significantly reduces the variance of the group-varying wave height in the breaking and shallow water zones. The new breaker parameterization, `break = 4`, gives a more realistic determination of the short wave breaking process, imitating the 'breathing pattern' of naturally breaking waves – rising (inhaling) just before and falling (exhaling) just after reaching the maximum value of the breaker parameter. This variability is transported with the propagation speed of the wave further into the shallow water zone, which is also seen in the measurements.

If we were to compare break = 3 and break = 4 to the different methods of LF wave generation due to wave breaking, break = 3 would most resemble the model of *Symonds et al*. [1982], while break = 4 is comparable to the hybrid model of *Schäffer* [1993]. With both breaker models, the initial shoaling rate of the IBLF waves is comparable to the measured data. For bichromatic waves, break = 4 gives the better results for the LF waves is series B (amplitude dependency), but not for series A (frequency dependency). Additionally, break = 4 is able to extend the wave interactions within the LF spectrum further up in the HF range in during wave breaking and in shallow water, similar to what is seen in reality. For irregular waves, both breaker parameterizations perform equally, giving very similar results for similar input parameters. Given that break = 4 is able to represent both the predictable nature of breaking for bichromatic waves as well as the broad range of breaking for irregular waves, it is the preferred breaking parameterization.

XBeach gives remarkably good visualizations of wave run-up, where the LF waves are shown to steepen and surge up the beachface. Despite the fact that in reality the waves have a gentler slope during run-up, the fact that XBeach is capable of qualitatively representing the dynamics of the process is extremely advantageous for determining sediment transport in the swash and overwash zones. Therefore, the most important issues to address in the case of run-up are, first, the over-steepening of the LF wave, and secondly, the maximum limit of run-up which affects the initial point of the phase variation of the RFLF wave.

In general, XBeach has shown that it is capable of modelling both quantitatively and qualitatively the short wave energy flux and LF wave shoaling and reflection quite will without inducing serious errors from the linear simplifications in the wave module. The most important point, however, is that the IBLF waves are, in fact, over-estimated by approximately 20% – 34 % for irregular wave spectra. While other errors, such as those due to discretizations or values of the friction coefficient used, are relatively small (less than 10%), the forcing of the IBLF wave requires particular attention and particularly the frequency dependence of IBLF wave shoaling.

Previous validation studies, for example *McCall* [2008], have already identified that XBeach over-predicts morphological changes in shallow water which lead to the hypothesis that the LF wave estimates in shallow water were too high. This validation has confirmed this observation, as has identified that the IBLF waves are the main cause. In order to improve the estimates of the IBLF waves, we therefore need to look at the forcing terms derived in the short wave module that are applied to the NSW equations in the flow module.

7.2 Recommendations

The over-shoaling of the wave energy and wave height in XBeach should be addressed to better represent the forcing mechanism (radiation stress gradients) of the short waves on the IBLF waves. As such, accounting for additional sources of energy dissipation, such as by means of friction, can (slightly) improve the output of the short wave module. This is especially useful if XBeach is used to model situations where the roughness of the bottom topography can have a significant influence on the short waves, such as areas where there is vegetation such as seagrass on the seabed, or if the bottom is rocky. The overall effect, however, may not be enough to significantly improve the LF wave results, but this is still a consideration.

To (partially) account for the non-linearities which often cause the shape of the wave (and wave spectrum) to change in the nearshore zone, the incorporation of a third generation spectral model (or other similar method) which is capable of (approximately) estimating the energy transfer

from the main HF part of the wave spectrum to higher and lower harmonics as the short waves propagate over space can aid in reducing the energy of the main HF band. This means that the short wave energy is not fully conserved in areas where non-linearities are pronounced, leading to energy 'dissipation' from the core HF waves and thus reduced forcing on the LF waves.

Another alternative would be to employ a non-hydrostatic approach, which would essentially combine HF waves in the flow module, thereby abandoning the short wave module. This has been previously investigated by *Smit* [2008]. In his conclusions, *Smit* ascertains that this would allow for direct modelling of short waves in the nearshore (in addition to the LF waves). This alternative requires the model to be extended to a 3-D (layered) computational grid to obtain improved results, which comes with the disadvantage of increasing computational time.

The over-steepening of the LF wave run-up can be investigated to determine whether the addition of a vertical component to the momentum balance equation or an alternative numerical scheme to limit the steepness of the wavefront can improve the current results. Also, given that the eps parameter in XBeach can lead to instabilities in the LF wave results, further investigation into the flooding-drying schematization, which uses this parameter, should be done.

Finally, accounting for wave current interaction in the model might also aid in improving the model results in the nearshore.

7.3 Further Research

In this study, we focused on a 2-dimentional uni-directional approach for the validation of XBeach, however, in the modelling of real-life situations, XBeach would also include the longshore dimension. Therefore, it is important to also validate the model against such a scenario (in a controlled manner) since, in this case, additional phenomena such as refraction, directional spreading and the formation of longshore currents are also very important factors influencing morphological change.

Further study to quantify the significance of the errors induced by using a linear scheme to determine the short wave forcing should be done. This should also be a precursor to justify further improvements to the model. To do so would require that the model should be further validated against prototype field cases.

References

AIRY, G.B., (1845), Tides and waves, Encyclopaedia Metropolitana, London, Scientific Department, pp. 241-396

ARCILLA, A.S., J.A. Roelvink, B.A. O'Connor, A. Reniers and J.A. Jimenéz, (1994), The Delta flume '93 experiment, Coastal Dynamics 1994, Am. Soc. Civ. Eng.

BATTJES, J.A., (1974), Surf similarity, Proc. of 14th Int. Conf. Coastal Eng., Copenhagen, Am. Soc. Civ. Eng., pp. 467-479

BATTJES, J.A., H.J. Bakkenes, T.T. Janssen, and A.R. van Dongeren, (2004), Shoaling of subharmonic gravity waves, J. Geophys. Res., 109, C02009, doi:10.1029/ 2003JC001863.

BATTJES, J.A. and J.P.F.M. Janssen, (1978), Energy loss and set-up due to breaking in random waves, Proc. 16th Int. Coastal Eng. Conf., Hamburg, vol. 1: 569-587.

BOUSSINESQ, J., (1872), Théorie des ondes et des remous qui se propagent le long d'un canal rectangulaire horizontal, en communiquant au liquide contenu dans ce canal des vitesses sensiblement pareilles de la surface au fond, J. Math. Pures Appl., Série 2, vol. 17 : 55-108.

CARRIER, G.F. and H.P. Greenspan, (1958), Water waves of finite amplitude on a sloping beach, J. Fluid Mech., vol. 4: 97-109.

DEIGAARD, R., (1993), A note on the three dimensional shear stress distribution in a surf zone, Coastal Eng., 20, pp. 157-171

HALLER, M.C. and R.A. Dalrymple, (1995), Looking for wave groups in the surf zone, Proc. Coastal Dynamics 1995.

HASSELMANN K., T.P. Barnett, E. Bouws, H. Carlson, D.E. Cartwright, K. Enke, J.A. Ewing, H. Gienapp, D.E. Hasselmann, P. Kruseman, A. Meerburg, P. Müller, D.J. Olbers, K. Richter, W. Sell and H. Walden, (1973), Measurements of wind-wave growth and swell decay during the Joint North Sea Wave Project (JONSWAP), Deutsch. Hydrogr. Z., Suppl., A8, 12, 95 pp.

HOLTHUIJSEN, L.H., N. Booij and T.H.C. Herbers, (1989), A prediction model for stationary short-crested waves in shallow water with ambient currents, Coastal Eng., vol. 13: 23-54

HOLTHUIJSEN, L.H., (2008), Waves in oceanic and coastal waters, Camb. Univ. Press,

JANSSEN, T.T., J.A. Battjes, and A.R. van Dongeren, (2003), Long waves induced by short-wave groups over a sloping bottom, J. Geophys. Res., 108(C8), 3252, doi:10.1029/2002JC001515.

JANSSEN, T.T., (2006), Nonlinear surface waves over topography, Ph.D. Thesis, Delft University of Technology, the Netherlands.

JIMENÉZ, J.A., A.H. Sallenger and L. Fauver, (2006), Sediment transport and barrier island changes during massive overwash events, Int. Conf. Coastal Eng. 2006, San Diego.

JOHANSSON, M., (1999), The hilbert transform, M.Sc. Thesis, Växjö University, Sweden.

KORTEWEG, D.J. and G. de Vries, (1895), On the change of form of long waves advancing in a rectangular canal, and a new type of long stationary waves, Phil. Mag., Series 5, vol. 39: 422-443.

LIST, J.H., (1992), A model for the generation of two dimensional surf beat, J. Geophys. Res., vol. 212: 61-79

LIST, J.H., (2002), Breakpoint-forced and bound long waves in the nearshore: A model comparison, Prec. Int. Conf. Coastal Eng. 2002.

LONGUET-HIGGINS, M.S., and R.W. Stewart, (1962), Radiation stress and mass transport in gravity waves, with application to 'surf beats', J. Fluid Mech.

MCCALL, R.T., (2008), The longshore dimension in dune overwash modelling, M.Sc. Thesis, Delft University of Technology, the Netherlands.

MCCALL, R.T., J.S.M. van Thiel de Vries, N.G. Plant, A.R. van Dongeren, J.A. Roelvink, D.M. Thompson, A.J.H.M. Reniers, (2009), Two-dimensional time dependent hurricane overwash and erosion modeling at Santa Rosa island, Submitted to Coastal Eng.

MUNK, W.H., (1949), Surf beats, Trans. Amer. Geophys. Un., vol. 30: 849-54.

PHILLIPS, O.M., (1977), The dynamics of the upper ocean, 2nd edition, Camb. Univ. Press, New York.

PIERSON, W.J. and L. Moskowitz, (1964), A proposed spectral form for fully developed wind seas based on the similarity theory of S.A. Kitaigorodskii, J. Geophys. Res., vol. 69, 24, 5181-5190.

ROELVINK, J.A., (1993), Surf beat and its effect on cross-shore profiles, Ph.D. Thesis, Delft University of Technology, the Netherlands.

ROELVINK, J.A., (Pers. Com. 2009), Note on new breaker parameterization for XBeach, Unpublished.

ROELVINK, J.A., A. Reniers, A.R. van Dongeren, J.S.M. van Thiel de Vries, J. Lecinsky, (2008), R. McCall, XBeach Model Description and Manual, Report, Unesco-IHE, Deltares and Delft University of Technology.

RUESSINK, B.G., (1998), Infragravity waves in a dissipative multiple bar system, Ph.D. Thesis, University of Utrecht.

SCHÄFFER, H.A. and I.A. Svendsen, (1988), Surf beat generation on a mild slope beach, Proc. of the 21st International Conference on Coastal Engineering, pp. 1058-1072, Am. Soc. Of Civ. Eng.

SCHÄFFER, H.A., (1993), Infragravity waves induced by short-wave groups, J. Fluid Mech., vol. 247: 551-588.

SMIT, P.B., (2008), Non-hydrostatic modeling of large scale tsunamis, M.Sc. Thesis, Delft University of Technology, the Netherlands.

STEENHAUER, K., (2003), Numerical modelling of surfbeat, M.Sc. Thesis, Delft University of Technology, the Netherlands.

STELLING, G.S. and S.P.A. Duinmeijer, (2003), A staggered conservative scheme for every Froude number in rapidly varied shallow water flows, Int. J. Num. Meth. in Fluids, vol. 43: 1329-1354.

STOKES, G.G., (1847), On the theory of oscillatory waves, Trans. Camb. Phil.. Soc., vol. 8: 441-455

SVENDSEN, I.A., (1984), Wave heights and set-up in a surf zone, Coastal Eng., vol. 8:303-329

SVENDSEN, I.A., (2005), Introduction to nearshore hydrodynamics, World Scientific, Advanced Series on Ocean Engineering – Volume 24.

SYMONDS, G., D.A. Huntley and A.J. Bowen, (1982), Two-dimensional surf beat. Long wave generation by a varying breakpoint, J. Geophys. Res., vol. 80: 492-498.

TUCKER, M.J., (1950), Surf beats: sea waves of 1 to 5 minutes' period, Proc. Roy. Soc. A, 202, 565-73.

URSELL, F., (1953), The long wave paradox, Proc. Camb. Phil. Soc., vol. 49: 685-694

VAN DER MOLEN, W., P. Monárdez Santander and A. van Dongeren, (2004), Modeling of infragravity waves and moored ship motions in Tomakomai Port, Prec. Harbor Long Wave 2004.

VAN DONGEREN, A.R., F.E. Sancho, I.A. Svendsen and U. Putrevu, (1994), SHORECIRC: A quasi-3D nearshore model, 24th Int. Conf. Coastal Eng., Am. Soc. Civ. Eng.

VAN DONGEREN, A.R., A. Reniers, J. Battjes, and I. Svendsen, (2003), Numerical modeling of infragravity wave response during DELILAH, J. Geophys. Res. 108(C9), 3288, doi:10.1029/2002JC001332.

VAN DONGEREN, A.R., J.A. Battjes, T.T. Janssen, J.C. van Noorloos, K. Steenhauer, G. Steenbergen and A. Reniers, (2007), Shoaling and shoreline dissipation of low-frequency waves, J. Geophys. Res., 112, C02011, doi:10.1029/2006 JC003701.

VAN GROESEN, E., Andonowati and E. Soewono, (1999), Nonlinear effects in bichromatic surface waves, Proc. Estonian Acad. Sci. Phys. Math.

VAN THIEL DE VRIES, J.S.M., J. van de Graaf, B. Raubenheimer, A. Reniers and M.J.F. Stive, (2006), Modelling inner surf hydrodynamics during storm surges, Proc. 30th Int. Conf. Coastal Eng., Am. Soc. Civ. Eng.

VAN NOORLOOS, J.C., (2003), Energy transfer between short wave groups and bound long waves on a plane slope, M.Sc. Thesis, Delft University of Technology, the Netherlands.

WALSTRA, D.J., J.A. Roelvink and J. Groeneweg, (2000), 3D calculation of wave-driven cross-shore currents, Proc. 27th Int. Conf. Coastal Eng., Sydney

WATSON, G., and D. Howell Peregrine, (2002), Low frequency waves in the surf zone, Prec. Int. Conf. Coastal Eng. 2002, Am. Soc. Civ. Eng.

Figures

Tables

Appendix A – Use of FFT for Filtering and Spectra

A.1 The Fast Fourier Transform

The fast Fourier transform (FFT) is a mathematical procedure which quickly computes the discrete Fourier Transform (DFT) and can be used to discretize the frequency components of a timeseries signal, $\hat{\eta}(t)$, given as

$$\hat{\eta}(t) = \sum_{i=1}^{N} a_i \cos(2\pi f_i t + a_i). \tag{A.1}$$

The timeseries can be rewritten using trigonometric identities as

$$\hat{\eta}(t) = \sum_{i=1}^{N} A_i \cos(2\pi f_i t) + B_i \sin(2\pi f_i t), \tag{A.2}$$

$$\text{where} \quad A_i = \frac{2}{D}\int_D \hat{\eta}(t)\cos(2\pi f_i t)\, dt \tag{A.3}$$

$$\text{and} \quad B_i = \frac{2}{D}\int_D \hat{\eta}(t)\sin(2\pi f_i t)\, dt \tag{A.4}$$

are the Fourier coefficients. The discrete amplitude and phase for each frequency component, i, of the signal is given in terms of the Fourier coefficients as

$$a_i = \sqrt{A_i^2 + B_i^2} \tag{A.5}$$

$$\text{and } \psi_i = -\frac{B_i}{A_i}. \tag{A.6}$$

The FFT procedure is most efficient when the number of data points, N, of the timeseries is an integer multiple of 2, such that $N = 2^p$ and where $p = 1,2,3\ldots\infty$. For a given value of p, and sampling frequency, f_s, the duration, D, of the signal timeseries is then

$$D = \frac{2^p}{f_s}. \tag{A.7}$$

The lowest resolvable frequency (or basic frequency) of the signal timeseries, f_0, is given as

$$f_0 = \frac{1}{D}. \tag{A.8}$$

This therefore implies that in order to sufficiently describe LF motions (given the finite length of the timeseries), the duration of the timeseries should be chosen such that the lowest desirable frequency is able to be discretized.

In MATLAB®, the FFT of the original signal timeseries produces the complex value amplitude and phase per integer multiple, i, of the basic frequency component. The frequency range is two-sided, however, for practical purposes, only the positive half of the frequency range is used and the ensemble mean (given at 0 Hz) is reduced to zero by de-trending the timeseries beforehand. The length of i is equal to N and the maximum value is determined by the Nyquist frequency, f_{nyq}, where

$$f_{nyq} = \frac{f_s}{2}. \tag{A.9}$$

This therefore implies that the sampling frequency should be chosen such that the desired upper limit of frequency range is able to be discretized.

A.2 Low and High Pass Filtering

Filtering is important in distinguishing between low frequency (LF) and high frequency components (HF) of a (measured) timeseries signal, $\hat{\eta}(t)$. The filtering process can easily be done in frequency space by using the fast Fourier transform (FFT) of the signal. A cut-off frequency, f_{cut}, is specified, above which is considered to be the HF domain and below which is the LF domain. The value of f_{cut} should be chosen appropriately to best represent the divide between HF and LF. The Fourier transform of the LF and HF components, $\zeta(t)$ and $\eta(t)$ respectively, is given as

$$F_{\zeta(t)}(f_i) = \begin{cases} 0 & \text{for } f_i \le 0 \\ F_{\hat{\eta}(t)}(f_i) & \text{for } 0 < f_i \le f_{cut} \\ 0 & \text{for } f_{cut} < f_i \le f_{nyq} \end{cases} \tag{A.10}$$

$$\text{and } F_{\eta(t)}(f_i) = \begin{cases} 0 & \text{for } f_i \le 0 \\ 0 & \text{for } 0 < f_i \le f_{cut} \\ F_{\hat{\eta}(t)}(f_i) & \text{for } f_{cut} < f_i \le f_{nyq} \end{cases} \tag{A.11}$$

where F represents the FFT. From (A.10) and (A.11) we then obtain $\zeta(t)$ and $\eta(t)$ using the inverse Fourier transform (IFFT) as

$$\zeta(t) = F^{-1}\left[F_{\zeta(t)}(f_i)\right] \tag{A.12}$$

$$\text{and } \eta(t) = F^{-1}\left[F_{\eta(t)}(f_i)\right]. \tag{A.13}$$

where F^{-1} represents the IFFT. It then follows that

$$F_{\hat{\eta}(t)}(f_i) = \begin{cases} 0 & \text{for } f_i \le 0 \\ F_{\zeta(t)}(f_i) & \text{for } 0 < f_i \le f_{cut} \\ F_{\eta(t)}(f_i) & \text{for } f_{cut} < f_i \le f_{nyq} \end{cases} \tag{A.14}$$

$$\text{and } \hat{\eta}(t) = \eta(t) + \zeta(t) \tag{A.15}$$

where the mean value of the signal timeseries is $= 0$.

A.3 Wave Spectra

The amplitude and phase spectrum of a timeseries signal, $\hat{\eta}(t)$, can be determined directly from the magnitude and argument of the FFT of the timeseries, given by (A.5) and (A.6) respectively. We are (normally) more interested in the amplitudes of the frequency components in the timeseries, therefore for each *i*, the *amplitude spectrum* is given as

$$a_i = \frac{2}{N}\left|F_{\hat{\eta}(t)}(f_i)\right| \tag{A.16}$$

The *variance density spectrum* is determined based on (2.41) as

$$E(f_i) = \frac{1}{2}\frac{1}{f_0}\frac{2}{N}\left|F_{\hat{\eta}(t)}(f_i)\right|^2 \tag{A.17}$$

The *energy density spectrum* is obtained by simply multiplying the variance density estimates by the factor $\frac{1}{8}\rho g$. This is sometimes treated as a constant and ignored, therefore the variance density spectrum is (incorrectly) referred to as the *energy variance density spectrum*.

The estimate is of the variance density in (A.17) is based on only one realization of a finite length timeseries, which results in a raw or grassy-looking spectrum as the variance density is estimated with only one amplitude per frequency. This gives approximately a 100% error in the variance estimates. To counteract this, the expected value of the variance can be found by dividing the timeseries into a number of (overlapping) parts for which the variance density is computed and averaged. This has the disadvantage of reducing the actual duration of the truncated timeseries, therefore the basic frequency is increased and the frequency discretization is reduced.

For the bichromatic wave cases, the amplitude spectrum is used as we are only looking at two primary wave sources and the non-linear waves generated from their resonance. For irregular wave cases, the energy variance density calculations are presented (which is not multiplied by the $\frac{1}{8}\rho g$ factor). In order to improve the variance density estimates, the timeseries is divided into 16 parts with 50% overlap, resulting in an average over 31 points. In both the bichromatic and irregular wave cases, the sampling frequency is decreased from 25 Hz to 6.25 Hz in order to facilitate faster computational times for FFT procedures. The parameters used for each series is given in Table 1. The parameters of the truncated series C and series D are shown as C' and D'.

Table 1 FFT Parameters used for Bichromatic and Irregular Wave Timeseries

Series	f_s **[Hz]**	p **[-]**	N **[-]**	D **[s]**	f_0 **[Hz]**	f_{nyq} **[Hz]**	f_{cut} **[Hz]**
A	6.25	11	2048	327.52	0.00305	3.125	$2 \times f_b$
B	6.25	11	2048	327.52	0.00305	3.125	$2 \times f_b$
C	6.25	15	8192	1310.56	0.00076	3.125	0.3
C'	6.25	9	512	81.76	0.01223	3.125	0.3
D	6.25	15	8192	1310.56	0.00076	3.125	0.4
D'	6.25	9	512	81.76	0.01223	3.125	0.4

Appendix B Envelope Detection

The envelope of the maxima and minima of a (HF) timeseries, η, is required to determine the group-varying wave height of the timeseries, H, and also other related parameters such as the groupiness and energy density of the waves. In addition, information from the phase of the amplitude envelope can be used to determine the speed of the wave groups. There are two common methods used to determine the envelope of a timeseries. The first is essentially based on the use of the Hilbert Transform and the second based on squaring the timeseries. Both methods are applied to synthetic data and compared in order to select the most suitable method to apply further to measured data. Depending on the type of timeseries, additional steps may need to be taken, namely scaling, to accurately capture the envelope. The author wishes to point out that the scaling procedure used to obtain envelopes for measured timeseries employ *empirical estimates*. The results, however, have been found to be acceptable for the purposes of this thesis.

B.1 The Hilbert Transform Method

A real function, $x(t)$, and its Hilbert transform, $\hat{x}(t)$, are related to each other in such a way that when both are combined they create a so-called strong analytic signal. This analytical signal in the time domain can be written in terms of the (HF) timeseries, $\eta(t)$,as

$$z(t) = \eta(t) + \mathrm{i}\hat{\eta}(t) \tag{B.1}$$

The Hilbert transform is a $\pm \pi/2$ phase shift of $\eta(t)$, such that cosines become sines and vice versa. The Hilbert transform is defined mathematically for all t as

$$\hat{\eta}(t) = \frac{1}{\pi} P \int_{-\infty}^{\infty} \frac{f(\tau)}{t-\tau} d\tau \tag{B.2}$$

when the integral exists and where the P in front of the integral denotes the Cauchy principal value integral which expands the class of functions for which (B.2) exists. The Hilbert transform can, however, be quickly performed in the frequency domain by programs such as MATLAB® using FFT routines to create the phase shift of $\eta(t)$. This FFT is done according to the following relationship between $z(t)$ and $\eta(t)$

$$F_{z(t)}(f) = \begin{cases} F_{\eta(t)} & \text{for } f = 0 \\ 2F_{\eta(t)}(f) & \text{for } f > 0 \\ 0 & \text{for } f < 0 \end{cases} \tag{B.3}$$

The IFFT yields the analytic signal such that

$$z(t) = F^{-1}\left[F_{z(t)}(f)\right] \tag{B.4}$$

and the amplitude envelope is determined as

$$A(t) = \left|z(t)\right| = \sqrt{\eta^2(t) + \hat{\eta}^2(t)}\,. \tag{B.5}$$

According to (B.5) $A(t)$ is a positive function which fits the upper envelope of η, ($A_{top}(t)$). The bottom envelope, $A_{bot}(t)$, is found by similarly applying the Hilbert transform procedure to an inverted η timeseries, whereby positive values become negative and vice versa. The group-varying wave height, $H(t)$, is determined from the envelope as

$$H(t) = A_{top}(t) - A_{bot}(t)\,. \tag{B.6}$$

B.2 The Amplitude Square Method

The Amplitude Square method can be used to determine the envelope of the measured timeseries by squaring the input signal and subsequently filtering the result. This method essentially uses the timeseries to demodulate itself by squaring it, which causes much of the energy to shift to higher frequencies, hence requiring a low-pass filter to detect the envelope (using the discrete FFT method discussed in Appendix A). In order to maintain the correct balance of energy after filtering, a gain is placed on the input signal (typically around a factor 2) and the square root of the signal is taken to reverse the scaling distortion caused by initially squaring the signal. The process is given as

$$A(t) = F^{-1}_{\zeta(t)}\left[\sqrt{\left(\mu\cdot\eta(t)\right)^2}\right] \tag{B.7}$$

where μ is the gain placed on the signal. This method determines the upper envelope of the input timeseries; however, it is assumed that the bottom envelope is a mirror image of the top envelope about the zero (still water) level. Therefore, the group-varying wave height is determined as

$$H(t) = A_{top}(t) - A_{bot}(t) = 2\cdot A_{top}(t) \tag{B.8}$$

B.3 Application to Synthetic Timeseries

Figure B.1 shows the result of applying the Hilbert Transform (HT) method to a synthetic bichromatic timeseries, of linear waves, $\eta^{[1]}(t)$, for different modulations, δ. Here, it is shown that for linear waves the HT method exactly determines the amplitude envelope of the wave groups, and thus the group-varying wave height, H. Figure B.2 shows the amplitude spectrum of $\eta^{[1]}(t)$ (blue lines) and also of a second order bichromatic timeseries, $\eta^{[2]}(t)$, (red lines) which is computed using the same primary wave components as $\eta^{[1]}(t)$. Both spectra have similar first-order amplitudes of 0.05 m and 0.03 m respectively (δ = 0.6) and, for $\eta^{[2]}(t)$, the second-order (Stokes correction) waves are also shown to occur at twice the value of the primary frequencies.

Figure B.3 shows the amplitude spectrum of the group-varying wave height, H, obtained from the application of the Amplitude Square (AS) method (left plot) and the HT method (right plot) to both $\eta^{[1]}(t)$ and $\eta^{[2]}(t)$ *without filtering the result*. In this figure, the spectrum obtained from the

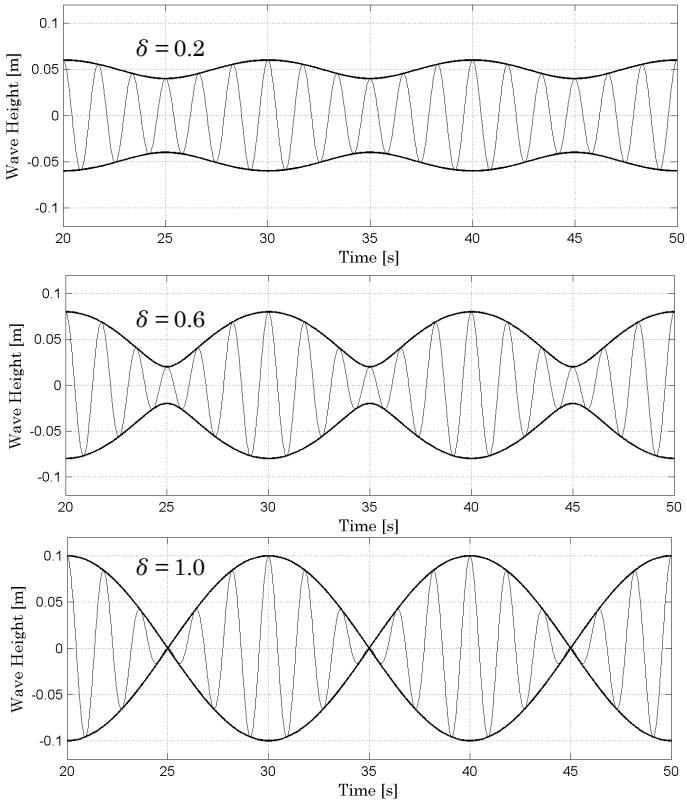

Figure B.1 Comparison of amplitude envelopes of synthetic linear bichromatic timeseries for varying modulation, $\delta = 0.2$ (top), $\delta = 0.6$ (centre) and $\delta = 1.0$ (bottom).

AS method clearly has an (infinite) number of higher (super-)harmonics at integer multiples of the difference frequency, f_b, (0.05 Hz), which extends beyond the 1.0 Hz limit shown on the x-axis. Higher harmonics can be also be seen for the HT method, however, only the first four (in the case of linear waves) or first 8 (in the case of second order waves) exist, with no further super-harmonics (hence a finite number of super-harmonics).

Since the HT method has already been shown to correctly determine the envelope for linear waves, the super-harmonics above the fourth harmonic obtained from the AS method (in this case) has to be ignored, as they do not constitute meaningful contribution to the amplitude envelope. This therefore gives an indication of the value of the cut-off frequency, f_{cut}, to use if applying the FFT filter in the AS method.

In general, it is preferred to use the HT method over the AS method for several reasons. These are, when using the amplitude square method:

1. There is *always* a need to filter the envelope, which is sensitive to the value of f_{cut}.
2. The gain, μ, used in (B.7) has to be calibrated to fit the data.
3. The bottom envelope cannot be directly determined.
4. There are erroneous results for values around and below unity (in this case the square root of the timeseries may be taken).

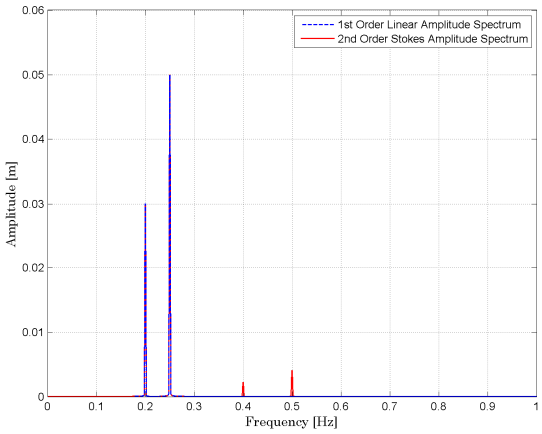

Figure B.2 Amplitude spectrum of a synthetic linear (blue) and second order (red) bichromatic timeseries (with modulation, $\delta = 0.6$).

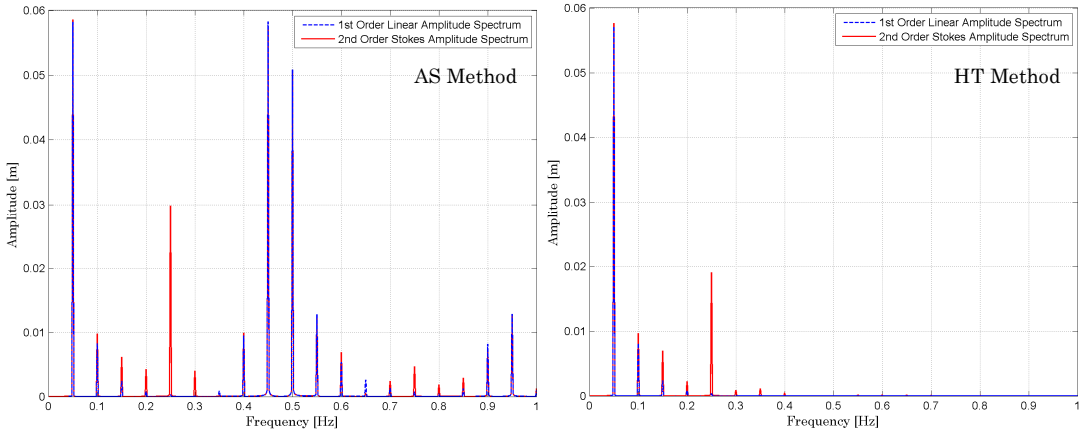

Figure B.3 Amplitude spectrum of the group-varying wave height, H, of a synthetic linear (blue lines) and second order (red lines) bichromatic timeseries determined using the Amplitude Square (left plot) and the Hilbert Transform methods (right plot) without any filtering.

Despite the preference of using the HT method over the AS method, there are still limitations in its use. These limitations present themselves when non-linearities are present in the timeseries. As shown in Figure B.3, the timeseries of H (obtained from a non-linear bichromatic timeseries) includes the effects of a number of super-harmonics. Figure B.4 shows the resulting envelope when the HT method is applied to the non-linear waves (left plot). Here, it is shown that the top and bottom envelopes, $A_{top}(t)$ and $A_{bot}(t)$ respectively, are influenced by the higher harmonics.

While this is not necessarily incorrect, for practical purposes, such creating an energy input timeseries for XBeach model runs, smoothening is desired. By low pass filtering $A_{top}(t)$ and $A_{bot}(t)$ of $\eta^{[2]}(t)$, the HF parts of the signal, $A_{hi}(t)$, is discarded and the resultant amplitude envelope is given as the LF part of the signal, $A_{lo}(t)$. The result of this operation is also shown in Figure B.4 (right plot). Here, it is shown that $A_{lo}(t)$ follows the group structure of $\eta^{[2]}(t)$ more smoothly.

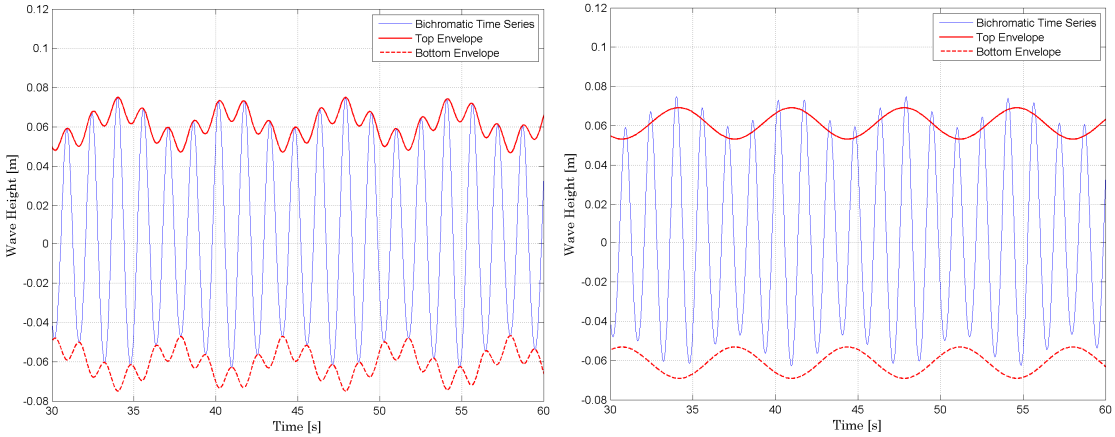

Figure B.4 The result of the Hilbert transform method using a synthetic timeseries of second order waves (left) and subsequent low pass filtering of the envelope (right).

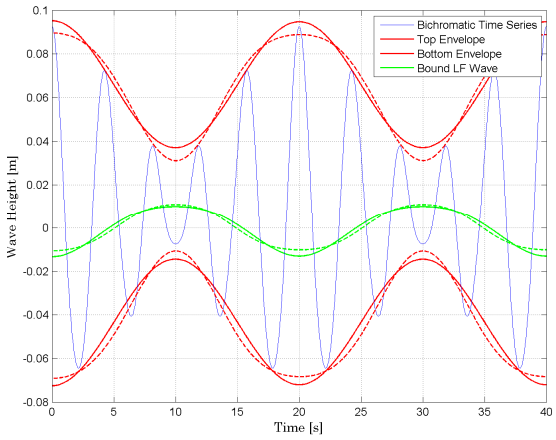

Figure B.5 The upper and lower amplitude envelopes (red) of a second-order synthetic timeseries (blue) and the corresponding bound wave (green) determined using the filtered Hilbert transform including the first two (solid lines) and first three (dashed lines) harmonics.

The value of f_{cut} used will give different results for the envelope, however taking f_{cut} such that the first three harmonics of the HT are included gives the best estimate of the envelope than, say, when the first two are taken, as shown in Figure B.5.

In the right plot of Figure B.4 there is clearly a visual shift of the envelope below its 'ideal' level. This is due to the addition of the second order Stokes correction, given in (2.16), to the linear component, which causes the originally linear timeseries to be shifted upwards relative to the zero level by the amplitude of the second order contribution.

In order to obtain an ideal visual fit of $A_{top}(t)$ and $A_{bot}(t)$ to $\eta^{[2]}(t)$, we can perform an upward translation of the envelopes. This translation is equivalent to the total amplitude of the second-order contribution to $\eta^{[2]}(t)$ which can be estimated, assuming uniform, Rayleigh distributed waves, as

$$a_{A_{hi}} = \frac{H_{rms,A_{hi}(t)}}{2} = \sqrt{2}\sigma_{A_{hi}(t)}\,. \tag{B.9}$$

Adding this constant to $A_{lo}(t)$ of $A_{top}(t)$ and $A_{bot}(t)$ respectively, we get the resultant

$$A_{res}(t) = a_{A_{hi}(t)} + A_{lo}(t) \tag{B.10}$$

The application of (B.10) is shown in Figure B.5, in which it is observed that it approximately determines the correct position of the envelope relative to the second-order waves. If we were to use a different approach whereby we subtract the amplitude of the non-linearities from $\eta^{[2]}(t)$, the position of $A_{top}(t)$ and $A_{bot}(t)$ obtained from the filtered HT will also give a similar visual fit, albeit at a lower vertical position relative to the zero level. Hence, the vertical position of the filtered HT envelope is not affected by the non-linearities in $\eta^{[2]}(t)$.

The method of correcting the position of the envelope is only applicable to non-linear waves simply because the translation is based on the amplitude of the non-linearities present in the timeseries signal, which for the case of linear waves is equal to zero.

B.4 Application to Measured Timeseries

As shown in section B.3 above, the process translating the filtered HT to obtain the upper and lower envelope of nonlinear waves gives accurate results. In reality, however, waves deform when entering shallow water as the non-linearities present in the waves (which most likely goes beyond second-order) increase and symmetry is not maintained over the entire shoaling and breaking zone. Wave skewness and asymmetry influences the HT amplitude envelope.

Figure B.6 below shows examples of the (HF) timeseries $\eta(t)$ from some of wave gauges in the VN experiment located in the shoaling (top row), breaking (middle row) and shallow water (29 bottom row) zones, and also the corresponding upper and lower amplitude envelopes, $A_{top}(t)$ and $A_{bot}(t)$ respectively. The waves in the shoaling zone are shown to be regular, second-order waves, but in the breaking zone, the peakedness of the non-linearities increase and the waves become skewed. In the shallow water zone, the waves are less skewed and more asymmetric.

It is clear from Figure B.6 that in the breaking and shallow water zones, $A_{top}(t)$ should contain more variability while the bottom envelope, $A_{bot}(t)$, is relatively flat and should contain very little variability. While $A_{top}(t)$ and $A_{bot}(t)$ is shown to represent the envelopes of $\eta(t)$ quite well in the shoaling zone, in the breaking zone, $A_{top}(t)$ is not fully capturing the variability of the peaks, and in the shallow water zone $A_{bot}(t)$ contains too much variability. The method to determine the envelope then requires an additional step – that of scaling[1].

We then introduce a scaling factor, $C_f(x)$, the function of which is to relatively increase the variance of the top envelope while simultaneously decreasing the variance of the bottom envelope

[1] It is important to note that the subsequent attempts to properly scale the amplitude envelope is empirical and is therefore only recommended for use with the VN data.

in order to obtain correct values of H (and by extension, the wave energy density) in time (t) and space (x) such that

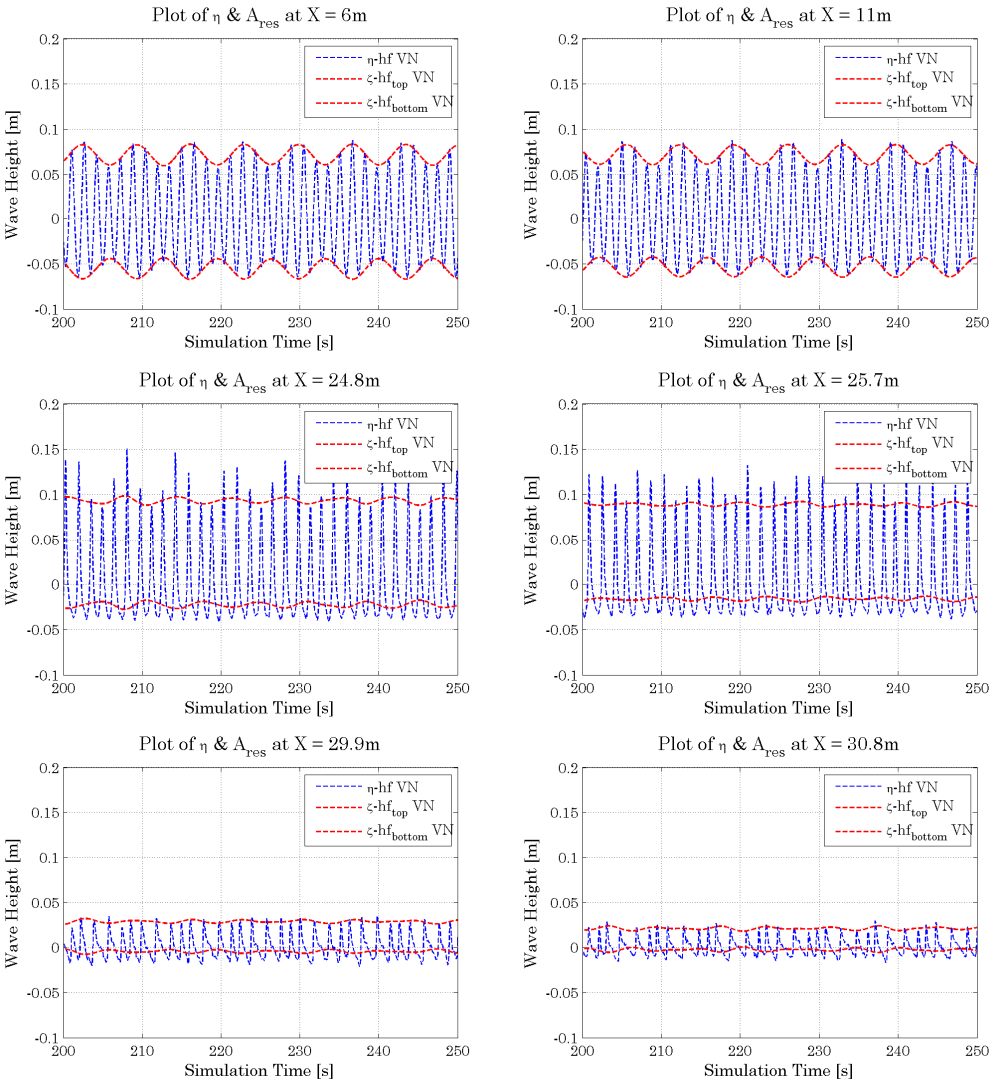

Figure B.6: The result of using the filtered Hilbert transform to obtain $A_{res,top,VN}$ and $A_{res,bot,VN}$ for point locations in the shoaling zone (top row), breaking zone (middle row) and shallow water zone (bottom row) for case A-2.

$$H(t,x) = \left[C_f(x) \cdot A_{top}(t,x)\right] - \left[C_f^{-1}(x) \cdot A_{bot}(t,x)\right]. \tag{B.11}$$

According to (B.11), the reduction of $A_{bot}(t,x)$ is less than the increase in $A_{top}(t,x)$, and subsequently (B.11) will the increase the variability of H (and thus the energy) than when it is originally determined using (B.6).

The difficulty in this step is the fact that the $C_f(x)$ varies with cross-shore location. Since it is found to be highly dependent on the skewness and asymmetry of the waves, we can assume that an initial estimate of $C_f(x)$ is given by the ratio of the wave height of the envelope obtained directly from the HT, $A(t,x)$ (which includes the super-harmonic components) and the wave

height of the filtered LF component, $A_{lo}(t,x)$ with which we eventually use to define the resultant envelope $A_{res}(t,x)$ as given in (B.10). This is given as

$$C_f = \frac{H_{A(t,x)}}{H_{A_{lo}(t,x)}}. \tag{B.12}$$

The cross-shore variance of (B.12) is shown in Figure B.7 below (red lines) for case A-2 of the VN data. Here it is shown that $C_f(x)$ has values as high as 17 in the breaking zone. When (B.12) is applied in combination with (B.11) to the measured VN data, very good agreement between $A_{top}(t,x)$, $A_{bot}(t,x)$ and the measured data, $\hat{\eta}(t)$, is obtained in the shoaling zone, but in the breaking and the shallow water zones the variance is far out of the range of $\hat{\eta}(t)$ because of the excessively high values of C_f in these regions. A different approach is therefore needed in which lower values of $C_f(x)$ are obtained in the breaking zone.

In the next approach, the temporal group steepness, S_t, proposed by *Haller* and *Dalrymple* [1995] as

$$S_t = \frac{\sigma_{A_{res}(t)}}{gT_g^2} \tag{B.13}$$

where $T_g = \sqrt{\frac{m_{0,\hat{\eta}(t)}}{m_{2,\hat{\eta}(t)}}}$ (B.14)

is the spectral estimate of the mean group period, is used as the base function of $C_f(x)$. This is assuming that as the waves approach breaking, they tend to steepen, which is in some way related to the increasing skewness of the waves. Calculating S_t over the cross-shore profile and scaling the result to best fit the values of $C_f(x)$ initially determined by (B.12) in the shoaling zone, a new $C_f(x)$ is determined according to

$$C_f = (a \cdot S_t)^b \tag{B.15}$$

where a and b are 'curve fitting parameters' given in Table (for the bichromatic wave cases).

Table 7 Curve Fitting Parameters for Amplitude Envelope Scaling Factor

Series	***a***	***b***
A-1	3500	0.66
A-2	3400	0.66
A-3	3300	0.66
A-4	3200	0.66
B-2	3400	0.66
B-3	2500	0.75
B-4	1800	0.90
B-5	1100	1.00

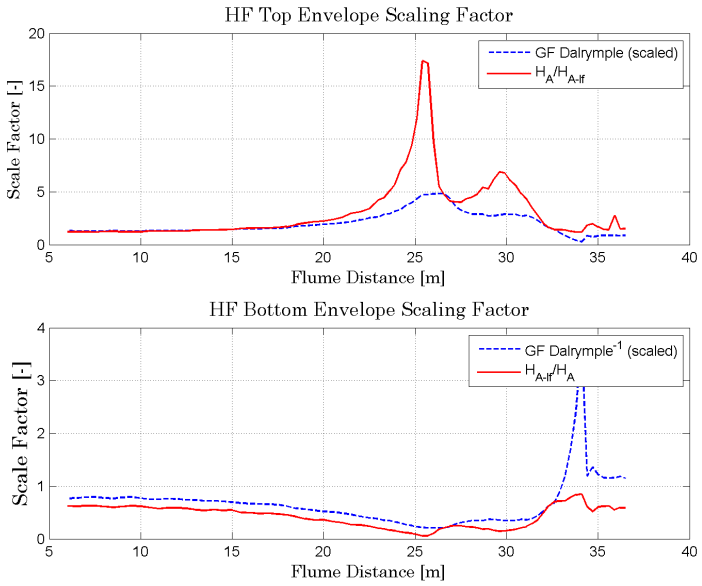

Figure B.7: Amplitude envelope scaling factor, C_f, determined by the ratio of $H[A(t,x)]/H[A_{lo}(t,x)]$ (solid, red lines) and as a function of the temporal group steepness, S_t (dashed, blue lines) for data from van Noorloos case A-2.

The cross-shore variation of this new scaling parameter is also shown in Figure B.7 (blue lines). Here it is seen that $C_f(x)$ obtained from (B.15) is similar in value to $C_f(x)$ obtained from (B.12) the shoaling zone, but is far reduced in the breaking zone, with the maximum value around 5.

The results obtained for scaling $A_{top}(t)$ and $A_{bot}(t)$ using the definition of $C_f(x)$ according to (B.15) in combination with (B.11) is shown in Figure B.8 below. Very good estimates of $A_{top}(t)$ and $A_{bot}(t)$ are obtained in the shoaling zone. In the breaking zone $A_{top}(t)$ captures most the variability of the peaks while $A_{bot}(t)$ is flattened. In the shallow water zone, where symmetry is restored, the envelopes are estimated very well. The values of H determined from (B.11) is used to calculate the cross-shore variance of the RMS wave height of $\eta(t)$ according to

$$H_{rms} = \sqrt{\overline{H^2}} \tag{B.16}$$

and is compared to the 'real' values obtained directly from $\eta(t)$ according to

$$H_{rms} = 2\sqrt{2}\sigma_{\eta(t)} \tag{B.17}$$

as shown in Figure B.9. Both plots are shown to be similar in the shoaling and shallow water zone, but the RMS wave height determined from H in breaking zone is slightly less than the actual value. This slight difference is ignored and the values of H obtained are treated as acceptable results. The timeseries of H is used mainly for the auto-correlation of the timeseries and in cross-shore plots of the data for comparison to XBeach model output. The method of scaling does not affect the phase of the wave envelope, therefore it does not alter the auto-correlations for the case where the scaling is not employed.

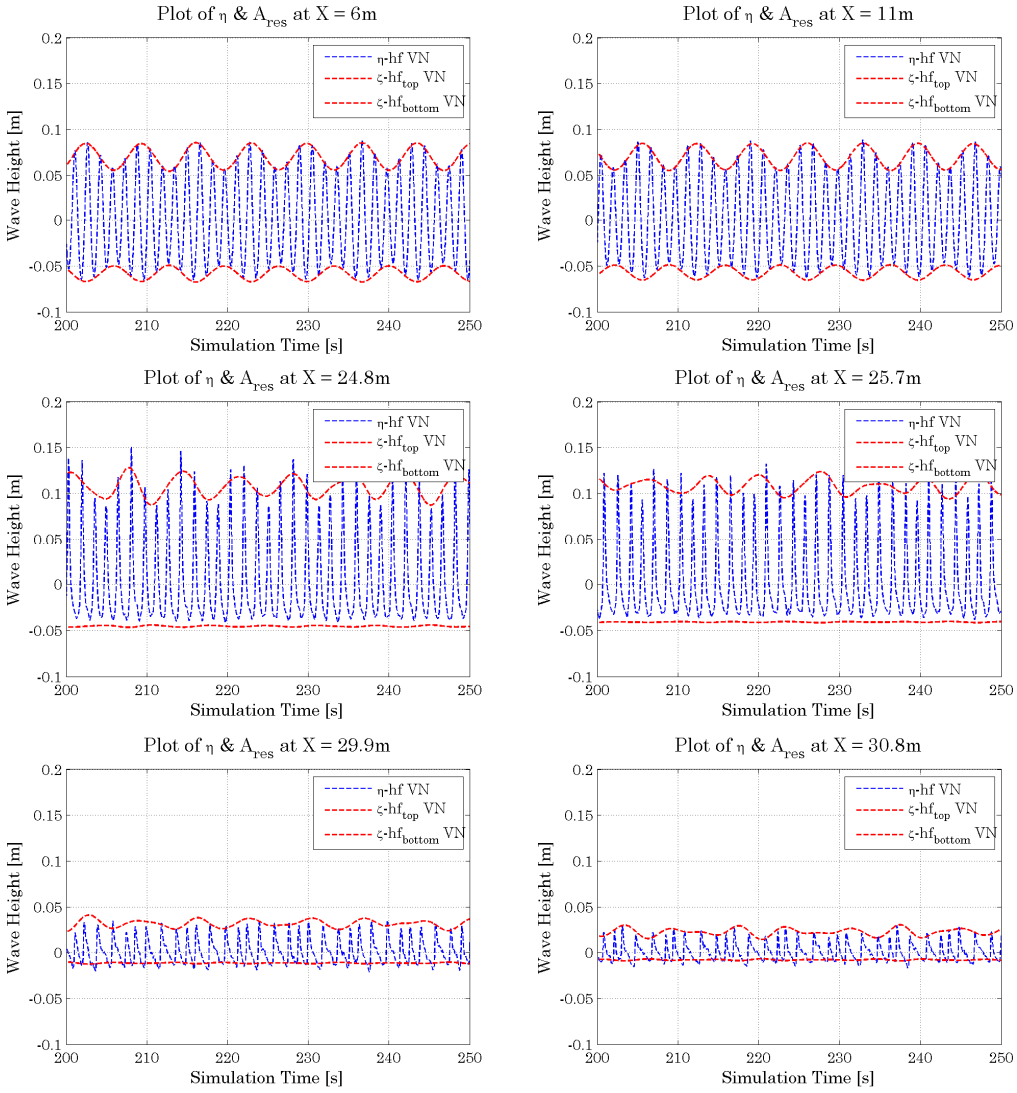

Figure B.8: The result of using the filtered Hilbert transform to obtain $A_{res,top,VN}$ and $A_{res,bot,VN}$ for point locations in the shoaling zone (top row), breaking zone (middle row) and shallow water zone (bottom row) after scaling for case A-2.

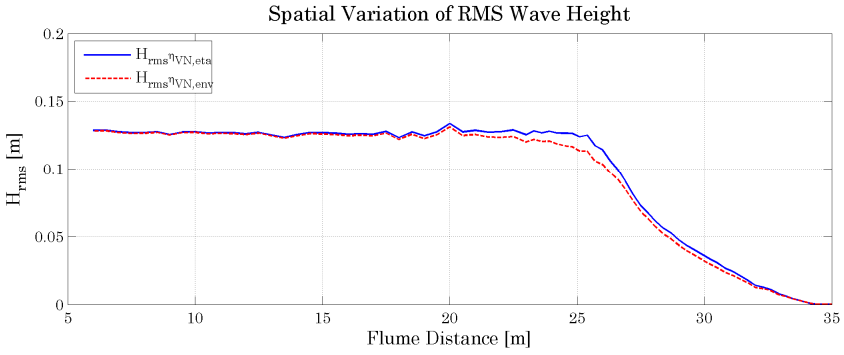

Figure B.9: RMS wave height computed from H (red line) and from $\eta(t)$ (blue line) for data from van Noorloos case A-2.

Appendix C – Low Frequency Wave Decomposition

A timeseries realization from a wave gauge in a flume will simultaneously contain waves which are generated by the wave maker propagating toward the back of the flume to the beach (incoming waves) and those reflected from the back of the flume at the beach (outgoing waves). For wave flumes which are equipped with Active Reflection Compensation (ARC), such as the one at the Delft University fluid mechanics laboratory, the re-reflection of the outgoing wave at the wave generator is suppressed. Incoming LF waves are generally bound to the forcing short wave groups until they break in shallow water and are released as free waves. These waves will be termed *incoming bound low frequency* (IBLF) waves. As the outgoing LF waves are free waves, we shall refer to them as *reflected free low frequency* (RFLF) waves. The summation of the IBLF and RFLF wave will give the total (measured) LF wave. Thus, an important assumption we make is that, due to ARC, *the incoming LF signal is due to bound LF waves only*. The decomposition of the IBLF and RFLF waves will allow us to conduct further analysis on the LF waves, such as the energy transfer to the IBLF waves from the short wave groups and the de-shoaling of RFLF waves. There are several methods which can be used to obtain a decomposed LF timeseries. In this thesis, two methods are employed – the collocated gauge method (used with XBeach data) and gauge array method (used with measurements from the van Noorloos experiment). These are discussed further in the following sections.

C.1 Collocated Gauge Method

C.1.1 Theory

With simultaneous measurements of surface elevation, ζ, and horizontal particle velocity, U, at the same point (collocated gauges), it is possible to decompose the LF timeseries into IBLF and RFLF timeseries by considering the conservation of flow. The method was first proposed by *Guza et al.* [1984] and has also been used in other work such as *van Dongeren* [1997]. The discharge of the total LF wave, Q, is assumed to be the summation of the discharge associated with the IBLF and RFLF wave components, Q^{in} and Q^{out} respectively, which are given for each cross-shore position, p, as

$$\begin{aligned} Q_j^{in} &= c_g \zeta_j^{in} \\ Q_j^{out} &= -\sqrt{gh}\,\zeta_j^{out} \end{aligned} \tag{C.1}$$

where c_g is the group velocity of the incoming short wave groups, $\sqrt{gh}$ is the free wave celerity and j is a time counter. The negative value of Q^{out} indicates the direction of propagation. Solving (C.1) for ζ^{in} and ζ^{out} gives

$$\zeta_{j,p}^{in} = \frac{\zeta_{j,p}\sqrt{gh_p} + Q_{j,p}^{in}}{c_{g,p} + \sqrt{gh_p}}$$
$$\zeta_{j,p}^{out} = \frac{\zeta_{j,p}c_g + Q_{j,p}^{out}}{c_{g,p} + \sqrt{gh_p}} \quad \text{(C.2)}$$

Replacing Q with U in (C.2), given that $U = Q/h$, we further get

$$\zeta_{j,p}^{in} = \frac{\zeta_{j,p}\sqrt{gh_p} + U_{j,p}h_p}{c_{g,p} + \sqrt{gh_p}}$$
$$\zeta_{j,p}^{out} = \frac{\zeta_{j,p}c_{g,p} - U_{j,p}h_p}{c_{g,p} + \sqrt{gh_p}} \quad \text{(C.3)}$$

The cross-shore amplitude variation of ζ^{in} and ζ^{out} is then found by using the Hilbert transform.

C.1.2 Application to XBeach Data

In order to apply the collocated decomposition method to the XBeach model output results, we first determine the group velocity, c_g, of the incoming short waves. This is given as output from XBeach, where the time averaged value is used for each cross-shore location, p. The c_g is computed up to the maximum inundation depth of the wave setup. Beyond this point a minimum value of 0.07 m/s is imposed to prevent negative values for dry regions.

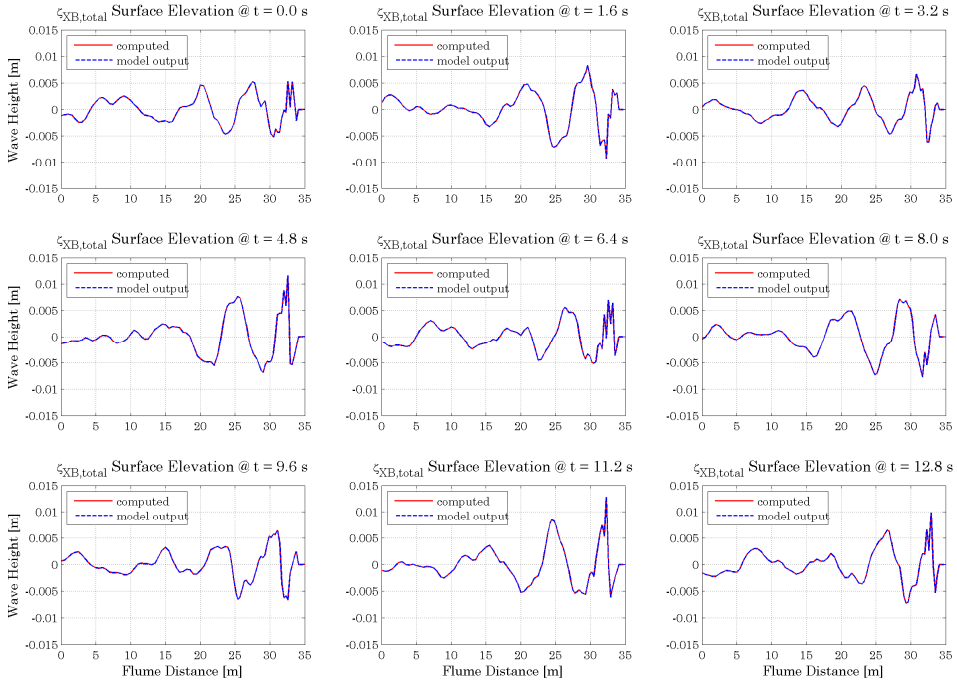

Figure C.1: Comparison of the spatial variation of the computed LF wave height obtained from the collocated decomposition method ($\zeta_{XB,in} + \zeta_{XB,out}$) (red line) and the LF wave given as model output from XBeach ζ_{XB} (blue line).

The LF timeseries given as output from XBeach includes the time averaged wave setup. This is therefore subtracted from the timeseries. XBeach also gives the horizontal particle velocity, U, as output. By directly applying (C.3) to the data, the IBLF and RLFL timeseries is obtained, which is styled as $\zeta_{XB,in}$ and $\zeta_{XB,out}$ respectively. Figure C.1 and Figure C.2 shows the spatial and temporal results of the decomposition respectively. In these figures, the LF timeseries obtained from the decomposition $\left(\zeta_{XB} = \zeta_{XB,in} + \zeta_{XB,out}\right)$ is compared to the model output as a check. As shown in the figures, the summation of $\zeta_{XB,in}$ and $\zeta_{XB,out}$ gives exact values as the XBeach output.

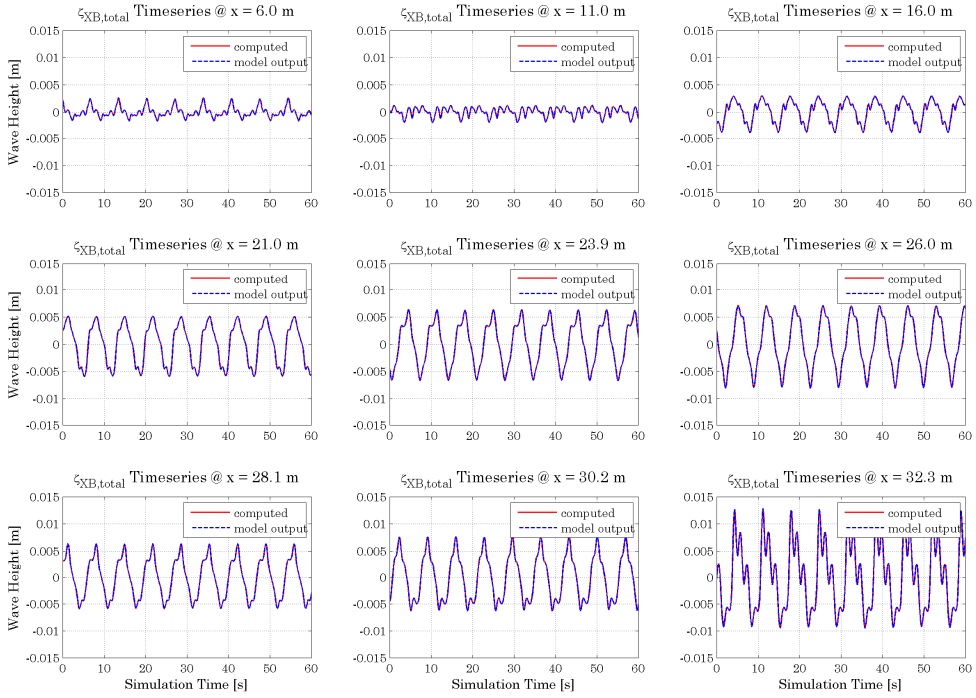

Figure C.2: Comparison of the timeseries of the computed LF wave height obtained from the collocated decomposition method ($\zeta_{XB,in}$ + $\zeta_{XB,out}$) (red line) and the LF given as model output from XBeach ζ_{XB} (blue line).

C.2 Gauge Array Method

C.2.1 Theory

The gauge array method is an extension of the *Mansard* and *Funke* [year] method which was proposed by *Battjes et al.* [2004] and further modified by *van Dongeren et al.* [2007]. This method uses a series of wave gauges to solve an overdetermined set of equations for the IBLF and RFLF wave. The LF timeseries is first obtained by filtering the measured timeseries and extracting the LF component. The complex amplitude of the LF wave, Z, in space, x, and time, t, can be written as

$$Z_{m,p} = \frac{1}{N}\sum_{j=1}^{N} \zeta\left(x_p, t_j\right) e^{-i2\pi f_m t_j} \tag{C.4}$$

where ζ is the LF timeseries, p denotes the gauge number in the local array with $p = 1, 2, \ldots, P$ and in which the central gauge is R, j is the time index, N is the number of points in the timeseries, m is the two-sided frequency counter $\left(0, \pm 1, \pm 2, \ldots\right)$ and $f_m = {}^{m}\!/_{D}$ is the LF wave frequency with D being the duration of the timeseries. The complex amplitude at the reference gauge, R, is considered to be the summation of the IBLF and RFLF components with an error, written as

$$Z_{m,p} = Q^{in}_{m,p,n} Z^{in}_{m,R,n} + Q^{out}_{m,p,n} Z^{out}_{m,R,n} + \varepsilon_{m,p,n} \tag{C.5}$$

where superscripts *in* and *out* indicate the incoming IBLF and the outgoing RFLF wave respectively, Q is a complex shoaling and phase correction factor, and n is a step counter in the multi-step process. Z^{in} and Z^{out} are the two unknowns in (C.5) which consists of P equations. If $P > 2$, then the system is overdetermined and a solution is found using a least square method. The system of equations is given as

$$\begin{bmatrix} Q^{in}_{m,1,n} & Q^{out}_{m,1,n} \\ \vdots & \vdots \\ Q^{in}_{m,R,n} & Q^{out}_{m,R,n} \\ \vdots & \vdots \\ Q^{in}_{m,P,n} & Q^{out}_{m,P,n} \end{bmatrix} \begin{bmatrix} Z^{in}_{m,R,n} \\ Z^{out}_{m,R,n} \end{bmatrix} = \begin{bmatrix} Z^{in}_{m,1} \\ \vdots \\ Z^{in}_{m,R} \\ \vdots \\ Z^{in}_{m,P} \end{bmatrix} + \begin{bmatrix} \varepsilon_{m,1,n} \\ \vdots \\ \varepsilon_{m,R,n} \\ \vdots \\ \varepsilon_{m,P,n} \end{bmatrix} \tag{C.6}$$

The multi-step process involves five steps. In the first step ($n = 1$) the factors Q^{in} and Q^{out} are set to the initial estimates of the phase function of the IBLF and RFLF waves based on linear wave theory. The IBLF wave is assumed to propagate with the group speed of the primary wave groups, c_g, and the RFLF waves are assumed to propagate with the linear phase speed of free waves, c, such that

$$\begin{aligned} Q^{in}_{m,p,1} &= e^{i\Phi^{in}_{m,p}} \\ Q^{out}_{m,p,1} &= e^{i\Phi^{out}_{m,p}} \end{aligned} \tag{C.7}$$

where

$$\begin{aligned} \Phi^{in}_{m,p} &= -\int_{x=0}^{x=x_p} \frac{2\pi f_m}{c_{g,p}}\, dx \\ \Phi^{out}_{m,p} &= -\int_{x=0}^{x=x_p} \frac{2\pi f_m}{c_{m,p}}\, dx \end{aligned} \tag{C.8}$$

This step assumes that the phase variation is according to the initial estimate and there is no shoaling over the local array. The initial estimate is therefore taken as the initial phase value determined from the argument of the FFT of the signal. Solving (C.6) using (C.7) gives an estimate of Z^{in} and Z^{out}. The local array is then shifted by one wave gauge and the new system of gauges are solved again, therefore giving estimates for all wave gauges except the first and last ${}^{P-1}\!/_{2}$ wave gauges in the entire cross-shore array.

The solution obtained from step $n=1$ is a complex amplitude, the argument of which can be seen as a correction for the initial phase values used at the centre reference gauge. In step $n=2$ and step $n=3$ this phase correction is added to Z^{in} and Z^{out} respectively (this cannot be done in a single step). The phase correction is then given as

$$Q^{in}_{m,p,2} = \frac{Z^{in}_{m,p,1}}{\left|Z^{in}_{m,p,1}\right|} Q^{in}_{m,p,1}$$
$$Q^{out}_{m,p,3} = \frac{Z^{out}_{m,p,1}}{\left|Z^{out}_{m,p,1}\right|} Q^{out}_{m,p,1} \qquad \text{(C.9)}$$

The subsequent steps, $n=4$ and $n=5$, (C.6) is solved again for all wave gauges, this time allowing for variations in the amplitudes over the array due to shoaling by re-using the amplitude information obtained in steps $n=2$ and $n=3$. The amplitude correction is given as

$$Q^{in}_{m,p,4} = \frac{\left|Z^{in}_{m,p,2}\right|}{\left|Z^{in}_{m,R,2}\right|} Q^{in}_{m,p,2}$$
$$Q^{out}_{m,p,5} = \frac{\left|Z^{out}_{m,p,3}\right|}{\left|Z^{out}_{m,R,3}\right|} Q^{out}_{m,p,3} \qquad \text{(C.10)}$$

The method can therefore be seen as a predictor-corrector method as it does not use any new information in the calculations and over a number of iteration, the solution for Z^{in} and Z^{out} converges. The method has been shown to reduce oscillations in the RFLF wave amplitude after the first decomposition step, attributed to the initial inaccuracies in the assumed phase and amplitude variation.

C.2.2 Application to Measured Data

The array method is applied to the van Noorloos measured data. The high spatial density of the wave gauges makes the decomposition quite accurate. Because the method approximates the celerity of the LF waves, which is determined with linear wave theory and therefore is based on the local water depth, the gauges which lie above the shoreline (the gauges located on the beach where swash is intermittent) are neglected. The shoreline limit is taken as the point to which the wave-induced setup reaches, which is taken as 0.05 m height above zero line. To avoid possible negative numbers above the zero line, a minimum value of 0.07 m/s is imposed. Seven wave gauges are used in the local array, therefore the IBLF and RFLF timeseries are available for a total of 66 wave gauges, beginning from the third wave gauge at x = 7.5 m and ending at the wave gauge at x = 33.5 m.

Figure C.3 below shows the results of the stepwise process used to obtain the IBLF and RFLF waves. The upper left figure shows the initial estimate of the phases (lower plot, dotted lines) and the corrected phase values (lower plot, solid line). The amplitude variation is then shown in the upper right figure. With subsequent iterations, the amplitude and phases converge as shown in the lower left and lower right figures.

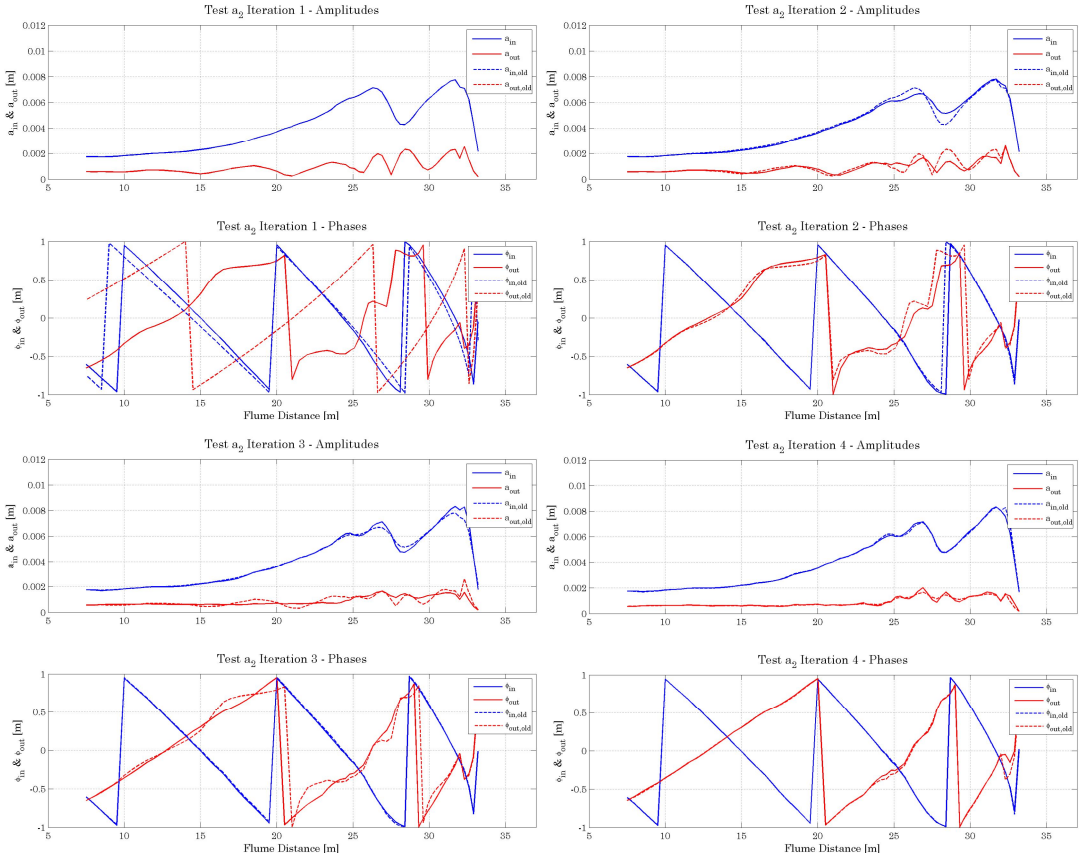

Figure C.3: Process of decomposing the measured LF wave from case A-2 of the van Noorloos experiment. Blue lines indicate the IBLF wave $\zeta_{VN,in}$ and red lines indicate the RFLF wave $\zeta_{VN,out}$. Solid lines indicate new values computed for the specified iteration step and dotted lines indicate the initial or former (old) values of the previous iteration step.

To check the accuracy of the decomposition technique, the IBLF and RFLF waves are added to obtain the total LF wave which is then compared to the originally measured values of ζ. Figure C.4 and Figure C.5 show these results in terms of cross-shore location and time respectively. The spatial variation of the computed LF wave is shown to be an approximation of the original which is of reasonable accuracy given the initial assumptions. Importantly, the phase variation is not too far off from the original, though the method seemingly smoothes out shock-like features. The timeseries reveals that the amplitudes are accurate for the most part, except in shallow water where they tend to be underestimated. This is most likely a direct result of the frequency spreading of the LF wave energy in this region. The timeseries of the decomposed LF waves only consist of the component at the difference frequency, therefore disregarding the contribution from other frequencies.

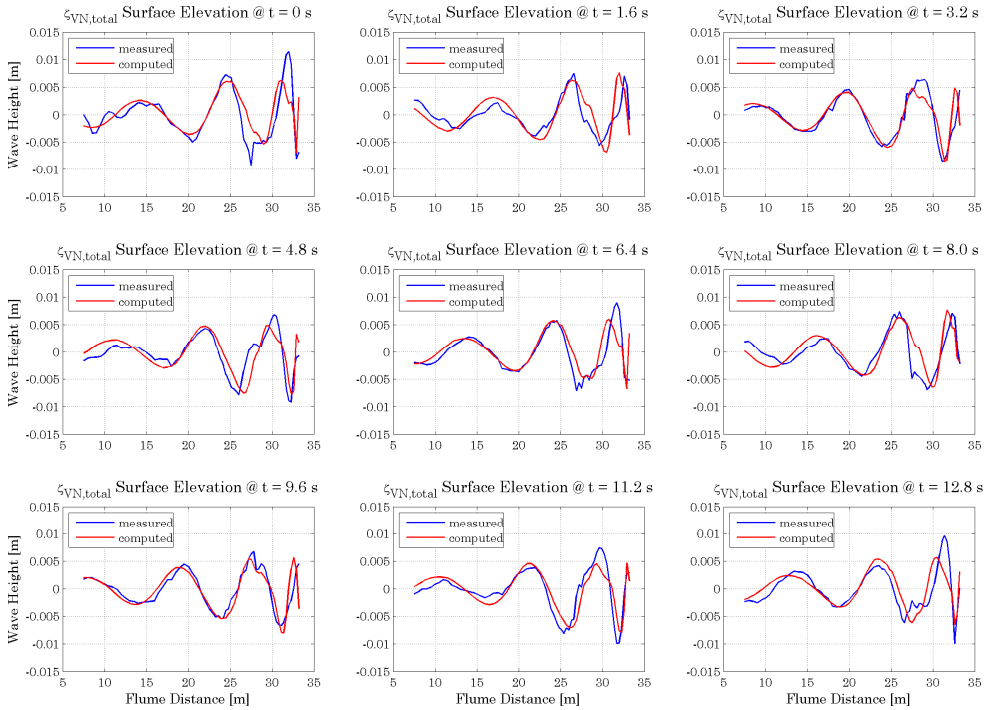

Figure C.4: Comparison of the spatial variation of the computed LF wave height obtained from the array decomposition method ($\zeta_{VN,in} + \zeta_{VN,out}$) (red line) and the measured LF wave from case A-2 of the van Noorloos experiment ζ_{VN} (blue line).

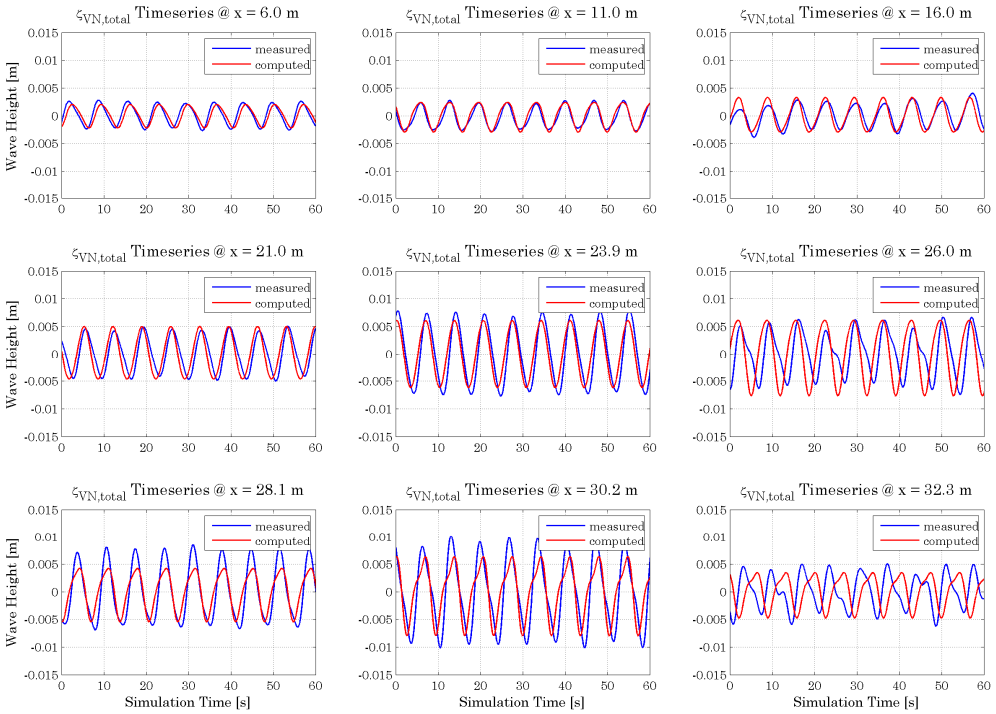

Figure C.5: Comparison of the timeseries of the computed LF wave height obtained from the array decomposition method ($\zeta_{VN,in} + \zeta_{VN,out}$) (red line) and the measured LF wave from case A-2 of the van Noorloos experiment ζ_{VN} (blue line).

Appendix D – Wave Gauge Locations

Table 2 below gives the cross-shore location of the wave gauges in the experimental setup of *van Noorloos* [2003].

Table 2 Wave Gauges Locations (x-coordinates) and Corresponding Water Depths (h) in the Flume.

Gauge No.	x [m]	h [m]	Gauge No.	x [m]	h [m]	Gauge No.	x [m]	h [m]
1	6	0.700	28	19.5	0.371	55	29.0	0.100
2	6.5	0.700	29	20.0	0.357	56	29.3	0.091
3	7.0	0.700	30	20.5	0.343	57	29.6	0.083
4	7.5	0.700	31	21.0	0.329	58	29.9	0.074
5	8.0	0.700	32	21.5	0.314	59	30.2	0.066
6	8.5	0.686	33	22.0	0.300	60	30.5	0.057
7	9.0	0.671	34	22.5	0.286	61	30.8	0.049
8	9.5	0.657	35	23.0	0.271	62	31.1	0.040
9	10.0	0.643	36	23.3	0.263	63	31.4	0.031
10	10.5	0.629	37	23.6	0.254	64	31.7	0.023
11	11.0	0.614	38	23.9	0.246	65	32.0	0.014
12	11.5	0.600	39	24.2	0.237	66	32.3	0.006
13	12.0	0.586	40	24.5	0.229	67	32.6	-0.003
14	12.5	0.571	41	24.8	0.220	68	32.9	-0.011
15	13.0	0.557	42	25.1	0.211	69	33.2	-0.020
16	13.5	0.543	43	25.4	0.203	70	33.5	-0.029
17	14.0	0.529	44	25.7	0.194	71	33.8	-0.037
18	14.5	0.514	45	26.0	0.186	72	34.1	-0.046
19	15.0	0.500	46	26.3	0.177	73	34.4	-0.054
20	15.5	0.486	47	26.6	0.169	74	34.7	-0.063
21	16.0	0.471	48	26.9	0.160	75	35.0	-0.071
22	16.5	0.457	49	27.2	0.151	76	35.3	-0.080
23	17.0	0.443	50	27.5	0.143	77	35.6	-0.089
24	17.5	0.429	51	27.8	0.134	78	35.9	-0.097
25	18.0	0.414	52	28.1	0.126	79	36.2	-0.106
26	18.5	0.400	53	28.4	0.117	80	36.5	-0.114
27	19.0	0.386	54	28.7	0.109			

Appendix E – Additional Graphics

E.1 Low Frequency Wave Results

The effect of increasing the eps parameter from the base case value of 0.001 m to 0.005 m is shown in Figure E.1 below for series A.

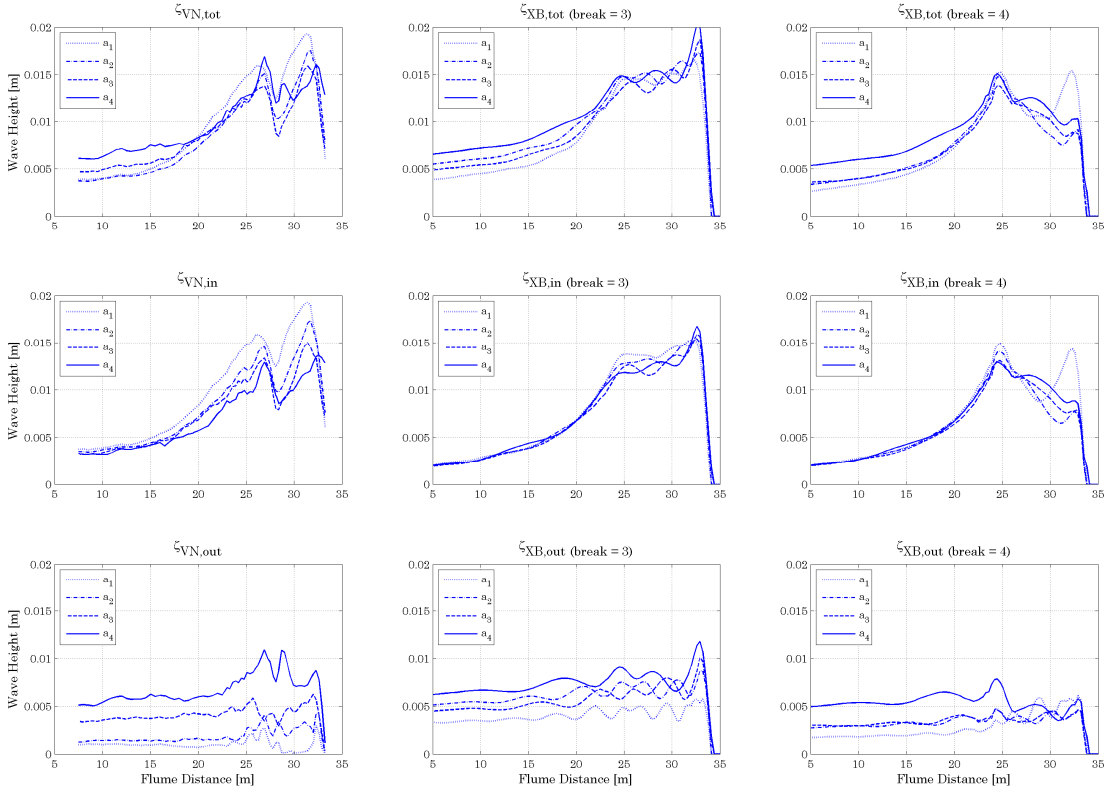

Figure E.1: Spatial variation of RMS values for the total (top row), inbound (centre row) and reflected (bottom row) LF waves from the van Noorloos (left column) and XBeach break = 3 (centre column) and break = 4 (right column) data for series A. (eps = 0.005, C = 70, grid 1).

The effect of decreasing the C parameter from the base case value of 70 $m^{0.5}s^{-1}$ to 50 $m^{0.5}s^{-1}$ is shown in Figure E.2 below for series A.

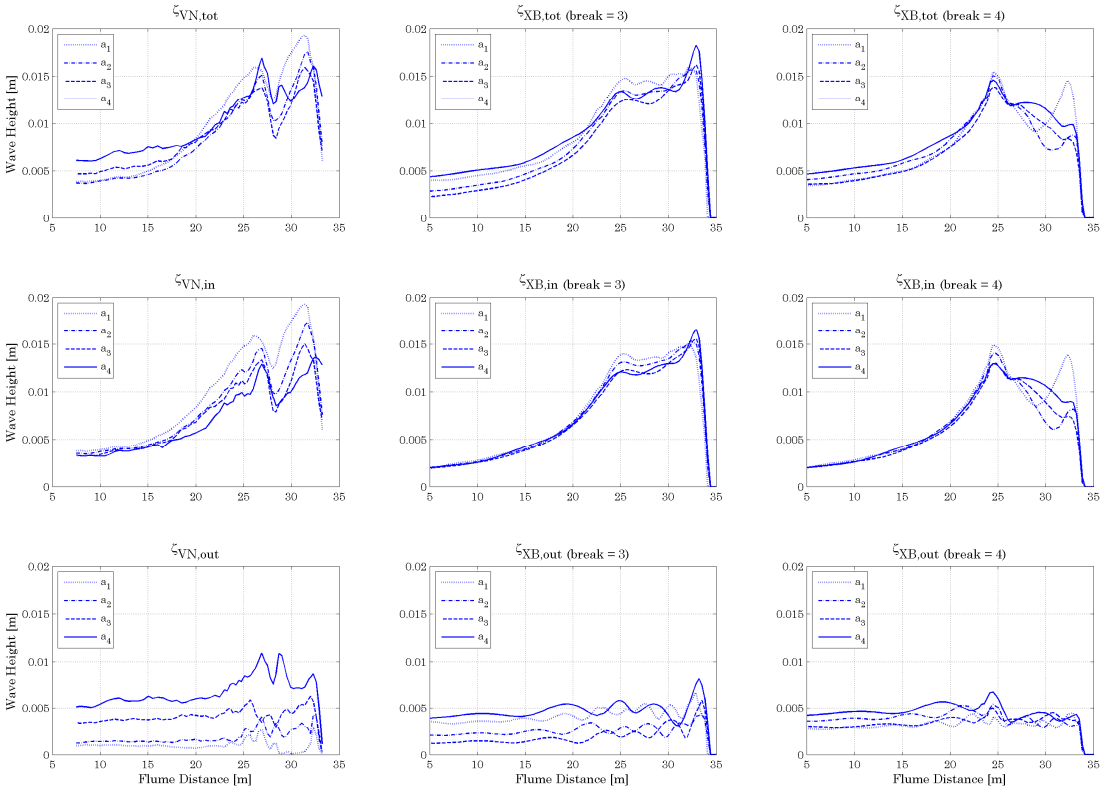

Figure E.2: As Figure E.1. (eps = 0.001, C = 50, grid 1).

The effect of doubling the grid resolution from the base case of 103 grid cells in the x-direction (grid 1) to 206 grid cells (grid 2) is shown in Figure E.3 below for series A.

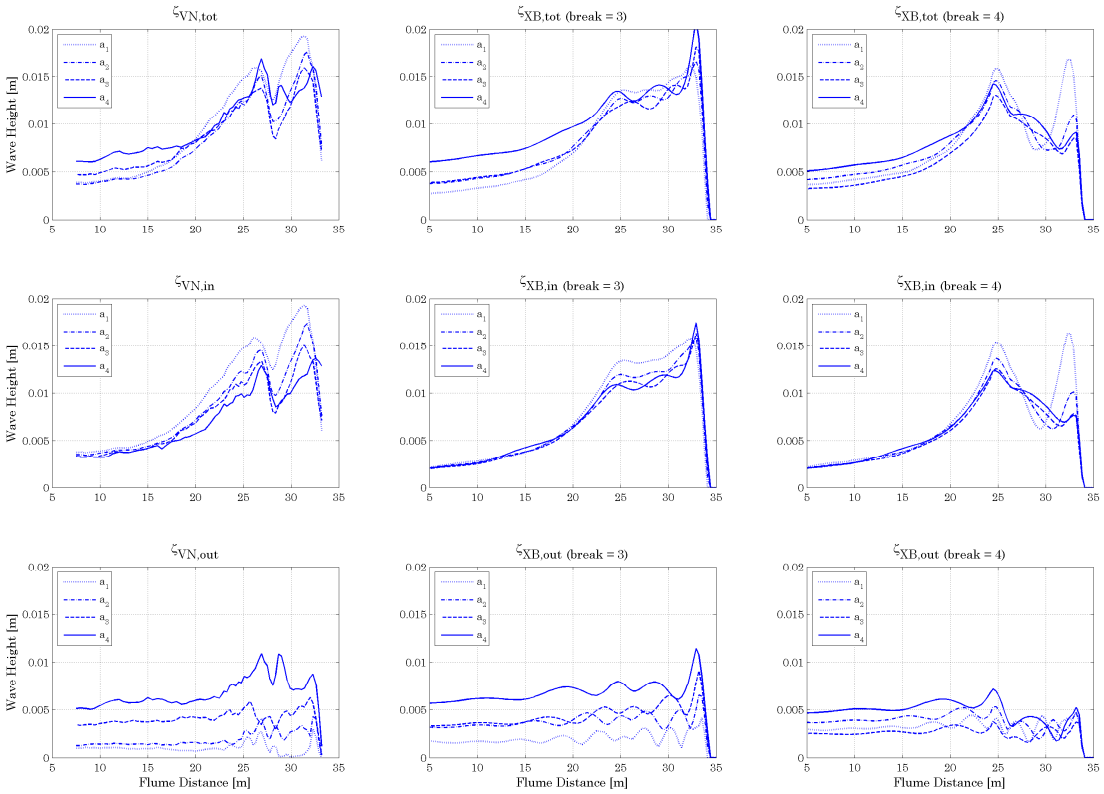

Figure E.3: As Figure E.1. (eps = 0.001, C = 70, grid 2).

The effect of increasing the eps parameter from the base case value of 0.001 m to 0.005 m is shown in Figure E.4 below for series B.

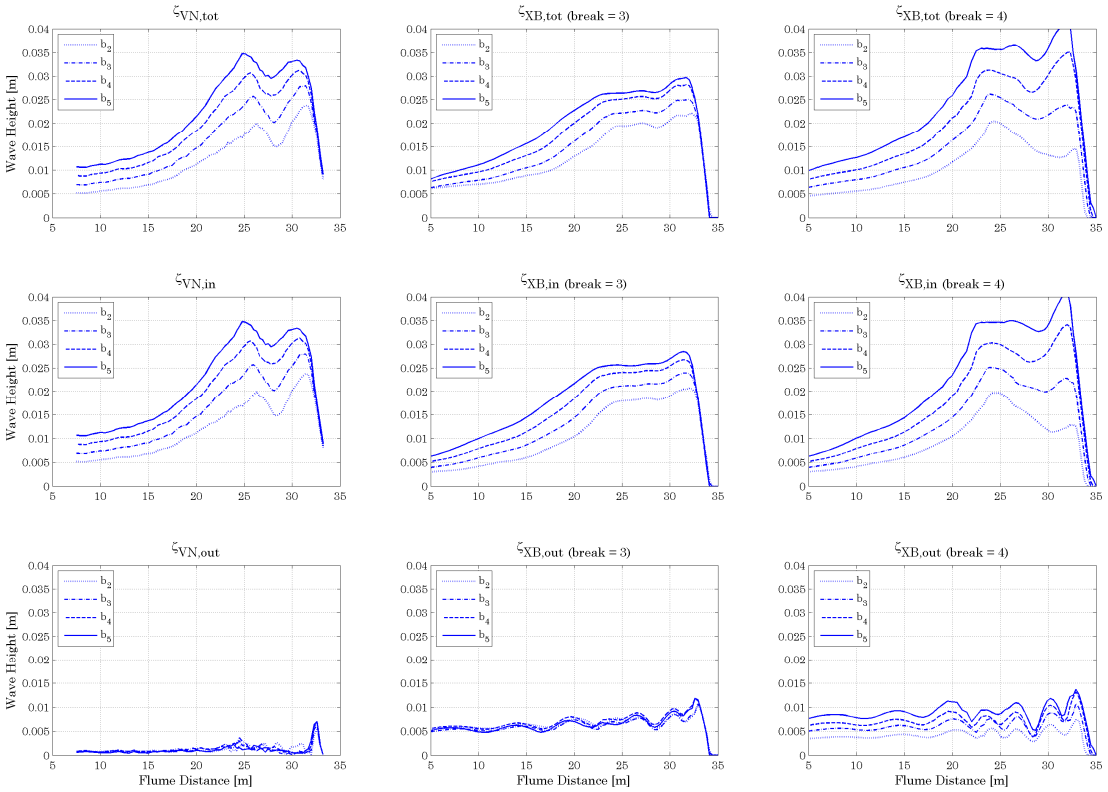

Figure E.4: Spatial variation of RMS values for the total (top row), inbound (centre row) and reflected (bottom row) LF waves from the van Noorloos (left column) and XBeach break = 3 (centre column) and break = 4 (right column) data for series B. (eps = 0.005, C = 70, grid 1).

The effect of decreasing the C parameter from the base case value of 70 $m^{0.5}s^{-1}$ to 50 $m^{0.5}s^{-1}$ is shown in Figure E.5 below for series B.

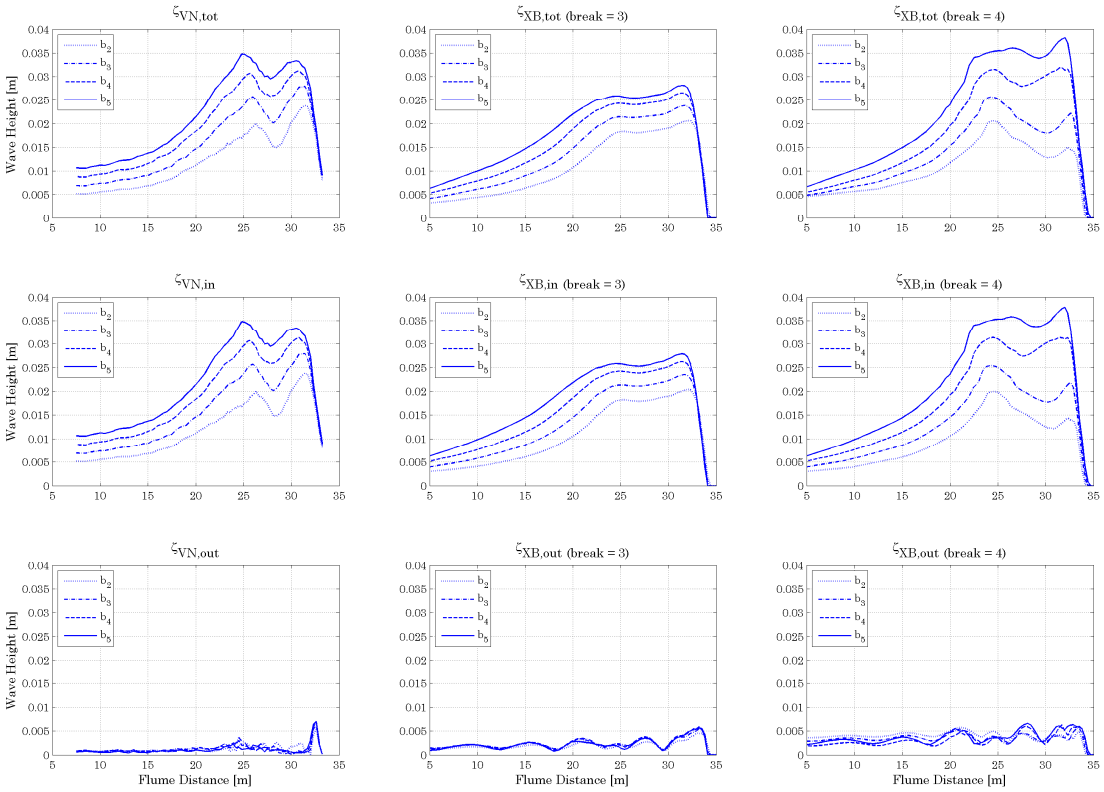

Figure E.5: As Figure E.4. (eps = 0.001, C = 50, grid 1).

The effect of doubling the grid resolution from the base case of 103 grid cells in the x-direction (grid 1) to 206 grid cells (grid 2) is shown in Figure E.6 below for series B.

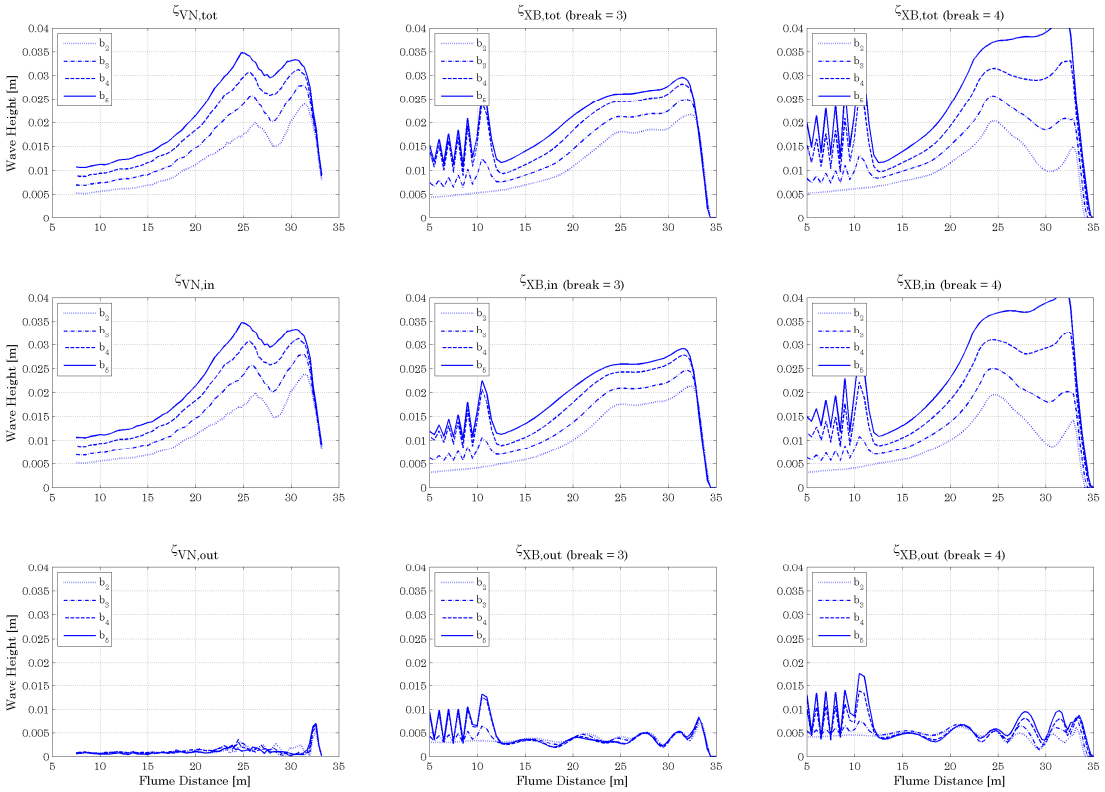

Figure E.6: As Figure E.4. (eps = 0.001, C = 70, grid 2).

The effect of turning off the excess radiation stress contribution from the roller model is shown in Figure E.7 below for series C.

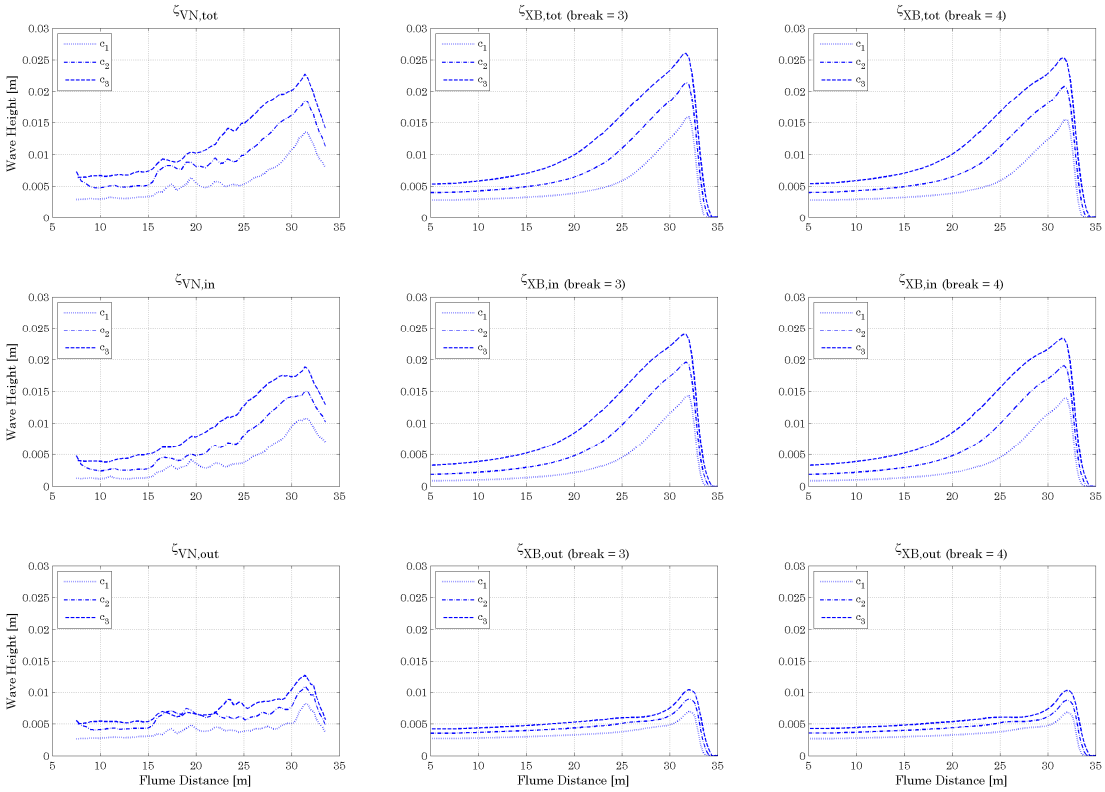

Figure E.7: Spatial variation of RMS values for the total (top row), inbound (centre row) and reflected (bottom row) LF waves from the van Noorloos (left column) and XBeach break = 3 (centre column) and break = 4 (right column) data for series C. (roller = 0, trepfac = 1).

The effect of using the mean spectral period, T_{m01}, over the peak spectral period, T_p, is shown in Figure E.8 below for series C.

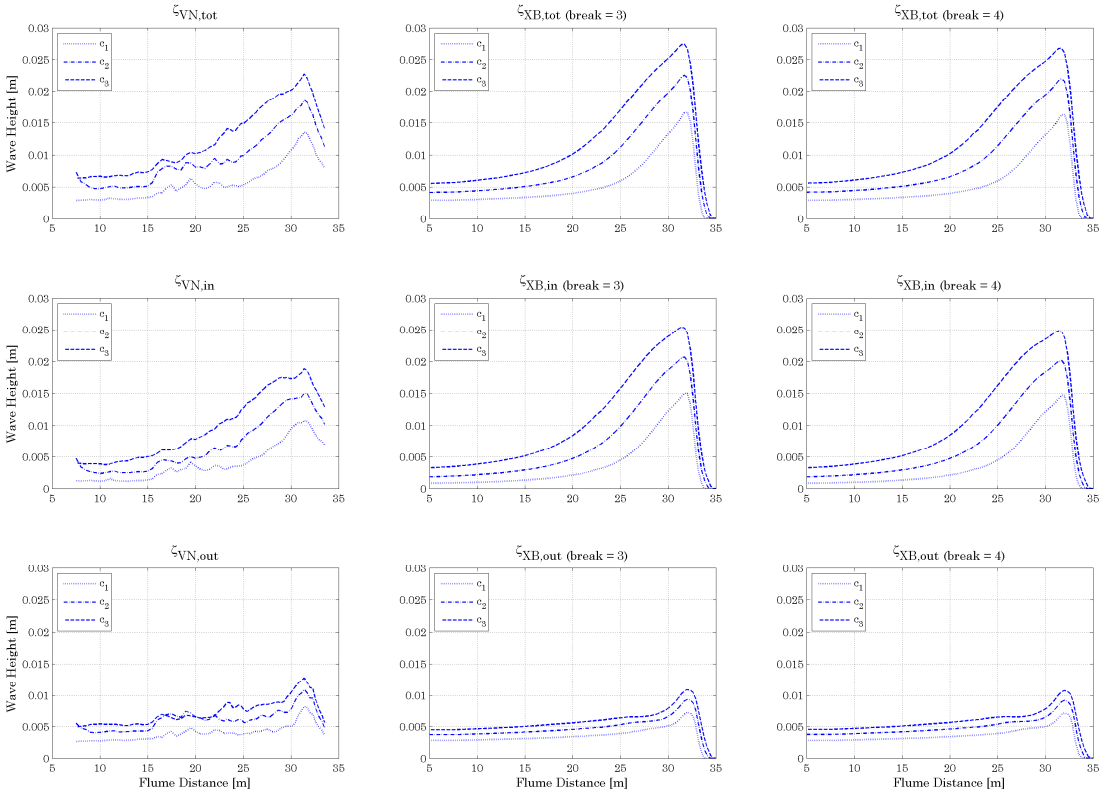

Figure E.8: As Figure E.7. (roller = 1, trepfac = 0).